PRODUCTION OF NEUTRON-UNBOUND STATES IN INTERMEDIATE-MASS FRAGMENTS FROM ^{14}N + Ag REACTIONS AT E/A = 35 MeV

By

Lawrence Harvey Heilbronn

A DISSERTATION

Submitted to
Michigan State University
in partial fulfillment of the requirements
for the degree of

DOCTOR OF PHILOSOPHY

Department of Physics and Astronomy

1990

ABSTRACT

PRODUCTION OF NEUTRON-UNBOUND STATES IN INTERMEDIATE-MASS FRAGMENTS FROM ^{14}N + Ag REACTIONS AT E/A = 35 MeV

By

Lawrence Harvey Heilbronn

The populations of neutron-unbound states and of bound states in intermediate-mass fragments have been measured at 15°, 31°, and 64° from the ^{14}N + Ag reaction at E/A = 35 MeV. The data are identified in terms of the reaction mechanism producing them, which is either a deep-inelastic mechanism or a quasielastic mechanism. In order to test the assumption that the deep-inelastic data are produced from a thermal source, the unbound-state/bound-state population ratios of deep-inelastic fragments are compared to the predictions of a thermal sequential decay model. Most, but not all, of the deep-inelastic population ratios are fitted with model calculations that assume a source temperature between 2.5 and 3.5 MeV. Three or more populations from the same isotope were measured for ^{13}C, ^{12}B, and ^{10}Be. The deep-inelastic populations from ^{13}C and ^{10}Be were fitted with a single temperature, while the deep-inelastic populations from ^{12}B were not fitted. There is enough of the deep-inelastic data that is not fitted with the predictions of a thermal model that the assumption of a thermal source for the production of deep-inelastic fragments may be incorrect, or there may be other effects present which alter the thermal properties of the data. The dependence of the unbound-state/bound-state population ratio on the fragment kinetic energy shows a difference between the quasielastic and deep-inelastic data. For quasielastic fragments whose mass is near the mass of the beam, the ratio decreases towards zero as the fragment velocity approaches the beam velocity. In contrast, the ratio for half-beam

mass quasielastic fragments is constant or only slightly decreasing as the kinetic energy increases. The ratio for deep-inelastic fragments is approximately constant as a function of kinetic energy, independent of fragment mass. The amount of feeding from several neutron-unbound channels into bound states is measured and compared to the sequential decay model. The effect of feeding on both spectral temperatures and on population temperatures is investigated. The effect of feeding on both temperatures, as determined by model calculations, cannot account for the discrepancy in the values between the two.

ACKNOWLEDGEMENTS

I would like to thank my advisor, Aaron Galonsky, for his interest in my career and for his patience with me over these six years. Not only has he taught me a great deal about nuclear physics, he has taught me a great deal about what it takes to be a nuclear physicist. Whatever I may do in the future, I hope that my work carries the qualities of preparedness, honesty, and thoroughness that Aaron has taught me. I have enjoyed my years in graduate school here at MSU, and I will really miss working with Aaron.

I would also like to thank Ferenc Deak, Adam Kiss, and Zoltan Seres for their friendship and for their help with my graduate work. It was a great experience for me to visit and work with them in Budapest, and I hope to return someday. I would also like to thank Bruce Remington, Greg Caskey, and Hugo Schelin for their help with my graduate work and for their friendship.

I want to thank Gary Westfall, Konrad Gelbke, and Bill Lynch for the interest they have shown in my studies and for their advice. It has been a great pleasure to work with the staff at the NSCL. Without question, the NSCL has been the best equipped and best staffed laboratory I have ever worked in. I would like to thank Gary Crawley, Konrad Gelbke, and Walt Benenson for the financial support they gave to me while serving as Director of Nuclear Science. In addition, I owe many thanks to Jules Kovacs for giving me the opportunity to study at MSU.

I would like to thank Daniel and Karen Cebra and Jim and Cynthia Clayton for their friendship. They have made these past six years some of the best years of my life.

I want to thank Len Porter and Randy Jeppesen for starting my interest in nuclear physics while I was an undergraduate at the University of Montana. In addition, I want to thank Paul Lisowski for giving me an opportunity to work with him at Los Alamos while I was an undergraduate.

I would like to thank my parents and family for their support. I consider myself lucky to have grown up in a home where education was very important. Most of all, I want to thank my wife, Lori, for her love and support. I look forward to growing old with her and reminiscing about these days.

TABLE OF CONTENTS

LIST OF TABLES

LIST OF FIGURES

Chapter I: Introduction

A. Motivation

An important property of intermediate-energy (E/A ~ 20-200 MeV) heavy-ion reactions is the production of intermediate-mass fragments (for this thesis, $3 \leq Z \leq 7$, $6 \leq A \leq 14$, referred to as IMFs). Both IMF and light particle spectra yield information about the reaction mechanisms governing their production, but IMFs bear additional information not found with very light particles, such as neutrons and protons. Specifically, IMFs are produced in excited states, and measurements of the populations of those states can be readily applied to an understanding of IMF production. In this thesis the populations of several neutron-unbound states in IMFs are reported along with their relevance to models used to explain IMF production.

In general, intermediate-energy reactions that have no fissionable products appear to produce IMFs from two different types of reaction mechanisms. Quasielastic (QE) processes dominate IMF spectra at high IMF kinetic energy at or near the grazing angle. Deep-inelastic (DI) processes dominate IMF spectra for all IMF kinetic energies at angles much greater than the grazing angle and for low IMF kinetic energies at or near the grazing angle. It should be pointed out that although there are many models associated with the word "deep-inelastic" that describe specific reactions, "deep-inelastic" is used here to describe a general class of reactions that result from violent collisions between the projectile and target in which a large amount of the projectile's kinetic energy is dissipated amongst the participating nucleons. The main difference between QE and DI processes is that DI fragments seem to come from a thermal source, whereas QE fragments appear to come from a nonthermal source.

1. IMF Singles Data

a. Quasielastic Data

Quasielastic IMF inclusive spectra have been detected in several systems (Moug81, Menc83, Guer83, Namb83, Murp83, Blum86, Cask88, Kiss89, Deak90). The fragmentation models of Goldhaber (Gold74) and Friedman (Frie83), which are successful in describing IMF spectra in high-energy heavy-ion collisions, are moderately successful in describing IMF spectra in intermediate-energy collisions. Specifically, the width and location of the quasielastic peak are two experimental observables that are predicted by these models. For intermediate beam energies, the peak shape at momenta greater than the peak value of the momentum are fitted well by the models. However, these models are unsuccessful in fitting the peak shapes below the peak momentum (Cask88) since both models predict a Gaussian peak shape (in momentum space), and in fact the peak has non-Gaussian shape below the peak momentum (see Figure 1 of Cask88). In general, the peak shape below the peak momentum is much broader than the high-momentum side for spectra from intermediate-energy reactions, whereas the peak shape for spectra from high-energy reactions is purely a Gaussian. This feature is seen as an important distinction between high-energy and intermediate-energy QE reactions.

Nucleon-exchange models, such as the stripping-pickup model (Kiss89), have been more successful in describing the general features of intermediate-energy IMF spectra. Qualitatively, the broad region below the peak momentum is seen in the model of Kiss et al. (Kiss89) as a consequence of the mixing between the projectile remenant and nucleons emitted by a source formed in the region of overlap between the target and projectile (this region is referred to as the participant zone). The lower the momentum, the more the number of nucleons from the participant zone that interacted with the projectile remnant. Also, lower-mass IMFs are believed to come from collisions with a smaller impact parameter (hence a larger overlap region) than higher-mass IMFs.

b. Deep-Inelastic Data

Deep-inelastic IMF spectra have been parameterized for a wide range of systems (Chen87a, Chen87b, Chen88, Bloc88, Fox88, Poch87) using the moving-source model (West76). The moving source model assumes that light particles and fragments are emitted from a hot, moving source that is in thermal equilibrium, and that the kinetic energy distribution of the emitted particles and fragments is governed by a Maxwell velocity distribution. In general, most of the IMFs come from a source with a velocity roughly one-third of the beam velocity (Bloc88, Deak90). As the beam energy increases, the source temperature also increases (see Figure 2 of Chen87a), which is consistent with the assumption of creating a thermal source. For the reaction used in this thesis the source temperature extracted from IMF spectra is about 13 MeV (Bloc88, Deak90).

2. IMF Excited-State Populations

a. Quasielastic Data

Populations of excited states of QE-produced IMFs, especially the populations of excited-state IMFs with large kinetic energies (Siwe85, Deak89), should bear information on the partition of excitation energy between reaction partners (Siwe85). The dependence of excited IMF population on IMF kinetic energy is seen as an important test of nucleon-exchange models (Siwe85, Siem71, Wilc90) used to describe QE IMF production. One group has reported on the dependence of the ratio of specific gamma-emitting states' populations to their corresponding fragment singles populations on kinetic energy (Siwe85). They show that for IMFs with a mass lower than the mass of the beam (stripping reactions) the ratio is essentially constant, whereas for IMFs with a mass higher than the mass of the beam (pickup reactions), the ratio increases as the kinetic energy increases. Another group (Deak89) has reported on the dependence of the ratio of the population of the 3.388-MeV state in ^{12}B to its corresponding bound states population on kinetic energy, and they report that the ratio decreases as the kinetic energy increases. It is interesting to note that these two reports on the

dependence of IMF excitation as a function of kinetic energy for QE-IMFs with mass below the mass of the beam are quite different from each other. It is not known if this difference is due to the fact that the two reports came from different reaction systems ($^{14}N + {}^{164}Dy$ at E/A = 20 MeV for Siwe85 and ^{14}N + Ag at E/A = 35 MeV for Deak89) or is due to the fact that bound-state populations were measured in one experiment (Siwe85) and unbound-state populations were measured in the other (Deak89). In any case, there is a need for more of this type of data on QE IMFs.

b. Deep-Inelastic Data

Both particle-bound excited states (Morr84, Morr85, Bloc87, Gome88, Xu89) and particle-unbound states (Deak89, Chen87a, Chen87b, Fox88, Poch87, Bloc87, Poch85a, Poch85b, Chit86, Xu86, Kiss87, Galo87, Chen87c, Sain88, Naya89, Cebr89) in IMFs have been detected in several intermediate-energy systems. The measured populations of these states can be used to calculate temperatures from a Boltzmann population distribution. The population ratio of two states of the same nucleus is related to the Boltzmann temperature (T) in the following way:

$$R = \frac{2J_1+1}{2J_2+1} \exp(-\Delta E/T) \qquad (I.1)$$

where R is the ratio of the population of state 1 to the population of state 2, J_1 and J_2 are the state spins, and ΔE is the difference in level energy between state 1 and state 2. If it is assumed that excited, DI IMFs come from a thermal source, then the population ratio gives the temperature of that source, just as IMF kinetic energy spectra give that temperature. For the system investigated in this thesis, the temperatures that have been deduced from excited state populations ranged from ~0.6 MeV to ~3 MeV. These population temperatures are much lower than the corresponding spectral temperatures.

Large discrepancies between population temperatures and spectral temperatures have been reported for other systems (Chen87a, Poch87, Xu89).

One possible explanation for the discrepancy between a Boltzmann temperature and Maxwell temperature measured for the same system is that sequential feeding from higher lying states may alter the measured populations of ground and excited states from their initial populations, making this experimentally derived "apparent" Boltzmann temperature different from the "true", or initial source temperature (Hahn87, Poch85b). The initial temperatures derived from analyses that compensate the measured state populations for feeding range from ~2.5 MeV to 5 MeV (Xu89, Fox88, Naya90). Thus, even after taking feeding into account the extracted population temperatures are still much lower than the spectral temperatures. To date, no attempt has been made to determine the effect that sequential feeding has on spectral temperatures deduced from IMF spectra.

There is some data that suggests that DI excited-IMFs are not produced by a thermal source. One group has measured the populations of seven states in the same isotope and has reported that it is not possible to fit a single temperature to all seven populations, even after taking feeding into account (Naya89). Also, the finding of population temperatures that are constant as a function of beam energies from E/A = 11 MeV to E/A = 94 MeV (Chen87a, Fox88, Gome88, Xu89, Sain88, Lee90a, Lee90b) contradicts the assumption of emission from a thermal source, as one would expect the the temperature to rise as more energy is dumped into the system. (It has been shown (see Figure 2 of Chen87a) that spectral temperatures do increase as the beam energy increases.)

Although there is some data on excited-state populations that seems inconsistent with what would be expected if they were produced by a thermal source, there is a large amount of population data that agrees with one property associated with thermal sources. One would expect that the populations of a large range of isotopes and states

created in the same system would reflect the same temperature, and this result is found for both bound-state and unbound-state populations (Fox88, Xu89). Although the value of the corresponding spectral temperatures derived from a moving-source analysis of inclusive IMF spectra are much higher than the population temperatures, they also are uniform as a function of IMF species. Thus, even though there is some contradictory evidence, the question of the validity of assumed thermal sources is still open.

Just as the dependence of R (Equation I.1) on IMF kinetic energy gives detailed information on the production of QE IMFs, this dependence can also yield important information on the nature of the thermal source producing DI IMFs, assuming they are produced by such a source. For example, if one assumes that this thermal source behaves like a source of infinite extent, one would expect the value of R to be constant as a function of kinetic energy. On the other hand, if the source is small enough, the effects of cooling from particle emission may give a different dependence of R on kinetic energy. One can imagine that as a finite-size source emits particles and fragments, it will cool and subsequently emit fragments whose kinetic energy distributions and state populations will be characteristic of the lower temperature. Because of this, IMFs with low values of kinetic energy would, on the average, come from the later, cooler stages of the reaction than IMFs with higher values of kinetic energy. Thus, the value of R would increase as IMF kinetic energy increased. An argument can be made that a finite-sized source which is vulnerable to the effects of evaporative cooling is <u>not</u> a source in thermal equilibrium, in which case it would not be correct to use a Boltzmann population distribution to calculate R. But in any case the dependence of R on IMF kinetic energy will add more information on the nature of the reaction mechanism producing DI IMFs.

B. Issues Addressed in this Thesis

The populations of several QE and DI IMF neutron-unbound states produced in the E/A = 35 MeV, ^{14}N + Ag system, will be reported on in this thesis. This work expands on the data previously reported on neutron-unbound states produced from this

system (Deak89, Bloc87), and adds to the set of data on bound-state populations (Morr84, Morr85) and charged particle-unbound state populations (Fox88, Naya90) for this system. The assumption of thermal production of DI IMFs will be tested by attempting to fit two-level population ratios calculated from measured unbound-state and bound-state populations to the predictions of the same ratios as calculated with a sequential feeding model using a single source temperature. It will also be determined whether three state populations in ^{12}B, three state populations in ^{10}Be, and four state populations in ^{13}C can be fitted with a single Boltzmann temperature. The dependence of R (Eq. 1) on IMF kinetic energy for both QE and DI IMFs will also be reported, along with its significance to the models used to describe QE and DI IMF production.

Using both the bound-state and unbound-state populations, the amount of feeding into bound-state populations from several neutron-unbound states will be reported and compared to predictions of the feeding from a sequential feeding model. The dependence of the feeding on kinetic energy will be used to determine the effect the feeding has on the parameters used to describe DI and QE IMF inclusive spectra. In particular, the effect feeding has on the spectral temperatures will be investigated, along with its consequences on the discrepancy between population temperatures and spectral temperatures.

Bound-state populations will be determined from IMF singles spectra that were also measured for this system. Fits to IMF singles spectra will be done using a parameterization suggested by Kiss89, and the results of these fits will be used to identify which regions of IMF kinetic energy are dominated by DI or QE processes. It is assumed that these regions are similar for unbound IMFs.

C. Organization

Chapter II contains the details of the experiment from which the data presented in this thesis came. Included are details about the fragment and neutron detectors, as well as a brief description of the electronics and data acquisition. Chapter III presents

the details of the data analysis which yielded fragment singles spectra and relative velocity spectra, and Chapter IV presents the results of that analysis. Chapter V compares the data on the populations of many bound and neutron-unbound IMF states with the predictions from a sequential-decay calculation. The sequential-decay model used for the comparison is described in Chapter V. Chapter VI contains the data showing the dependence of several population ratios on fragment kinetic energy. Chapter VII compares the data on feeding into IMF bound states to predictions from the sequential-decay model that was used in Chapter V. The effect the measured feeding has on IMF singles spectra is also presented in Chapter VII. Chapter VIII presents the conclusions from the data and analysis presented in the previous chapters. Appendix A details the calculation of the effective spin factor that was used in Chapter V, Appendix B explains the method used to determine the level-energies and widths of two neutron-unbound states from the data used in this thesis, Appendix C shows how the measured ^{7}Li singles spectra were corrected for ^{8}Be contamination, and Appendix D gives the details of how an energy-dependent width was used in the analysis of the 7.456-MeV state in ^{7}Li.

Chapter II: Experimental Method

A. Experimental Setup

The data presented in this thesis came from an experiment performed at the National Superconducting Cyclotron Laboratory during the fall of 1986. The K-500 cyclotron delivered a beam of 35 MeV/nucleon ^{14}N onto a silver target. Each beam burst was about 1 ns wide with a period of 52.4 ns. The energy of the beam was known to ± 2%. Typical beam intensity used during the experiment was about 1.5×10^{10} particles per second. The beam spot at the target location was roughly circular in shape, and it was about four mm in diameter.

The silver target and charged-particle detectors were housed in a 1/8 inch thick, 36-inch diameter steel scattering chamber with a domed lid on the top and bottom. Located at 0° and 180° with respect to the beam were five-inch diameter entrance and exit ports. Attached to these ports were four-inch diameter beam tubes. Nine-inch diameter ports were located on both sides of the chamber at 90° with respect to the beam axis, and two additional ports, both three inches in diameter, were located at -45° and 135° (a negative angle indicates the side opposite the charged-particle detectors). One-quarter inch thick black lexan was used for the port covers at ± 90° and at - 45°, and one-quarter inch thick clear lucite was used for the port cover at 135°. Signal cables for the fragment detectors were routed through the 90° ports using BNC-BNC and BNC-SHV vacuum feed-throughs. The coolant lines that ran to the charged-particle detectors were fed through the -45° port. A video camera was located just outside the port at 135° in order to monitor the position of the beam at the target location. A steel and concrete beam dump was located about two meters from the exit port of the chamber. A

well shielded Faraday cup was located at the end of the beam line inside the beam dump at a distance of about three meters from the target. During the experiment additional steel, lead and concrete shielding was added between the Faraday cup and neutron detectors which were located at 15° in order to reduce the number of background neutrons coming from the Faraday cup. A turbo vacuum pump and roughing pump were connected to the exit beam tube near the entrance to the beam dump. A cryogenic vacuum pump was connected to the bottom of the scattering chamber. Typical pressures inside the chamber during the experiment averaged about 1×10^{-5} torr. Mounted on top of the scattering chamber was a motor that controlled the height and rotation of the target ladder, which was inside the chamber.

The target ladder held four targets during the experiment. One of the targets used was a blank target, which was used to measure any events in the detection system that did not originate from the target. Another one of the targets used was a MgO scintillator, which was used to check the location of the beam at the target position. Finally, two rolled-silver targets of 5.0 mg/cm^2 and 3.88 mg/cm^2 were mounted on the target ladder. During the experiment the silver targets were rotated 45° with respect to the beam in order to minimize the energy loss in the target of reaction products observed with fragment detectors located at 15°, 31°, and 64°. No visible surface contamination of the targets from pump oils and coolant liquid was noted during the experiment.

A large amount of the time during the experiment was spent measuring neutron-fragment coincidences produced by collisions of ^{14}N projectiles with the silver targets. Since the goal of the experiment was to measure the populations of neutron-unbound states created during these collisions, and since there is a strong kinematical focussing of the neutrons that come from the decay of these states (Deak87), the neutron and fragment detectors were set up in a colinear alignment. One such setup was placed at

15°, where projectile fragmentation is the dominant reaction mechanism for production of IMFs. Two others were placed at 31° and 64°, where deep-inelastic reaction mechanisms dominate.

The neutron detectors that were used were glass cells filled with liquid scintillator. Two types of scintillator were used, NE-213 and BC-501, with no discernable differences in performance detected between them during data taking and analysis. Each cell was a cylinder approximately 7.6 cm long and 12.7 cm in diameter, and the glass used for the cells had a thickness of 1/8 inch. The back of each cell had a conical plastic (lucite) light pipe glued to it, which in turn had a 5.1 cm diameter photomultiplier tube glued to it. Each detector was housed in a thin aluminum can 15.25 cm in diameter, with a small amount of foam padding between the glass cell and the can. The intrinsic timing resolution of these detectors, when measured using γ-rays from a ^{60}Co source, was 0.9 ns on the average.

A close-packed array of three neutron detectors was centered at 15°, with a distance of 457 cm from the target to the centers of the scintillator cells. The array subtended a half angle of 1.9°, with 50% of the available solid angle in that space taken up by scintillator. Two close-packed arrays of seven detectors each were centered at 31° and 64°, with distances from target to cell centers of 438 cm and 354 cm, respectively. The array at 31° subtended a half angle of 2.8°, and the array at 64° subtended a half angle of 3.5°. Both arrays had 58% of the available solid angle taken up by scintillator. Table II.1 contains some of the important physical parameters of the neutron detectors that were placed in colinear alignment with a fragment detector.

"Veto paddles" were placed in front of the neutron detectors to detect any high energy protons that made it out of the scattering chamber and into the neutron detector. (In order for a proton to reach one of the neutron detectors it will typically have to go through at least 5 mm of silicon, 3 mm of steel, 3500 mm of air, 2 mm of aluminum, 6 mm of foam, and 3 mm of glass. Using those thicknesses, it is estimated that protons

Table II.1 - The positions of the neutron detectors used in the experiment along with the detector thicknesses and diameters and type of scintillator used.

angle Θ (deg)	angle Φ (deg)	distance from target to cell center (cm)	cell thickness (cm)	cell diameter (cm)	type of scintillator
14	-.6	456.51	7.525	12.355	BC 501
16	-.6	456.87	7.518	12.700	NE 213
15	1.1	457.52	6.985	12.471	NE 213
31	0	437.13	7.620	12.700	NE 213
33	0	437.87	7.630	12.295	BC 501
32	-1.7	437.63	7.140	12.365	BC 501
30	-1.7	437.82	7.530	12.355	BC 501
29	0	437.64	7.170	12.380	BC 501
30	1.7	437.72	7.330	12.355	BC 501
32	1.7	438.83	6.985	12.471	NE 213
64	0	352.73	7.620	12.700	NE 213
67	0	353.51	7.570	12.380	BC 501
66	-2.1	354.50	6.985	12.471	NE 213
63	-2.1	353.59	7.730	12.275	BC 501
62	0	353.53	7.620	12.270	BC 501
63	2.1	354.50	6.985	12.471	NE 213
66	2.1	353.44	7.445	12.325	BC 501

with kinetic energies of approximately 70 MeV or greater can make it to the neutron detectors.) The veto paddle used in this experiment was a round, 6-mm thick plastic scintillator approximately six inches in diameter. Each scintillator was glued to a light pipe, which in turn was glued to a two-inch phototube. It was placed in the laboratory such that the solid angles subtended by a neutron-detector array and its veto paddle were the same. Any signal in the neutron detector that was in coincidence with a signal in the veto detector in front of the neutron detector was subsequently identified as a proton.

In order to measure the number of background neutrons produced during the experiment, shadow bars were placed between the target and neutron detector arrays. Each bar was a brass cylinder 7.6 cm in diameter, and was long enough (50.8 cm at 15°, 40.6 cm at 31°, and 30.0 cm at 64°) to stop more than 99% of the neutron flux coming from the target directly to the neutron detector. About 40% of the beam time was dedicated to measuring background neutrons.

Figure II.1 shows a schematic overhead view of the entire experimental setup. The shadow bars are represented by the hatched lines, and the veto paddles are represented by the solid lines. The dashed outlines around a neutron detector indicate a multidetector array. The boxes inside the scattering chamber represent the silicon-detector telescopes. The dashed box at 0° is for the out-of-plane telescope, which was placed at a polar angle of 14° below the beam.

Fragment isotope identification and energy determination were achieved using solid-state silicon detectors. Two-element, ΔE-E telescopes were used at 31° (94μm and 5mm) and 64° (74μm and 5mm). At 15°, where some Li fragments have a large range, a four-element, ΔE-ΔE-E-E telescope (94μm, 97μm, 5mm, and 1mm) was used. Every element was cooled to -10°C to reduce the noise due to thermally excited electrons that "leak" into the conduction band of the Si detector. Good isotope identification and separation of IMFs were achieved using these telescopes. Fragment energy calibration

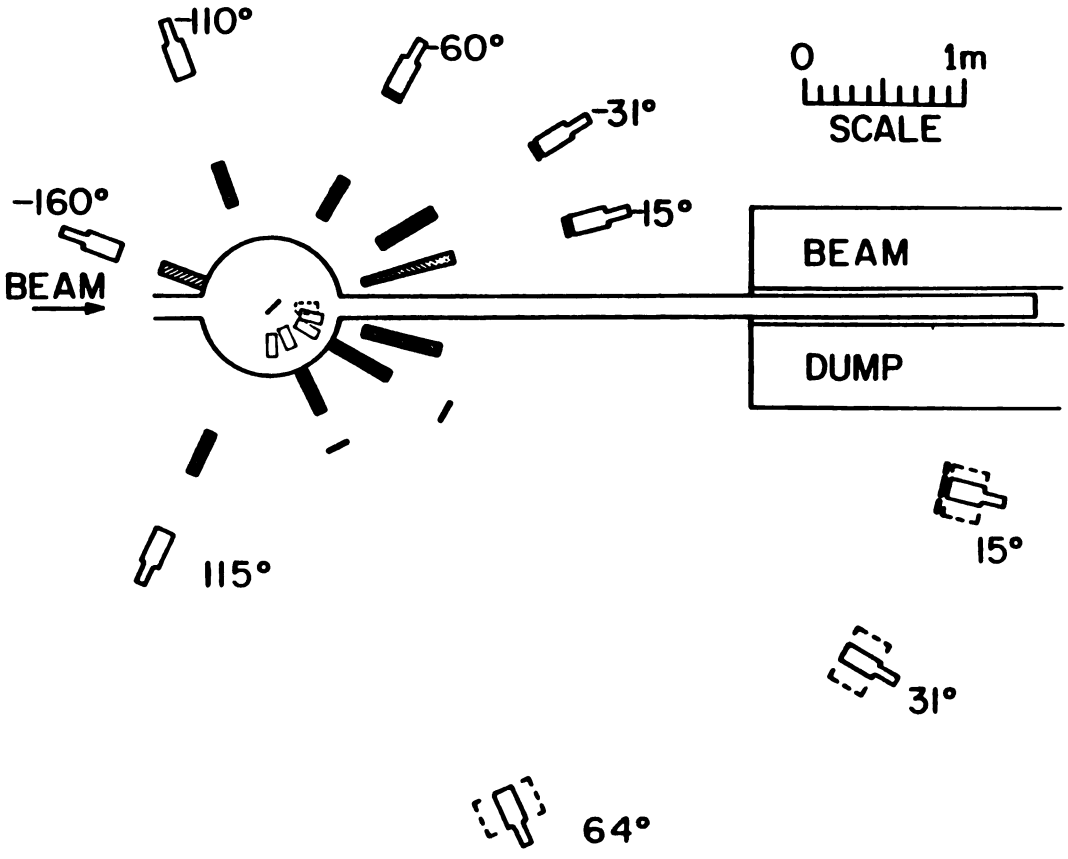

Figure II.1 - Overhead schematic view of the experimental setup

was done with alpha particles from a ^{232}Th source, using a calibrated pulser to extend the calibration to higher energies. Fragment energies were determined with an uncertaintity of ±2%.

Copper collimators with a thin (10 mg/cm^2) gold foil placed on their front faces were placed in front of each telescope. The foils were used to stop electrons and x-rays knocked out from the target. The diameters of the collimators defined the solid angle subtended by each of the fragment detectors. The collimator at 15° subtended a half angle of 1.9° and a solid angle of 3.5 msr. The collimators at 31° and 64° both subtended half angles of 2.9° and solid angles of 8.1 msr.

Neutron energies were determined by using a time-of-flight technique that used neutron and fragment signals as the start and stop, respectively, of a timing circuit. The timing signal from the fragment side of the circuit came from the first ΔE element of each telescope, with the aid of a time-pickoff unit. The timing signal from the neutron side came from the fast (anode) pulse from the neutron detector. The overall timing resolution of this system was determined by looking at the prompt γ-rays in the time-of-flight spectra, and was 0.9 ns for all three angles.

As mentioned above, a blank target was used to measure the number of coincidence events that did not originate from the target. The results from this measurement indicated that no appreciable amount of the data came from such events.

B. Electronics and Data Acquisition

Figure II.2 shows a simplified version of the electronics setup used for the experiment from which the data in this thesis came. Shown are the electronics for a single neutron detector (with a veto paddle) and the four-element telescope which was used at 15°. The electronics setup for the other neutron detectors and silicon telescopes was the same, with the exception that the other telescopes were two-element telescopes.

Neutron/gamma-ray separation was achieved using a pulse-shape discrimination technique (Helt88) that uses charge-integrating ADCs to integrate the

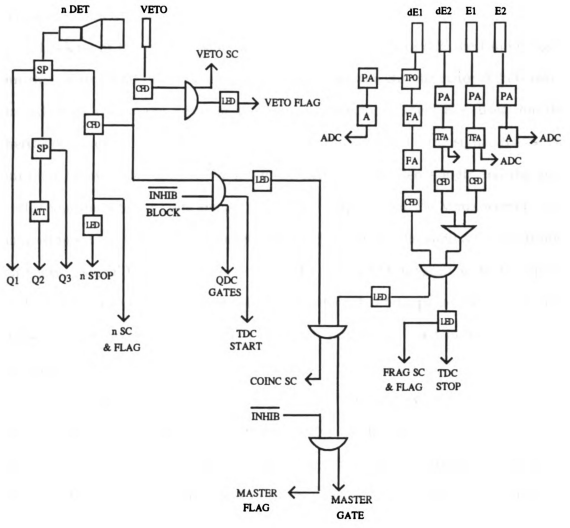

Figure II.2 - Electronics setup for one neutron detector (+ veto paddle) and a four-element silicon detector

total anode pulse from the neutron detector and to integrate the tail of the pulse. A clear separation between neutrons and gamma rays can then be seen in a plot of the tail-integrated charge versus the total-integrated charge (see Figure 3 of Helt88). The charge-integrating ADCs used in this experiment were Lecroy 2249W.

Looking at the neutron side of the electronics in Figure II.2, the timing signal from the neutron side was taken from a constant-fraction discriminator (CFD) which was fed from the anode pulse of the neutron detector. The CFDs used for this experiment were Tennelec TC-455s. In addition to the neutron timing signal, the output from the CFD was also used in the fragment/neutron coincidence logic and the veto-paddle/neutron-detector coincidence logic. The output from the veto/neutron logic was used to set the veto scaler. Note that in the pulse-shape discrimination electronics each neutron signal is integrated three times. In addition to integrating the total pulse and the tail of the pulse (as described above), an attenuated total pulse is also integrated in order to increase the dynamic range of signals that can be used in the pulse-shape discrimination technique.

Looking at the fragment side of Figure II.2, the timing signal from the fragment side originated from the signal of the first (or only) ΔE element with the aid of a time-pickoff unit (TPO). The fast timing signal from the TPO was then fed into a CFD, which then generated the timing signal used in the fragment/neutron time-of-flight logic. A valid fragment event required a coincidence between signals from the ΔE and E elements. The output from the $\Delta E/E$ coincidence logic was then used in the fragment/neutron coincidence logic. Pulse heights of the signals from the silicon elements were recorded via analog-to-digital convertors (ADCs - Ortec AD811).

Neutron/fragment time-of-flight was determined from a time-to-digital convertor (TDC - LeCroy 2228A). The channel width of the TDCs was determined after the experiment using an EG&G time calibrator. Each channel was found to be, on the average, about 0.225 ns wide, which is lower than the nominal value of 0.25 ns.

Data acquisition was performed using a system developed at the NSCL (Vand85) based on a 68010 microprocessor. For each coincidence event the fragment-telescope identification number and pulse height from each telescope element were recorded, along with the time of flight between the coincident fragment and neutron signals. On the neutron side of the event the neutron-detector identification number, total charge (of the anode pulse), attenuated total charge, and tail charge were recorded. For fragment-singles measurements, just the fragment-telescope bit registers and telescope-element pulse heights were recorded.

Chapter III: Data Analysis

The goal of the data analysis was to measure both bound-state and neutron-unbound state populations in IMFs. Before the populations were determined it was necessary to apply corrections to both the IMF singles and IMF-neutron coincidence data. Once these corrections were made, IMF singles spectra and IMF-neutron relative velocity spectra were produced, and from these spectra the state populations were extracted.

A. IMF Singles Data

As previously mentioned, IMF energies were determined using calibrated silicon telescopes. Small corrections to these energies were needed to compensate for energy loss in the target and the gold foil that preceded each telescope. In addition, the energy loss in the dead layers of the silicon detectors was also taken into account.

After applying the corrections to IMF energy on an event-by-event basis, IMF singles spectra were generated for each isotope at 15°, 31°, and 64° in the following manner. First, two-dimensional spectra were constructed with particle-identification number (PID) on the ordinate and fragment energy on the abcissa. PID was calculated from the following equation:

$$PID = n \times [(E_{tot})^x - (E)^x]^{1/3}, \qquad \text{(III.1)}$$

where

$$x = 1.82 + \frac{1.3 \times \Delta E}{(1+E)\,t}, \qquad \text{(III.2)}$$

and where E_{tot} is the sum of the ΔE and E signals, t is the thickness of the ΔE detectors (in units of μm), and n is a normalization constant chosen such that the maximum value of the PID is 32767. Once the two dimensional spectra were constructed, 5-MeV wide cuts were made along the energy axis, and those cuts were projected onto the PID axis. Figure III.1 shows the resulting plot for Be isotopes (note the absence of ^{8}Be) at 15° with energies between 240 MeV and 245 MeV. The solid line in Figure III.1 indicates a fit to the data using three Gaussians added on top of a linear background. The area of each Gaussian was then taken to be the number of counts for the corresponding isotope in that energy range. The number of counts was then converted to a cross section.

B. IMF-Neutron Coincidence Data

The corrections which were applied to the IMF kinetic energy are also needed for a precise determination of the neutron energy, since neutron energies were determined from a time-of-flight method that used the fragment signal for the stop, requiring the fragment flight time to be added to the neutron-fragment time of flight. The position of the gamma-ray peak in the time-of-flight spectrum did not shift as a function of IMF kinetic energy, which indicates that the proper fragment-flight time was added to each gamma-fragment (and neutron-fragment) time of flight.

Once the neutron flight time was determined for each event, corrections were made for the neutron side of the event. The energy dependent neutron detection efficiency for each detector was calculated using the code TOTEFF (Kurz64), and these calculations were compared to the efficiencies computed using a Monte-Carlo code developed by Cecil et al. (Ceci79). The results from the two codes disagreed by at most 10%, and this value was taken as the uncertainty in the efficiencies. Figure III.2 shows the efficiency calculation using TOTEFF for one of the neutron detectors at 15°. The signal-energy threshold used in the calculation was 800 keV equivalent-electron energy, which corresponds to proton energy of 3 MeV. This threshold, which is higher than the

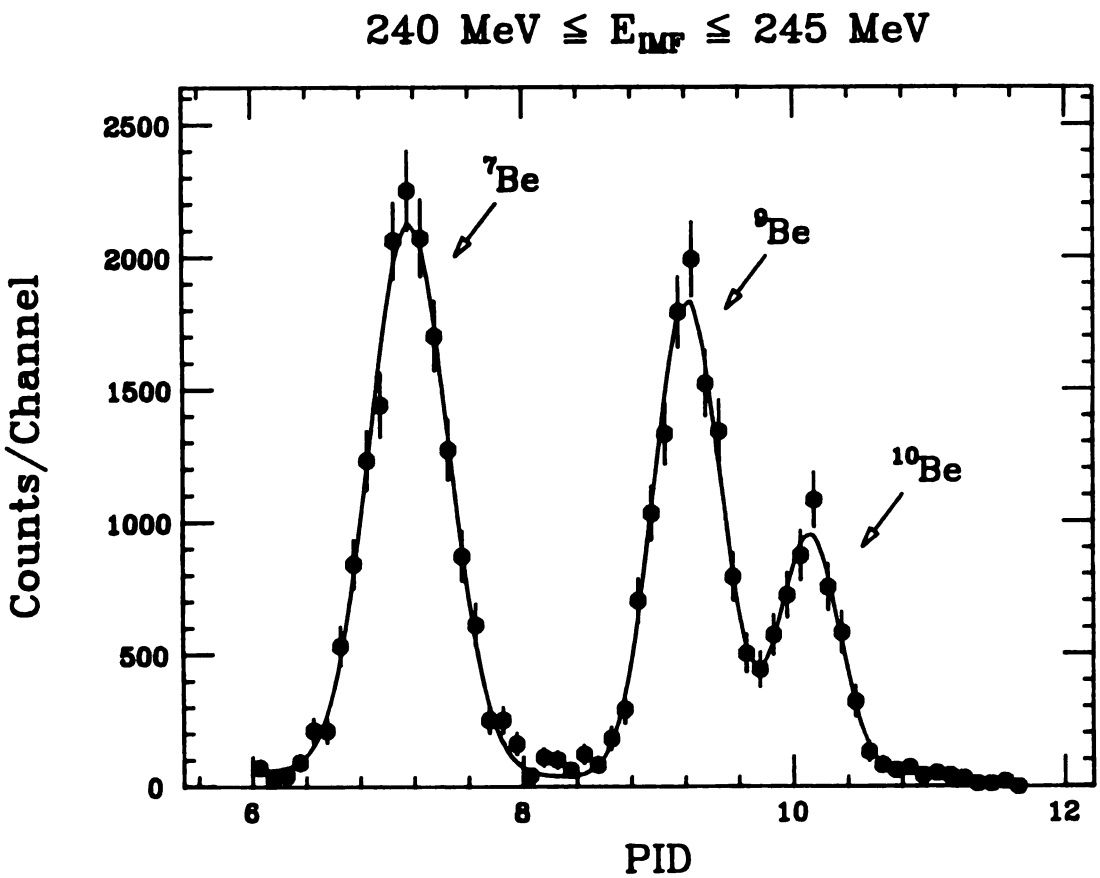

Figure III.1 - A particle identification spectrum for beryllium isotopes at 15° and for fragment kinetic energies between 240 and 245 MeV. The solid line shows a fit to the spectrum using three Gaussians added on top of a linear background.

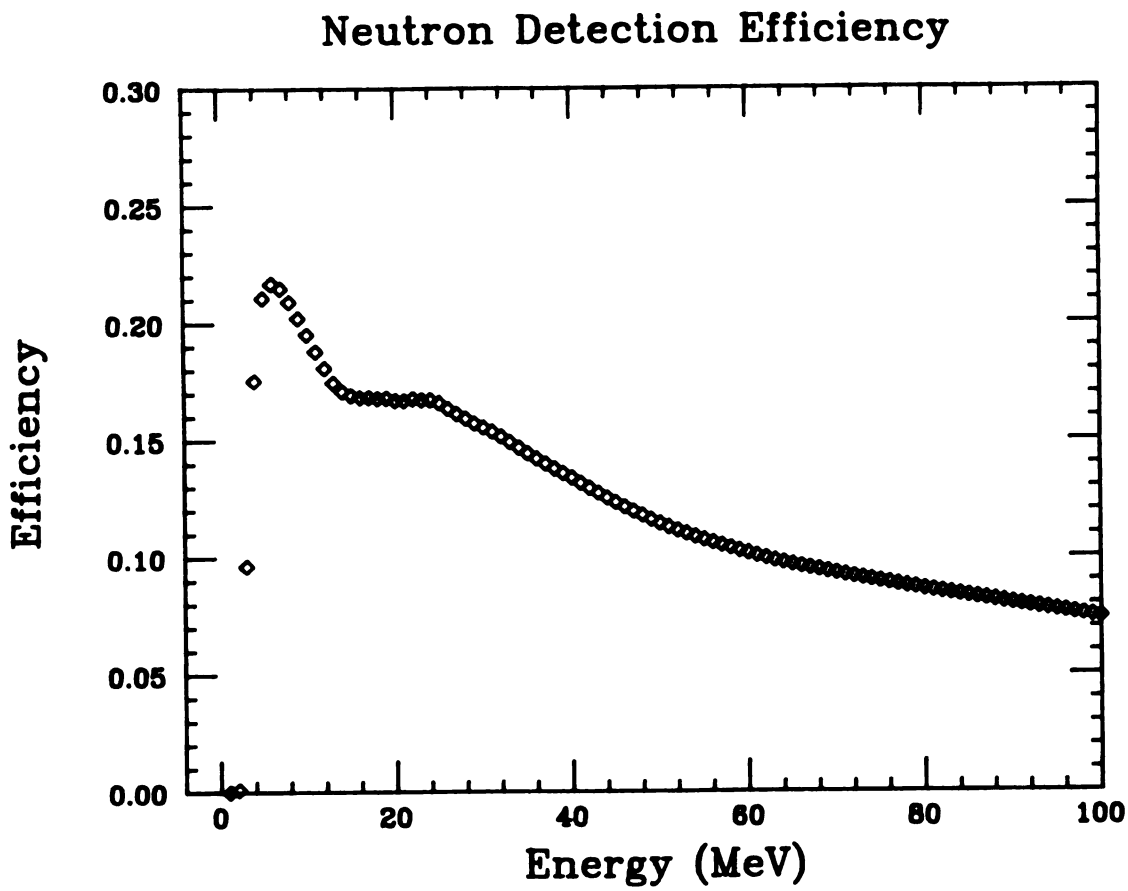

Figure III.2 - Neutron detection efficiency versus neutron energy for one of the neutron detectors placed at 15°.

hardware threshold used during data acquisition, was applied to all of the neutron signals in the subsequent analysis.

The loss of neutron flux due to out-scattering from materials between the target and neutron detector (silicon detectors, steel vacuum chamber wall, air, aluminum neutron detector can, and glass cell) was estimated using a code developed by Remington (Remi86). Other energy dependent corrections such as the background subtraction and accidentals subtraction were also made. All corrections were applied on an event-by-event basis.

After the corrections were made, relative velocity spectra were constructed from the colinear coincidence events using a technique very similar to the one used to construct IMF singles spectra. First, cuts were made on IMF PID that separated them by element. Then the relative velocity between a fragment and its coincident neutron was calculated on an event-by-event basis by assuming all the fragments of a particular element had the mass of one of its isotopes. The next step was then to construct two-dimensional plots of PID versus relative velocity. Cuts 0.1 cm/ns wide were then made along the relative velocity axis and projected onto the PID axis. Figure III.3 shows a plot resulting from this projection for Li isotopes with a cut made on relative velocity between 0.6 cm/ns and 0.7 cm/ns. In this case the relative velocities were calculated assuming all of the lithium was ^{7}Li. Fits to the data in plots such as Figure III.3 were done by fitting Gaussians on top of a linear background. The solid line in Figure III.3 shows the fit. The area of each Gaussian was taken to be the number of counts for each isotope in the corresponding relative-velocity bin. Of course, the number of counts is correct only for the isotope whose mass was used to calculate the relative velocity, and is <u>incorrect</u> for all other isotopes. For example, in Figure III.3 only the number of counts in the peak corresponding to ^{7}Li + n is correct. The number of counts for ^{6}Li +n was calculated by repeating all of the above steps, except the mass used to calculate the relative velocity was the mass of ^{6}Li, not ^{7}Li. Figure III.4 is the same as Figure III.3,

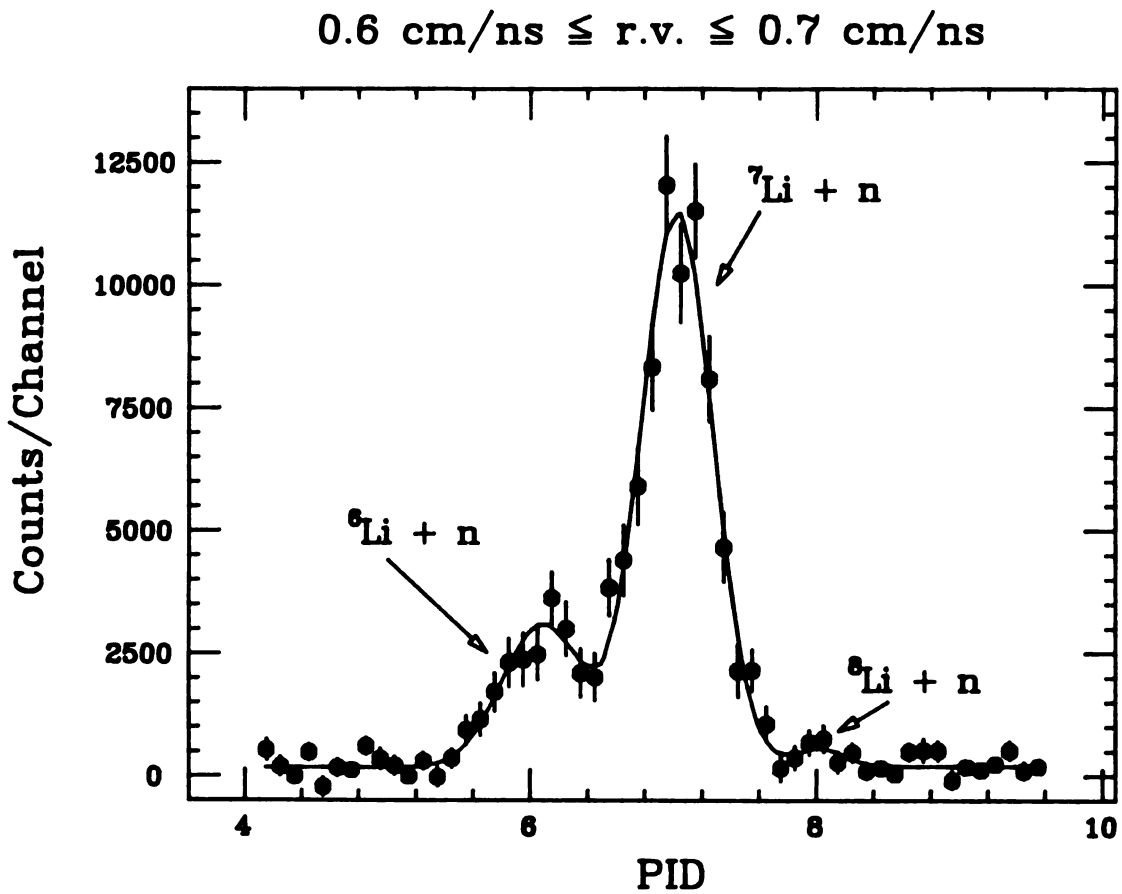

Figure III.3 - Particle identification spectrum for lithium isotopes in coincidence with neutrons at 15° and for v_{Li}-v_n between 0.6 and 0.7 cm/ns. Relative velocities were calculated using a mass number of seven for all fragments. The solid line shows a fit to the data using three Gaussians added onto a linear background.

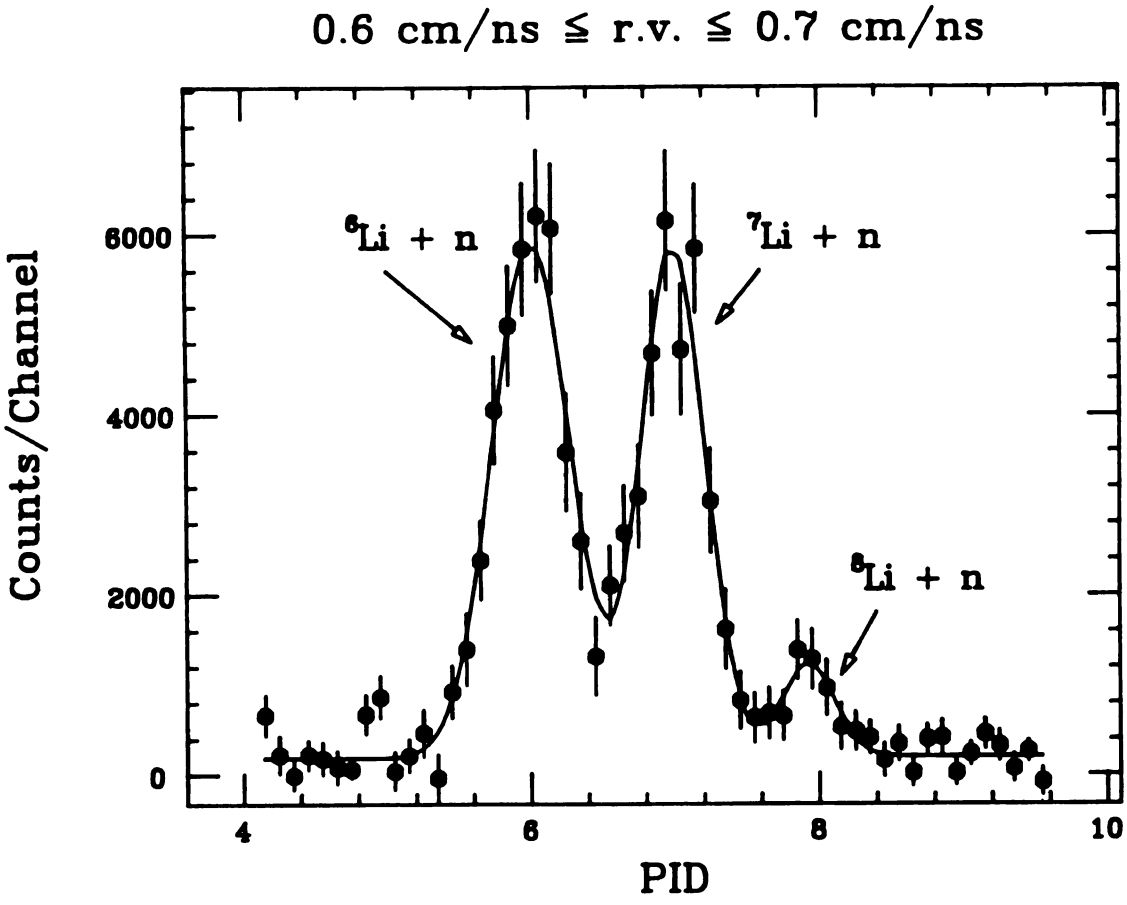

Figure III.4 - Same as Figure III.3 except the relative velocities were calculated using a mass number of six.

except the relative velocity was calculated using the mass of ^{6}Li. Relative velocity plots for particular isotope/neutron coincidences were then built up using the number of counts extracted from the fits to plots like the ones in Figures III.3 and III.4

Figure III.5 shows a relative velocity spectrum for neutrons in coincidence with ^{12}C at 15°. The abcissa shows the value of the fragment velocity minus the neutron velocity, while the top of the figure shows the relative energy between the fragment and neutron. Included in Figure III.5 is an energy level diagram which indicates the decays that show a resonance in the corresponding relative velocity plot. The solid line shows a fit to the data from Monte Carlo simulations (described later in this chapter) of the decays of the numbered resonances into the detection system added onto a background. The background is indicated with the dotted line.

Looking at Figure III.5, one notes that for each decay from a single state or group of states there are two peaks, one at a negative relative velocity and one at a positive relative velocity. These two peaks are a result of the kinematical focussing of the decay neutron and the finite detector geometry. Figure III.6 illustrates the decay of an excited fragment into a daughter fragment and a neutron. The dashed lines indicate the available solid angle for neutron and fragment detection. For simplicity, the daughter recoil momentum is neglected and the solid angles of the neutron and fragment detectors are taken to be equal. If the decay energy is large enough, only the most forward-focussed neutrons (which give a negative relative velocity) and the most backward-focussed neutrons (positive relative velocity) will be detected. In this way two peaks are created for each decay. The peak at negative relative velocity will be larger than its companion peak at positive relative velocity since the available solid angle in the decay frame for detection (the geometrical efficiency) is greater for forward-focussed neutrons.

If the decay energy is small enough, all of the neutrons will be focussed into the neutron detector, and as a result there will only be one peak in the corresponding

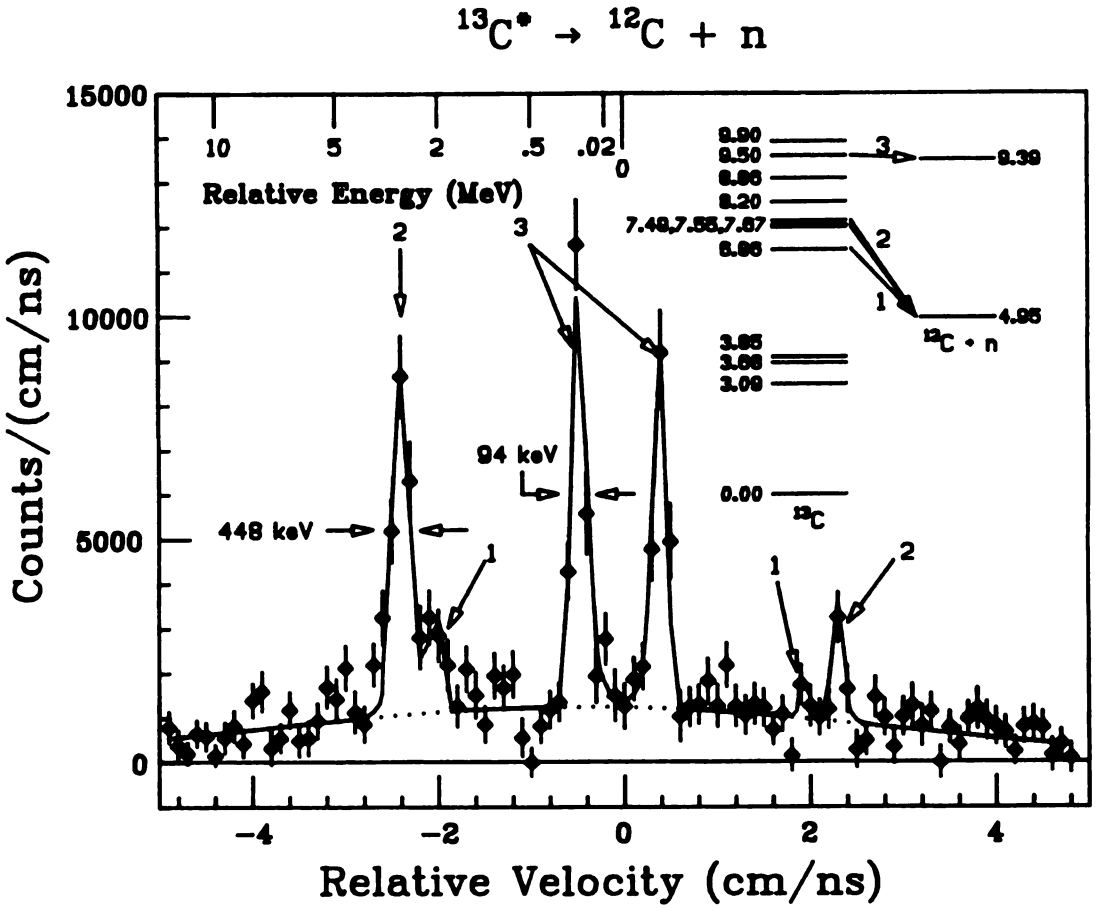

Figure III.5 - Relative velocity spectrum for $^{12}C + n$ at 15° and for $E_{^{12}C} \geq 15$ MeV/A. The numbered resonances come from the decays indicated in the level diagram. A relative energy scale is included for reference. The FWHM of peaks 2 and 3 are given. Each width corresponds to relative velocity resolution of 2 cm/ns. The solid line is from a fit described in the text, and the dotted line shows the background used in the fit (a Gaussian).

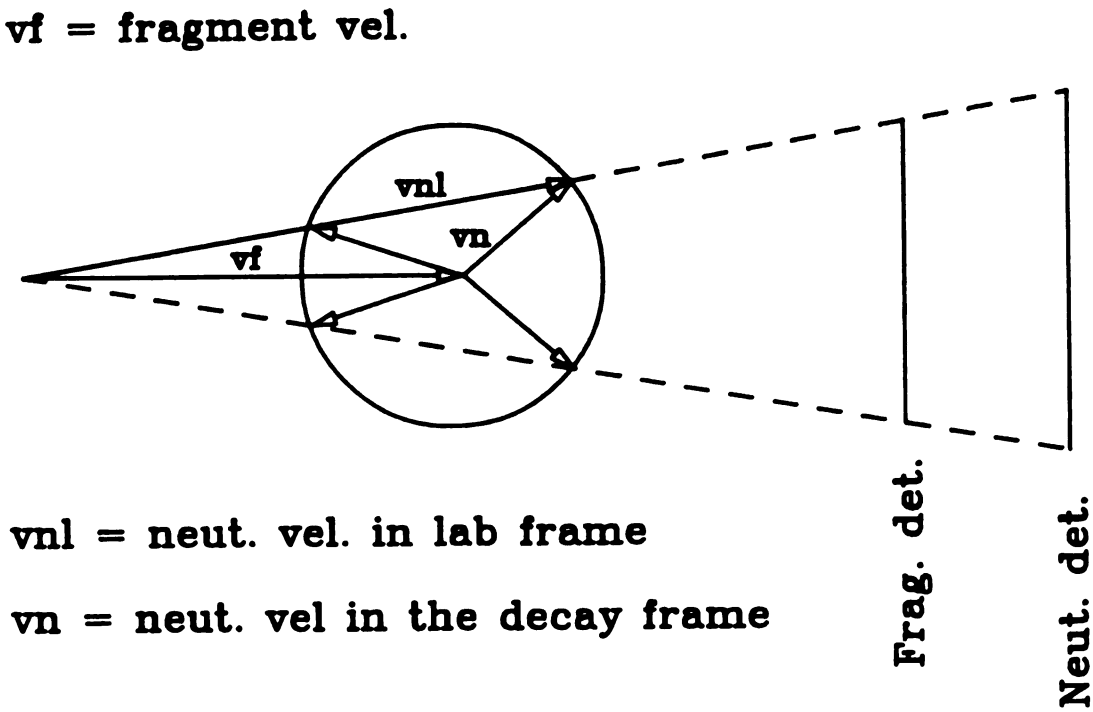

Figure III.6 - A velocity diagram showing the neutron decay of an excited fragment heading towards a colinear fragment-neutron detection system. Recoil of the daughter is neglected. The dashed line indicates the cone of acceptance of the detection system, and the circle represents all of the possible directions of decay. Only decays that lie within the cone of acceptance will be detected.

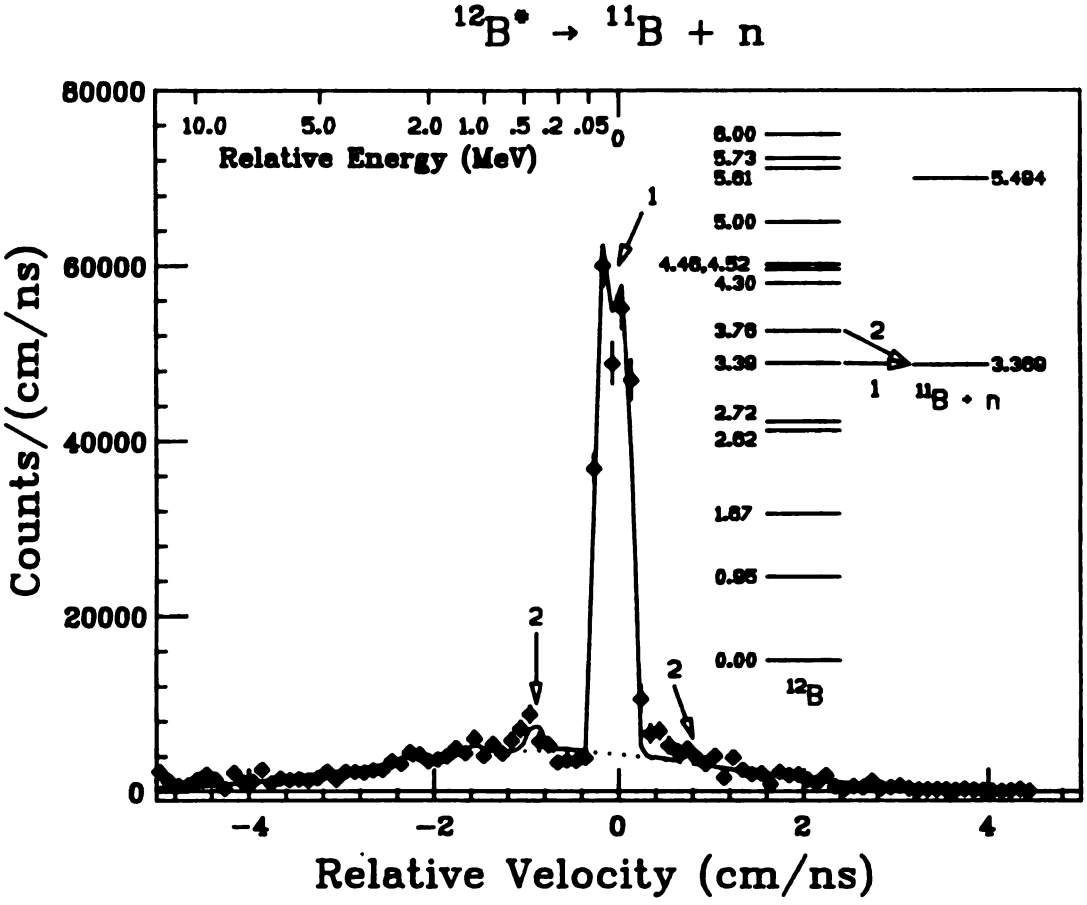

Figure III.7 - Relative velocity spectrum for ^{11}B + n at 31° and for $E_{^{11}B} \geq 6$ MeV/A. The numbered locations correspond to relative velocities that come from the decays indicated in the energy level diagram. A relative energy scale is included for reference. The solid line is from a fit described in the text, and the dotted line shows the background used in the fit (a Gaussian).

relative velocity spectrum, and it will be centered at 0 cm/ns. Such a case is best shown in Figure III.7, where the central peak is due to the decay of the 3.388-MeV state of ^{12}B to the ground state of ^{11}B. For this decay, the decay energy is only 18 keV, and the geometrical efficiency is about 33% (note that this value of the geometrical efficiency is much greater than the percentage of the available solid angle in the lab taken up by the neutron detectors, which is about 0.17% - thus the kinematical focussing increases the counting rate by a factor of ~200). Since the efficiency is less than 100%, one might expect the forward and backward peaks to be separated. Although there is a dip in the peak at 0 cm/ns, clearly the forward and backward peaks are unresolved from each other. The reason they are unresolved is due to the instrumental resolution. Hence, only one peak is observed for this decay.

For this experiment, the relative velocity resolution, dv_{rel}, was about 2 mm/ns for all of the spectra. The corresponding relative energy resolution is related to the relative velocity resolution by $dE_{rel}=\mu v_{rel} dv_{rel}$, where μ is the reduced mass of the daughter-fragment/neutron system. Thus, as the decay energy increases, the relative energy resolution gets worse, even though the relative velocity resolution remains the same. Because of this, the ability to resolve individual decays decreases as the decay energy increases. Figure III.5 shows the relative energy resolution for two of the decays. For E_{rel}= 0.1 MeV, for example, dE_{rel}= 90 keV, whereas for E_{rel}= 2 MeV, dE_{rel}= 450 keV, and for E_{rel}= 2.6 MeV, dE_{rel}= 510 keV. The energy resolution at a particular value of relative velocity will vary slightly, of course, depending on the mass of the fragment in question, but not by much.

Since the geometrical efficiency for all the detected decays was less than 100%, it had to be calculated in order for the total population of the neutron-unbound states to be extracted from the relative velocity spectra. Fragment and neutron detector sizes and flight paths, initial fragment velocity, level decay energies and level widths all have an

effect on the geometrical efficiency, and were put into the Monte Carlo code MONTRES (Deak87), which simulates the decay of neutron-unbound states into the detection system. Conditions which affect the energy determination of the fragments, such as silicon detector resolution and target thickness, and conditions which affect the timing resolution of the neutron detectors, such as detector thickness and intrinsic timing resolution, are also put into the code. The solid lines in Figures III.5 and III.7 show the fits to the data using the decay simulations from MONTRES added onto a background. The spectral resolution and spectral shapes are matched well with the simulations. It should be noted here that the decay is assumed to be isotropic in the rest frame of the parent fragment. Data from another experiment that used the same system as ours has been analyzed to test this assumption on states that decay by emission of charged particles (Naya90), and no evidence has been found that contradicts it.

It should also be noted that for all cases except one, the level widths used in the simulations are taken as constants in Lorentzian resonance functions. The one exception is for the decay of the 7.46-MeV state in ^{7}Li to the ground state of ^{6}Li. Here the reported width, 89 keV (Ajze84), is close enough to the decay energy, 210 keV, to take into account the energy dependence of the width. The energy dependence was calculated using penetrabilities from Mona58. More details regarding this case may be found in Appendix D.

The precise nature of the background in the spectra shown in Figures III.5 and III.7 is not known. A background has been calculated using random coincidences between fragments and neutrons and has been used in previous analyses (Bloc87, Kiss87), although it cannot account for all the background. It is a broad Gaussian whose peak is, in general, at some nonzero value of relative velocity. The dotted lines in Figures III.5 and III.7 show this type of background. In order to estimate the effect the uncertainty in background determination had on the extacted level populations, all the spectra were fitted using at least two types of backgrounds. The background just

mentioned was always used, and others that were used are Cauchy backgrounds, Tippet functions, and linear backgrounds. An average population from all backgrounds was calculated, and the deviation from the average was used as the uncertainty in the population due to the background.

In addition to the uncertainty in the population due to the background, statistical uncertainties and systematic errors (such as an assumed detector misalignment, current integrator error, target thickness nonuniformity, etc.) were also included in the final uncertainties reported for the populations, ratios, and temperatures. In most cases, the background uncertainty and statistical error were the main contributors to the final uncertainty.

Chapter IV: Results

A. IMF Singles Spectra

Figures IV.1, IV.2, and IV.3 contain the fragment singles spectra for selected isotopes and 15°, 31°, and 64°, respectively. The solid lines in each plot in Figures IV.1 and IV.2 indicate fits to the singles spectra using the sum of two functions which are represented with the dotted and dashed lines. The dotted lines show the fits to the deep-inelastic parts of the spectra with the function:

$$F_{DI} = N_{DI} \times (E/A) \times \exp(-E\rho) \qquad \text{(IV.1)}$$

where N_{DI} and ρ are the fit parameters, A is the mass number, and E is the kinetic energy of the fragment. The dashed lines show the fits to the quasielastic parts with the function:

$$F_{QE} = N_{QE} \times \sqrt{(E/A)} \times \exp[a\sqrt{(E/A)}] \times \{1+\exp[b(E/A-E_o/A)]\}^{-1} \qquad \text{(IV.2)}$$

where N_{QE}, a, b, and E_o are the fit parameters. The parameterization of the QE data is the same as the one used in Kiss89. This parameterization is used to estimate the percentage of QE IMFs and DI IMFs in the bound-state yields at 15° and 31° for various cuts on IMF kinetic energy, which in turn are used to identify the regions of IMF kinetic energy that are dominated either by QE or DI reaction mechanisms. It is assumed that these

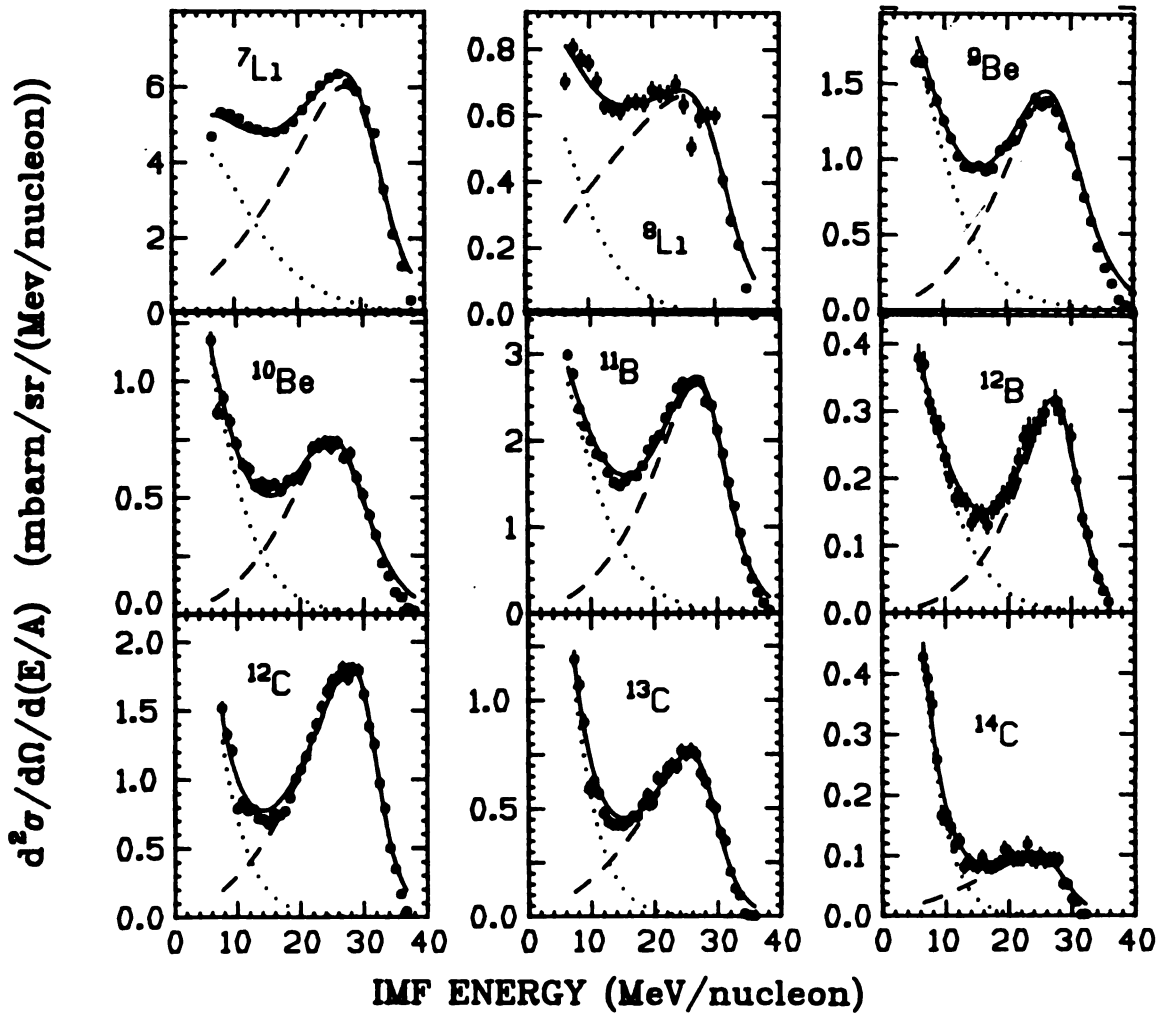

Figure IV.1 - Fragment singles spectra for 15°. The solid, dotted, and dashed lines come from a fit using Equations IV.1 and IV.2.

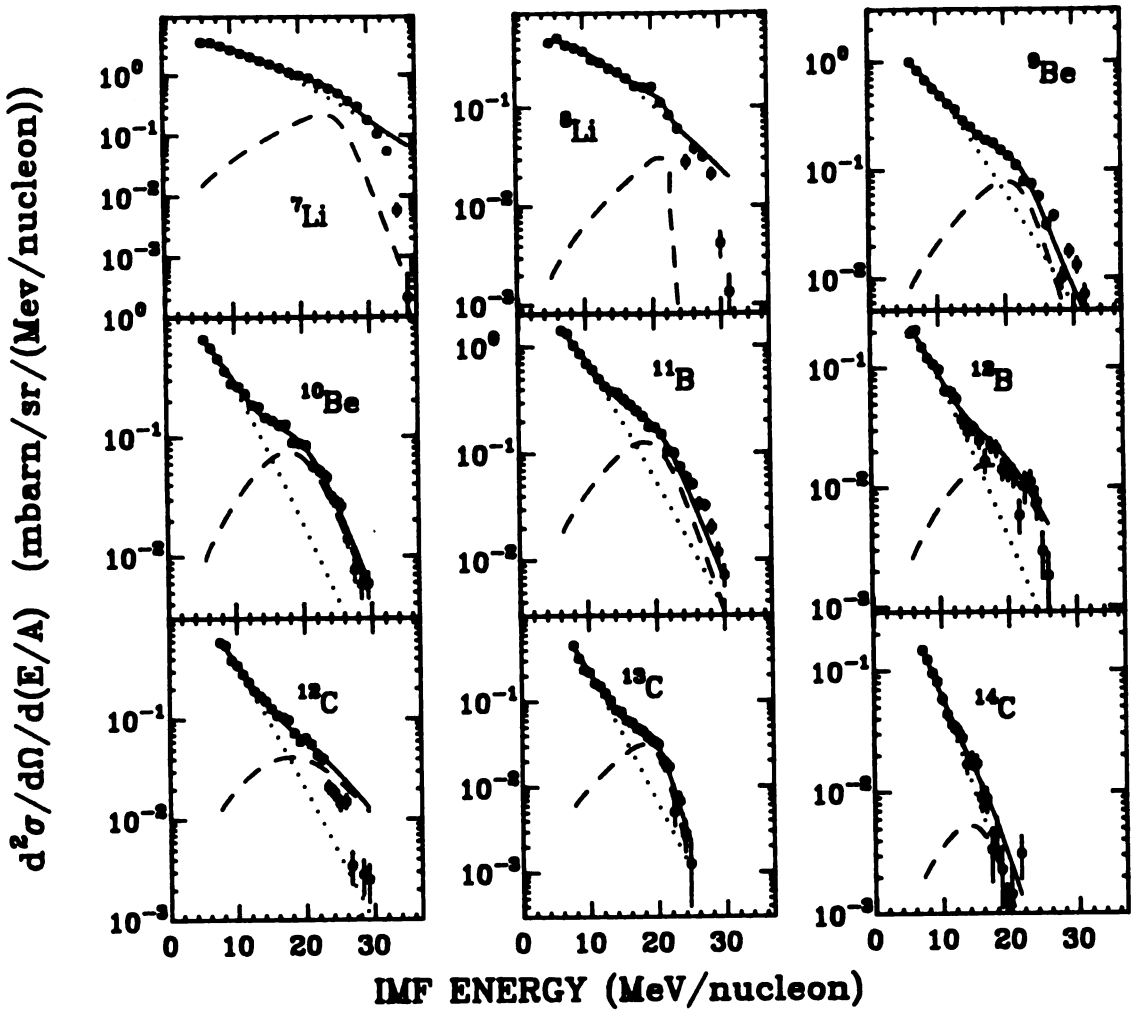

Figure IV.2 - Fragment singles spectra for 31°. The solid, dotted, and dashed lines come from a fit using Equations IV.1 and IV.2

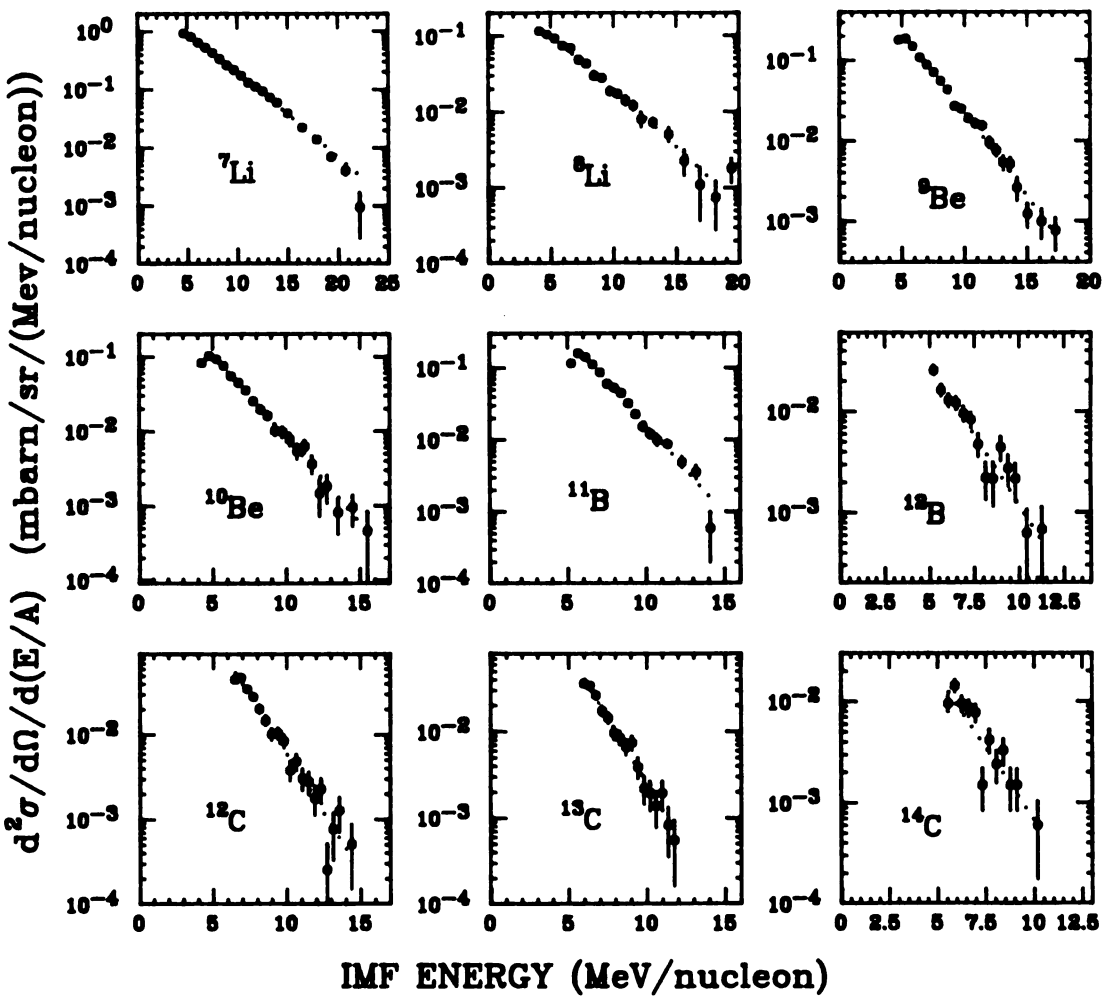

Figure IV.3 - Fragment singles spectra for 64°. The dotted lines come from a fit using Equation IV.1.

regions are the same for unbound-state IMF production as for bound-state IMF production. Table IV.1 shows the percentage of QE IMFs in the bound-state yield for various cuts on IMF kinetic energy at 15° and 31°. All of the yield at 64° is assumed to come from DI reactions. No IMF data below a kinetic energy of 6 MeV/nucleon was used in this thesis.

Tables IV.2 - IV.5 contain the energy-integrated cross sections for the isotopes of lithium, beryllium, boron, and carbon, respectively, for the kinetic-energy gates used in this thesis. These cross sections were used as the values of the bound-state populations extracted from the IMF singles analysis. Two sets of vaules are given for ^{7}Li in Table IV.2, one for the values extracted from the original ^{7}Li spectra, and another for the values extracted after correcting the spectra for ^{8}Be contamination. Appendix C explains how the ^{7}Li spectra were corrected for this contamination.

B. IMF - Neutron Coincidence Data

Unbound-state populations were determined from analyses of relative velocity spectra such as the ones in Figures III.5 and III.7. For all of the relative velocity plots shown in this chapter, fits to the data are indicated with the solid line, and the background used in the fitting procedure is indicated with the dotted line (for details on the fitting procedure, see Chapter III). In total, 16 populations from neutron-unbound states were measured from nine different isotopes. Unless otherwise noted, the level energies, spins, and widths for all the states mentioned in subsections 1-9 come from Ajze84, Ajze86, and Ajze90. All of the unbound-state populations reported in subsections 1-9 are the cross sections for a particular neutron-decay branch, and they are not corrected for any branching ratios. In order to calculate the total population for a particular unbound state, it will be necessary to divide the reported cross section by the branching ratio for neutron decay.

Table IV.1 - Percentage of QE fragments as determined by fits to inclusive IMF spectra using Equations IV.1 and IV.2 of the text for various cuts on IMF kinetic energy (in MeV) at 15° and 31°. Typical uncertainties of the fits are from ± 1% to ± 3%.

isotope	15° E/A ≥ 15	15° 6 ≤ E/A ≤ 15	15° 6 ≤ E/A ≤ 10	31° E/A ≤ 6	31° 6 ≤ E/A ≤ 15
^{7}Li	87 %	37 %	26 %	7 %	2 %
^{8}Li	94 %	55 %	43 %	5 %	2 %
^{9}Be	90 %	22 %	11 %	13 %	5 %
^{10}Be	92 %	22 %	11 %	24 %	11 %
^{11}B	90 %	22 %	11 %	16 %	7 %
^{12}B	90 %	14 %	6 %	19 %	8 %
^{12}C	97 %	31 %	16 %	15 %	6 %
^{13}C	96 %	25 %	12 %	10 %	5 %
^{14}C	94 %	18 %	9 %	7 %	6 %

Table IV.2 - Energy-integrated cross sections for lithium isotopes detected at 15°, 31°, and 64°. The units are mb/sr, and the uncertainties in the last significant digit(s) are written in the parentheses following each value of the cross section. The uncertainties are due to statistical errors only. The values under the ^{7}Li(a) column are the cross sections before correcting for ^{8}Be contamination, and the values under the ^{7}Li(b) are after the correction.

15°

Energy Range	^{6}Li	^{7}Li(a)	^{7}Li(b)	^{8}Li	^{9}Li
6-40 MeV/A	108.2(3)	154.2(4)	140.4(4)	17.44(14)	2.08(11)
6-15 MeV/A	26.50(14)	45.5(2)	43.62(18)	6.37(7)	
15-40 MeV/A	81.9(3)	108.7(3)	96.8(3)	11.07(12)	
6-10 MeV/A	11.48(9)	20.62(15)	19.98(12)	3.08(5)	
10-15 MeV/A	15.01(11)	24.88(14)	23.64(14)	3.29(5)	
15-20 MeV/A	16.44(11)	24.50(14)	22.56(14)	3.20(6)	
20-25 MeV/A	19.41(13)	29.01(15)	26.06(15)	3.38(6)	
25-30 MeV/A	21.52(14)	30.62(16)	26.83(16)	2.28(6)	
30-40 MeV/A	24.35(17)	24.59(15)	21.34(15)	1.61(5)	

31°

Energy Range	^{6}Li	^{7}Li(a)	^{7}Li(b)	^{8}Li	^{9}Li
6-40 MeV/A	24.09(9)	34.93(11)	29.75(16)	4.57(4)	0.96(2)
6-15 MeV/A	13.80(7)	22.77(8)	19.33(13)	3.11(3)	
15-40 MeV/A	10.29(6)	12.16(7)	10.42(10)	1.46(3)	
6-8 MeV/A	3.81(3)	6.81(4)	5.84(7)	0.91(2)	
8-10 MeV/A	3.36(3)	5.73(4)	4.88(6)	0.79(2)	
10-12 MeV/A	2.93(3)	4.69(4)	3.95(6)	0.63(2)	
12-16 MeV/A	4.76(4)	7.70(5)	5.95(7)	0.99(2)	
16-22 MeV/A	5.00(4)	6.56(5)	5.52(7)	0.93(2)	
22-40 MeV/A	4.23(4)	4.07(4)	3.60(6)	0.32(1)	

Table IV.2 (cont'd.).

	64°				
Energy Range	^{6}Li	^{7}Li(a)	^{7}Li(b)	^{8}Li	^{9}Li
6-40 MeV/A	1.750(14)	2.028(15)	1.83(2)	0.206(5)	

Table IV.3 - Energy-integrated cross sections for beryllium isotopes detected at 15°, 31°, and 64°. The units are mb/sr, and the uncertainties in the last significant digit(s) are written in the parentheses following each value of the cross section. The uncertainties are due to statistical errors only.

15°

Energy Range	^{7}Be	^{9}Be	^{10}Be
6-40 MeV/A	47.55(19)	34.13(16)	17.75(12)
6-15 MeV/A			6.60(7)
15-40 MeV/A			11.14(10)
6-10 MeV/A			3.59(5)
10-14 MeV/A			2.46(4)
14-18 MeV/A			2.20(4)
18-22 MeV/A			2.47(4)
22-26 MeV/A			2.87(5)
26-30 MeV/A			2.57(5)
30-40 MeV/A			1.59(4)

31°

Energy Range	^{7}Be	^{9}Be	^{10}Be
6-40 MeV/A	7.96(6)	6.28(5)	3.53(4)
6-15 MeV/A			2.64(3)
15-40 MeV/A			0.89(2)
6-10 MeV/A			1.65(2)
10-14 MeV/A			0.85(2)
14-40 MeV/A			1.04(2)

64°

Energy Range	^{7}Be	^{9}Be	^{10}Be
6-40 MeV/A		0.293(6)	0.121(4)

Table IV.4 - Energy-integrated cross sections for boron isotopes detected at 15°, 31°, and 64°. The units are mb/sr, and the uncertainties in the last significant digit(s) are written in the parentheses following each value of the cross section. The uncertainties are are due to statistical errors only.

	15°	
Energy Range	^{11}B	^{12}B
6-40 MeV/A	58.41(21)	6.09(7)
6-15 MeV/A	18.37(11)	2.10(4)
15-40 MeV/A	40.04(17)	3.99(6)
6-8 MeV/A	5.69(6)	0.70(2)
8-10 MeV/A	4.31(5)	0.55(2)
10-12 MeV/A	3.69(5)	0.39(2)
12-14 MeV/A	3.19(5)	0.32(1)
14-16 MeV/A	3.02(4)	0.29(2)
16-18 MeV/A	3.18(5)	0.28(1)
18-20 MeV/A	3.68(5)	0.33(2)
20-22 MeV/A	4.23(6)	0.42(2)
22-24 MeV/A	4.91(6)	0.52(2)
24-26 MeV/A	5.30(6)	0.57(2)
26-28 MeV/A	5.28(6)	0.58(2)
28-30 MeV/A	4.73(6)	0.50(2)
30-32 MeV/A	3.58(5)	0.39(2)
32-34 MeV/A	2.28(4)	0.18(1)

Table IV.4 (cont'd.).

	31°	
Energy Range	^{11}B	^{12}B
6-40 MeV/A	8.58(5)	0.983(18)
6-15 MeV/A	6.71(5)	0.832(16)
15-40 MeV/A	1.87(2)	0.151(8)
6-8 MeV/A	2.64(3)	0.358(10)
8-10 MeV/A	1.71(2)	0.218(8)
10-12 MeV/A	1.18(2)	0.138(7)
12-14 MeV/A	0.81(2)	0.085(5)
14-16 MeV/A	0.68(1)	0.058(4)
16-18 MeV/A	0.51(1)	0.042(4)
18-22 MeV/A	0.66(1)	0.054(5)
22-40 MeV/A	0.39(1)	0.030(4)

	64°	
Energy Range	^{11}B	^{12}B
6-40 MeV/A	0.260(5)	0.0239(17)

Table IV.5 - Energy-integrated cross sections for carbon isotopes detected at 15°, 31°, and 64°. The units are mb/sr, and the uncertainties int the last significant digit(s) are written in the parentheses following each value of the cross section. The uncertainties are due to statistical errors only.

15°

Energy Range	^{12}C	^{13}C	^{14}C
6-40 MeV/A	32.98(16)	15.92(11)	3.10(5)
6-15 MeV/A	7.76(8)	5.58(7)	1.75(4)
15-40 MeV/A	25.23(14)	10.04(9)	1.35(3)
6-10 MeV/A	3.95(6)	3.44(5)	
10-15 MeV/A	3.81(5)	2.44(4)	
15-20 MeV/A	4.19(6)	2.44(4)	
20-25 MeV/A	7.03(7)	3.45(5)	
25-30 MeV/A	8.81(8)	3.23(5)	
30-40 MeV/A	5.19(6)	0.91(3)	

31°

Energy Range	^{12}C	^{13}C	^{14}C
6-40 MeV/A	3.19(3)	2.14(3)	0.606(16)
6-15 MeV/A	7.76(3)	1.86(2)	
15-40 MeV/A	0.648(14)	0.28(1)	

64°

Energy Range	^{12}C	^{13}C	^{14}C
6-40 MeV/A	0.103(3)	0.059(2)	0.0159(13)

1. 6Li + n

Figure IV.4 shows the relative velocity spectrum for ^{6}Li + neutron coincidence events at 15° and for ^{6}Li kinetic energies between 6 and 40 MeV/nucleon. It shows a pronounced resonance at v_{rel}= ±0.6 cm/ns, which is due to the decay of the 7.456-MeV state in ^{7}Li ($J^{\pi}=5/2^-$, Γ=89 keV, Γ_n/Γ_{tot}= 0.776) to the ground state of ^{6}Li. An energy level diagram is included in the righthand portion of the plot illustrating the observed resonance. This resonance was also seen at 31° and 64°. The relative velocity spectra at 31° and 64° for ^{6}Li kinetic energies between 6 and 40 MeV/nucleon are shown in Figure IV.5.

Statistics were good enough at 15° and 31° to determine the 7.456-MeV state population gated on small cuts in the ^{6}Li fragment kinetic energy. Figure IV.6 shows the relative velocity spectra for ^{6}Li + n at 15° for gates on ^{6}Li kinetic energy of 6-10 MeV/nucleon, 10-15 MeV/nucleon, 15-20 MeV/nucleon, 20-25 MeV/nucleon, 25-30 MeV/nucleon, and 30-40 MeV/nucleon. Figure IV.7 shows the relative velocity spectra for ^{6}Li + n at 31° for gates on ^{6}Li kinetic energy of 6-8 MeV/nucleon, 8-10 MeV/nucleon, 10-12 MeV/nucleon, 12-16 MeV/nucleon, 16-22 MeV/nucleon, and 22-40 MeV/nucleon.

In addition to the kinetic-energy gates already mentioned for 15°, the population of the 7.456-MeV state was also determined at 15° for kinetic-energy gates of 6-15 MeV/nucleon and 15-40 MeV/nucleon. Instead of simply adding spectra for smaller cuts to determine these two spectra (for example, adding the 6-10 MeV/nucleon and 10-15 MeV/nucleon spectra together to get the 6-15 MeV/nucleon spectrum), they were generated using the analysis described in Chapter III, which was the method used for all the other spectra. Figure IV.8 shows the relative velocity spectra for the two energy gates of 6-15 MeV/nucleon and 15-40 MeV/nucleon. Table IV.6 contains the

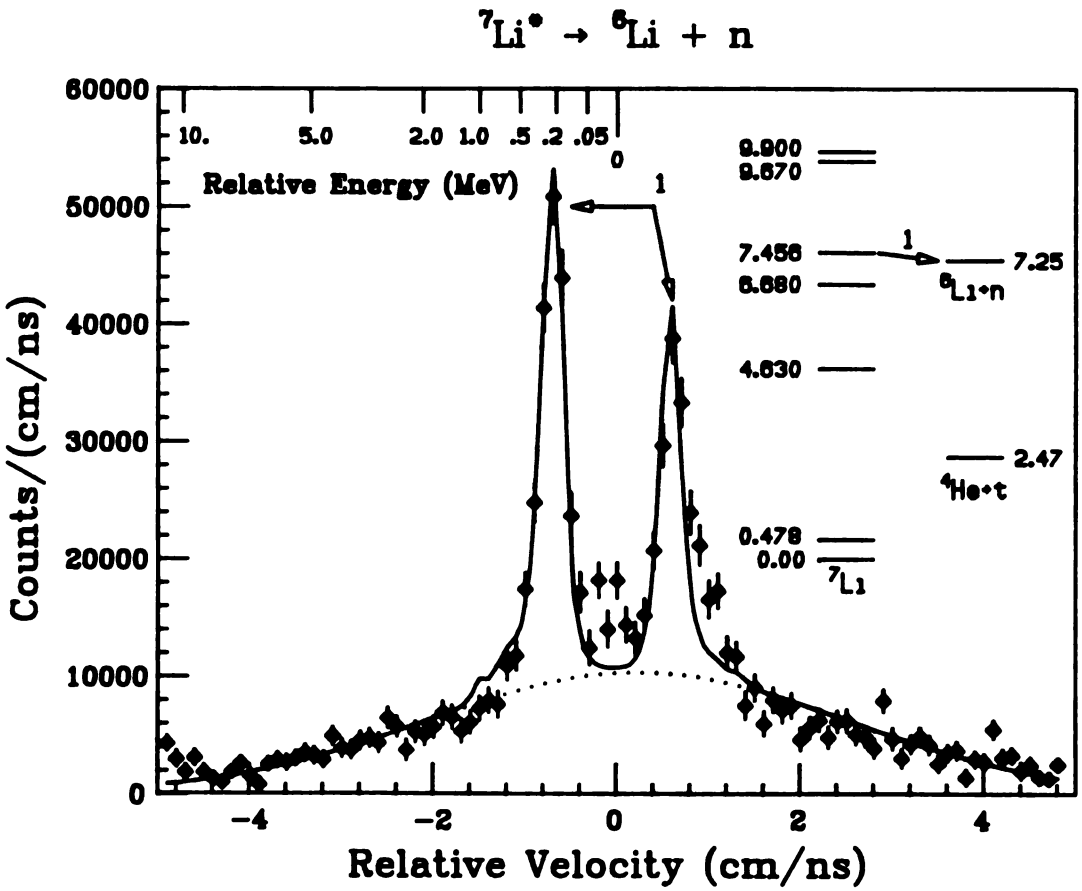

Figure IV.4 - Relative velocity spectrum for $^7Li + n$ at 15°. The resonance comes from the decay indicated in the energy level diagram. A relative energy scale is included for reference. The line shows a fit to the data that is explained in the text. The dotted line shows the background used.

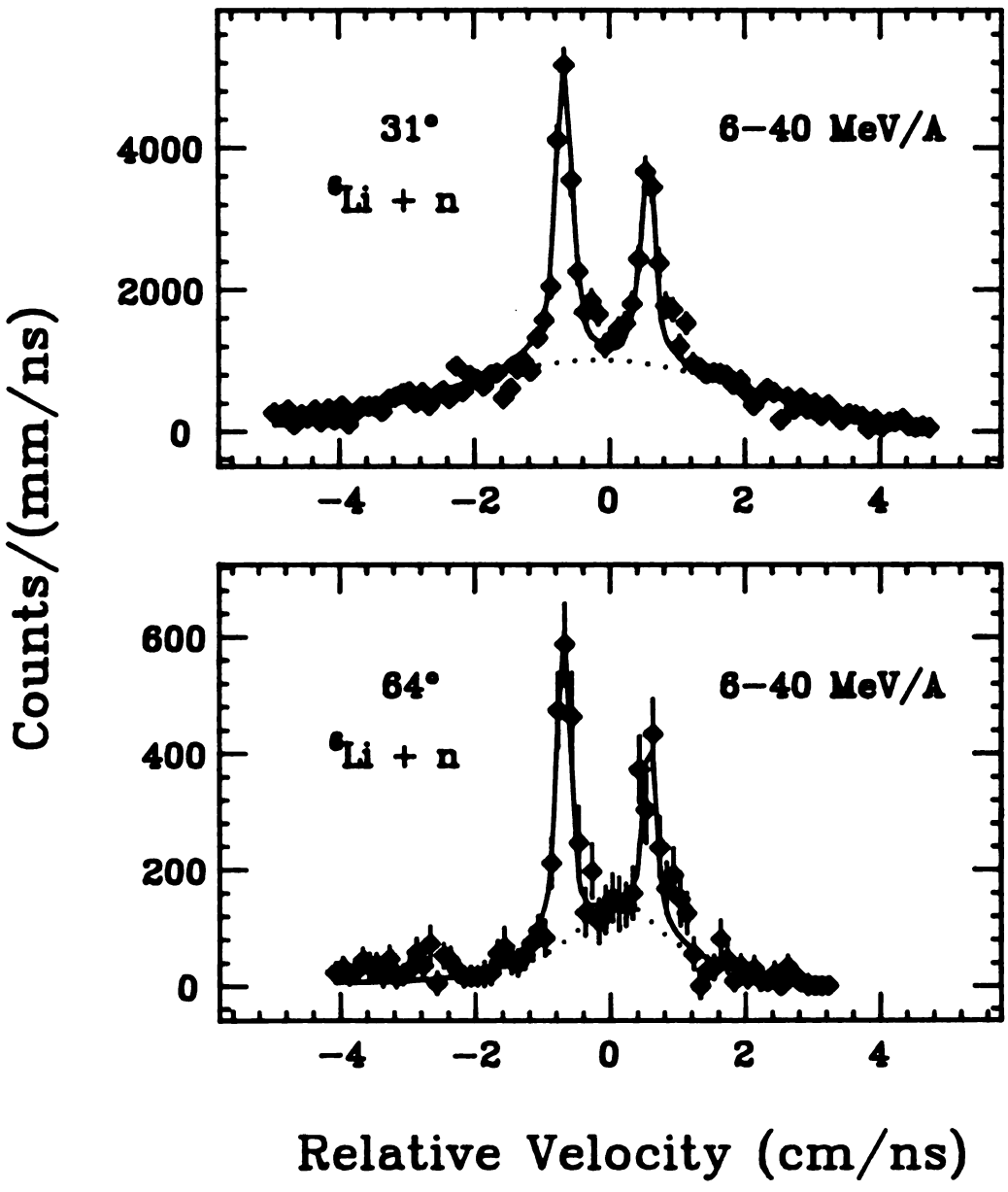

Figure IV.5 - Relative velocity spectra for ^{6}Li + n at 31° and 64° and for all ^{6}Li kinetic energies above 6 MeV/A.

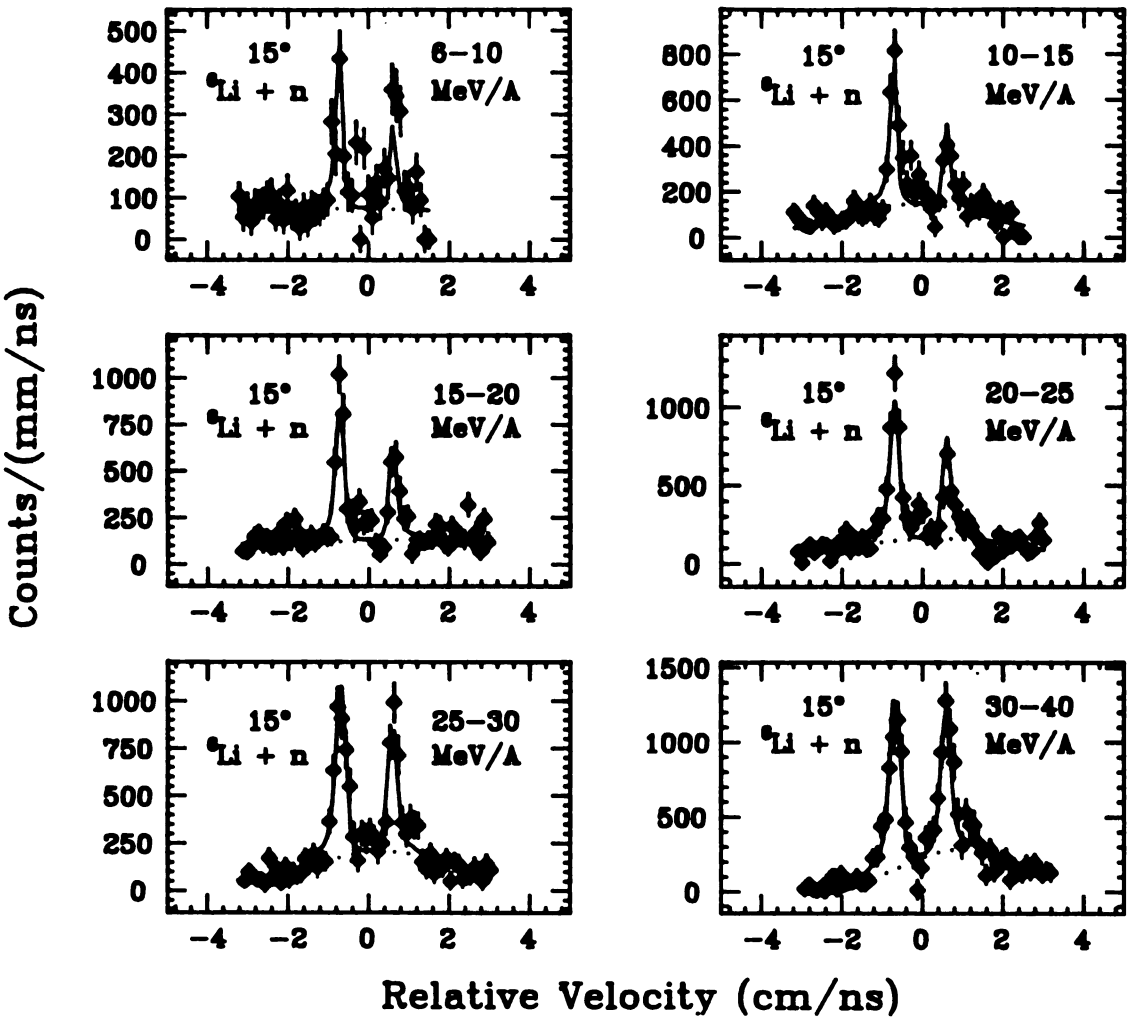

Figure IV.6 - Relative velocity spectra for ^{6}Li + n at 15° and for the indicated cuts on ^{6}Li kinetic energy.

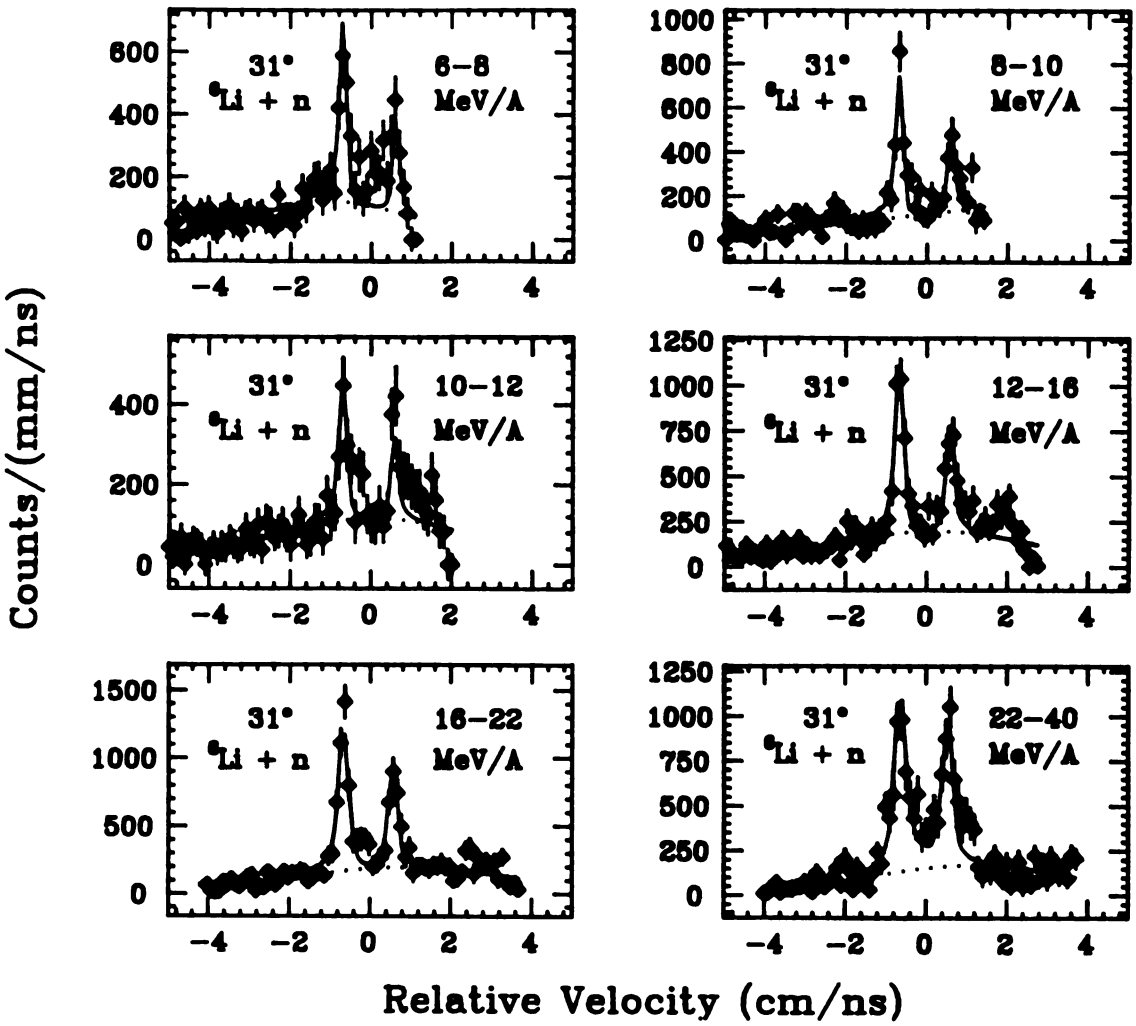

Figure IV.7 - Relative velocity spectra for ^{6}Li + n at 31° and for the indicated cuts on ^{6}Li kinetic energy.

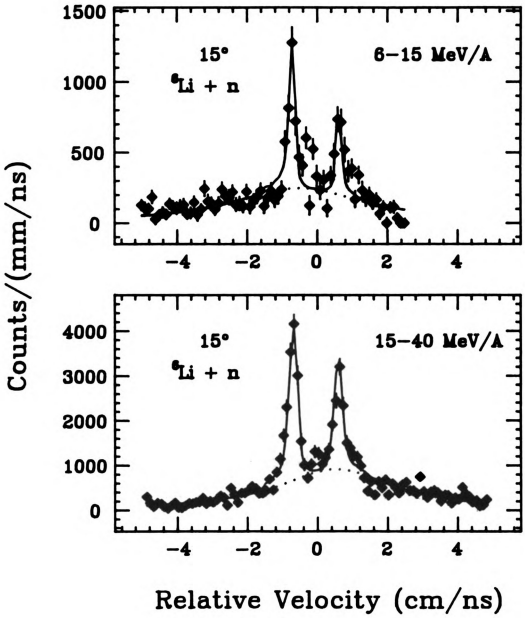

Figure IV.8 - Relative velocity spectra for ^{6}Li + n at 15° and for cuts on ^{6}Li kinetic energy from 6-15 MeV/A and 15-40 MeV/A.

Table IV.6 - Populations of the 7.46-MeV state in ^{7}Li for the indicated cuts on ^{6}Li kinetic energy and for the indicated angles. The units are in mb/sr, and the uncertainty in the last significant digit(s) is written in the parenthesis following each value of the population.

15°		31°	
Energy Range	Population	Energy Range	Population
6-40 MeV/A	5.44(30)	6-40 MeV/A	1.19(7)
6-15 MeV/A	2.10(14)	6-15 MeV/A	0.79(5)
15-40 MeV/A	4.04(17)	15-40 MeV/A	0.49(2)
6-10 MeV/A	0.93(10)	6-8 MeV/A	0.26(4)
10-15 MeV/A	1.03(8)	8-10 MeV/A	0.25(2)
15-20 MeV/A	1.04(7)	10-12 MeV/A	0.119(15)
20-25 MeV/A	1.05(7)	12-16 MeV/A	0.270(18)
25-30 MeV/A	0.98(6)	16-22 MeV/A	0.273(14)
30-40 MeV/A	1.15(5)	22-40 MeV/A	0.204(15)

64°	
Energy Range	Population
6-40 MeV/A	0.153(12)

populations of the 7.456-MeV state of ^{7}Li extracted from the spectra shown in Figures IV.4-8. All populations are reported as cross sections in units of mb/sr.

2. 7Li + n

The relative velocity spectra for ^{7}Li + n show a resonance at ±0.6 cm/ns at all three angles, which is due to the decay of the 2.255-MeV state of ^{8}Li ($J^{\pi} = 3^{+}$, Γ = 33 keV) to the ground state of ^{7}Li. Figure IV.9 shows such a spectrum for $\theta_{^{7}Li}$= 15°, 6 MeV/nucleon ≤ $E_{^{7}Li}$ ≤ 40 MeV/nucleon. Included in Figure IV.9 are an energy level diagram and a relative energy scale for reference. As was the case for ^{6}Li + n, statistics were good enough at 15° and 31° to allow the population of the 2.255-MeV state in ^{8}Li to be determined for the same gates on the fragment kinetic energy as the ones for ^{6}Li + n. Figure IV.10 shows the spectra for ^{7}Li + n at 15° for all 6 cuts on ^{7}Li kinetic energy, and Figure IV.11 shows the spectra for ^{7}Li + n at 31° for the indicated cuts on ^{7}Li energy. Figure IV.12 shows the relative velocity spectra for ^{7}Li + n at 15° for cuts of 6-15 MeV/nucleon and 15-40 MeV/nucleon on ^{7}Li kinetic energy. Figure IV.13 shows the relative velocity spectra for ^{6}Li + n at 31° and 64° for energies between 6 and 40 MeV/nucleon. The populations extracted from the spectra shown in Figures IV.9-13 are contained in Table IV.7 in units of mb/sr.

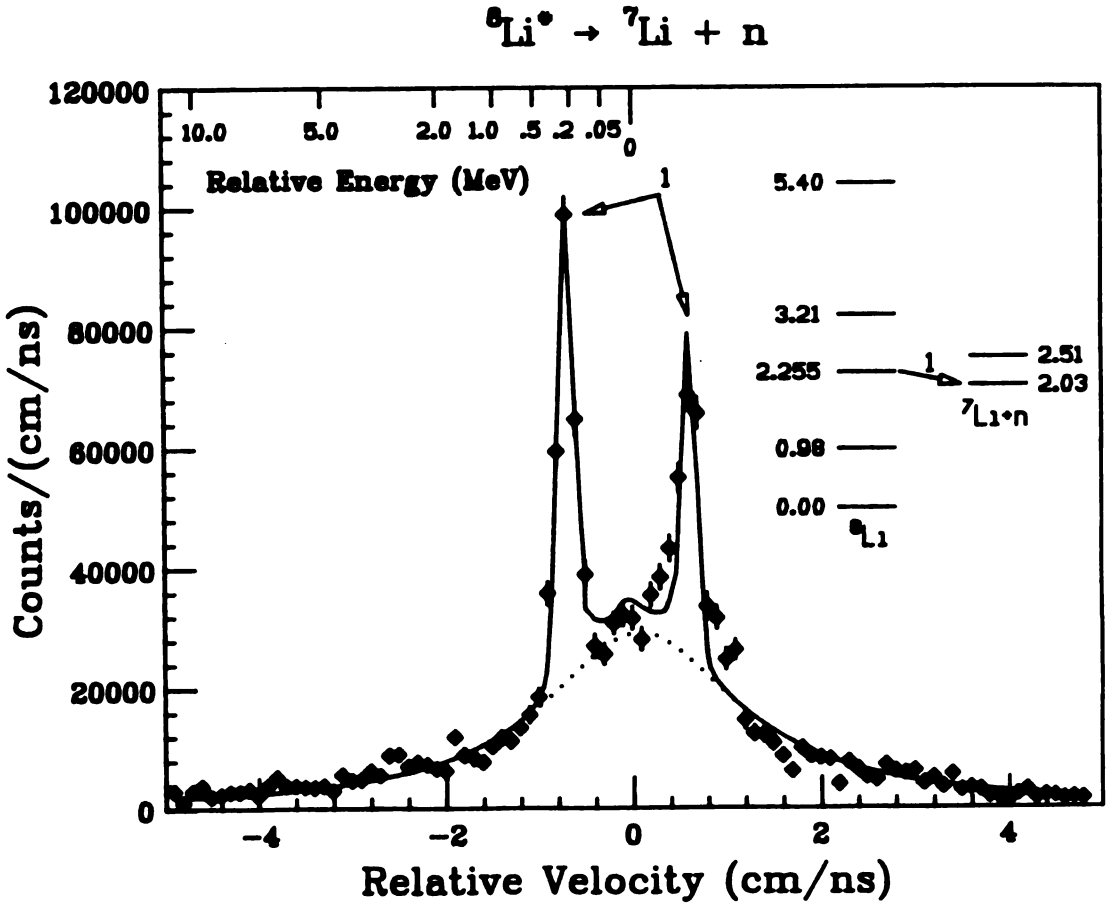

Figure IV.9 - Relative velocity spectrum for ^{7}Li + n at 15°. The resonance comes from the decay indicated in the energy level diagram. A relative energy scale is included for reference. The line shows a fit to the data that is explained in the text. The dotted line shows the background used.

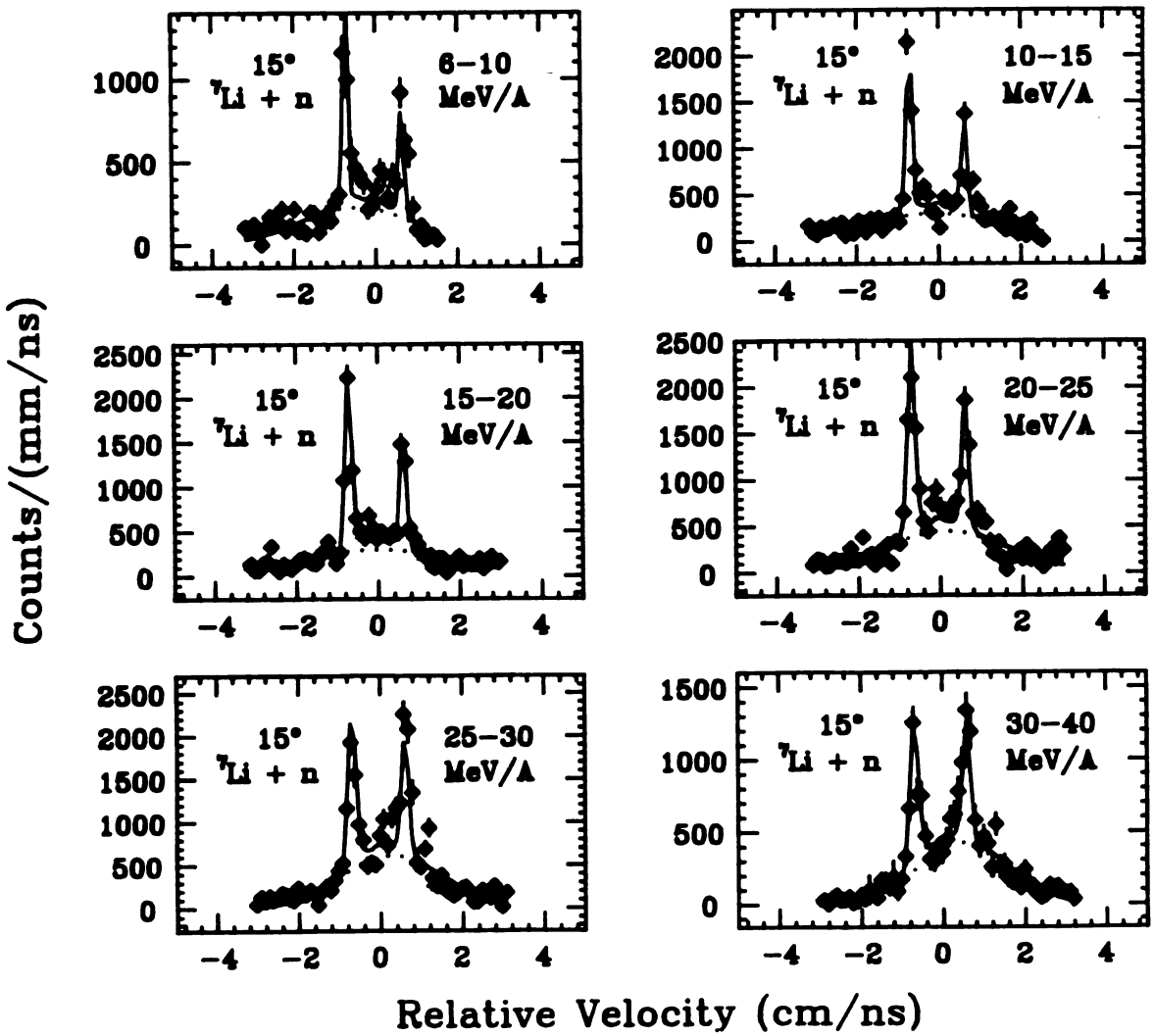

Figure IV.10 - Relative velocity spectra for ^{7}Li + n at 15° and for the indicated cuts on ^{7}Li kinetic energy.

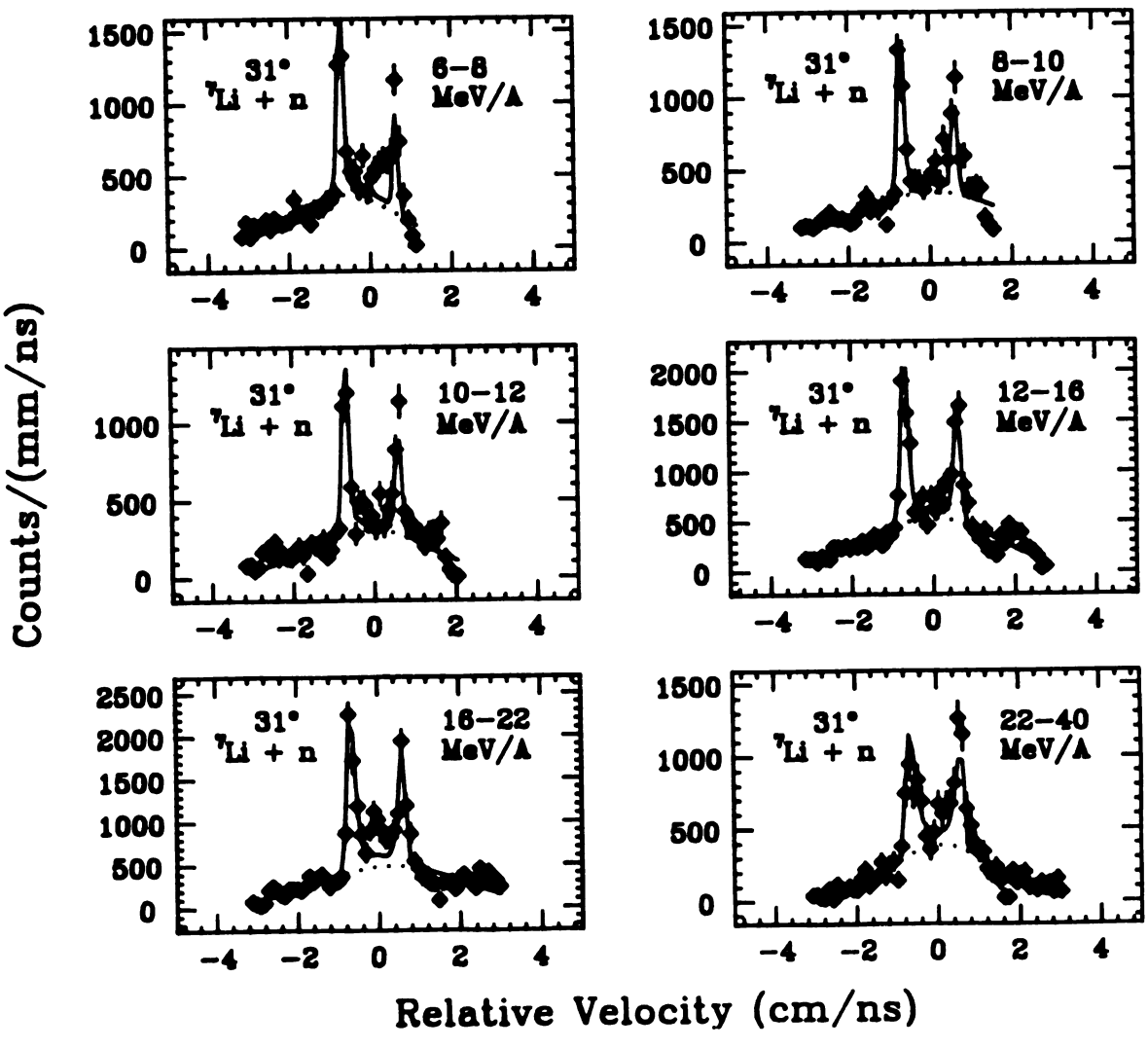

Figure IV.11 - Relative velocity spectra for ^{7}Li + n at 31° and for the indicated cuts on ^{7}Li kinetic energy.

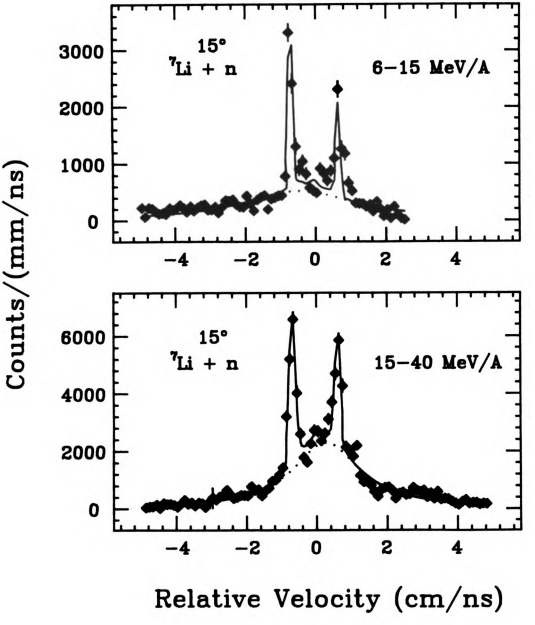

Figure IV.12 - Relative velocity spectra for ^{7}Li + n at 15° and for cuts on ^{7}Li kinetic energy from 6-15 MeV/A and 15-40 MeV/A.

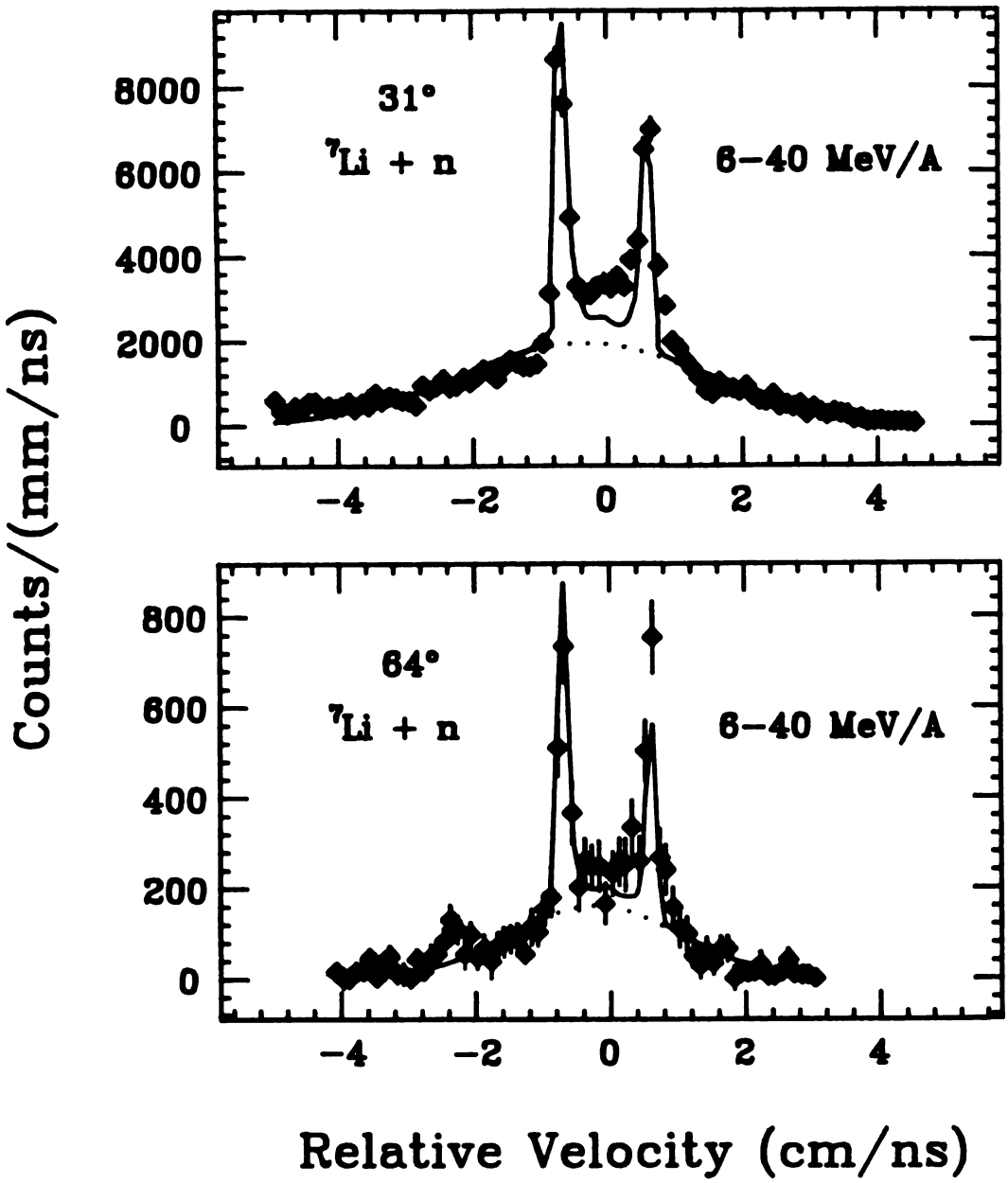

Figure IV.13 - Relative velocity spectra for ⁷Li + n at 31° and 64° and for all ⁷Li kinetic energies above 6 MeV/A.

Table IV.7 - Populations of the 2.255-MeV state in ^{8}Li for the indicated cuts on ^{7}Li kinetic energy and for the indicated angles. The units are in mb/sr, and the uncertainty in the last significant digit(s) is written in the parenthesis following each value of the population.

15°		31°	
Energy Range	Population	Energy Range	Population
6-15 MeV/A	3.57(17)	6-40 MeV/A	1.44(12)
15-40 MeV/A	4.16(33)	6-8 MeV/A	0.36(3)
6-10 MeV/A	1.64(11)	8-10 MeV/A	0.268(19)
10-15 MeV/A	1.75(8)	10-12 MeV/A	0.226(15)
15-20 MeV/A	1.54(8)	12-16 MeV/A	0.294(16)
20-25 MeV/A	1.40(8)	16-22 MeV/A	0.277(21)
25-30 MeV/A	1.17(5)	22-40 MeV/A	0.113(8)
30-40 MeV/A	0.60(3)		

64°	
Energy Range	Population
6-40 MeV/A	0.129(9)

3. 8Li + n

The decay of the 4.296-MeV state in ^{8}Li (J = 5/2, Γ = 60 ± 45 keV) to the ground state of ^{8}Li is observed at 15° and 31°. Figure IV.14 shows the relative velocity spectrum for ^{8}Li + n at 15° along with an energy-level diagram for ^{9}Li with the detected decay of the 4.296-MeV state indicated with the arrow. Figure IV.15 shows the relative velocity spectrum for ^{8}Li + n at 31°. The energy range used for both of the spectra in Figures IV.14 and IV.15 is 6-40 MeV/nucleon. The energy and width of this state come from a separate analysis of this data (see Appendix B). The spin used for this state comes from Youn71. The population of the 4.3-MeV state in ^{9}Li at 15° is 0.74 ± 0.17 mb/sr, and the population at 31° is 0.17 ± 0.05 mb/sr.

4. 7Be + n

The neutron decay of the 19.234-MeV ($J^{\pi}= 3^{+}$, Γ = 210 keV) state in ^{8}Be to the ground state of ^{7}Be is seen as the set of peaks at ± 0.9 cm/ns and the peak at 0 cm/ns in relative velocity spectra for ^{7}Be + n at 15° and 31° in Figures IV.16 and IV.17, respectively. Both figures show spectra for ^{7}Be kinetic energies between 6 and 40 MeV/nucleon. Included in Figure IV.16 is an energy level diagram for ^{8}Be showing the decay observed in the spectrum. The energy and spin of this state come from a separate analysis of the ^{7}Be + n data (see Appendix B). The population of the 19.24-MeV state in ^{8}Be at 15° is 1.91 ± 0.11 mb/sr, and the population at 31° is 0.2465 ± 0.025 mb/sr. It is assumed that nearly 100% of the decay of the 19.24-MeV state in ^{8}Be is through the neutron branch.

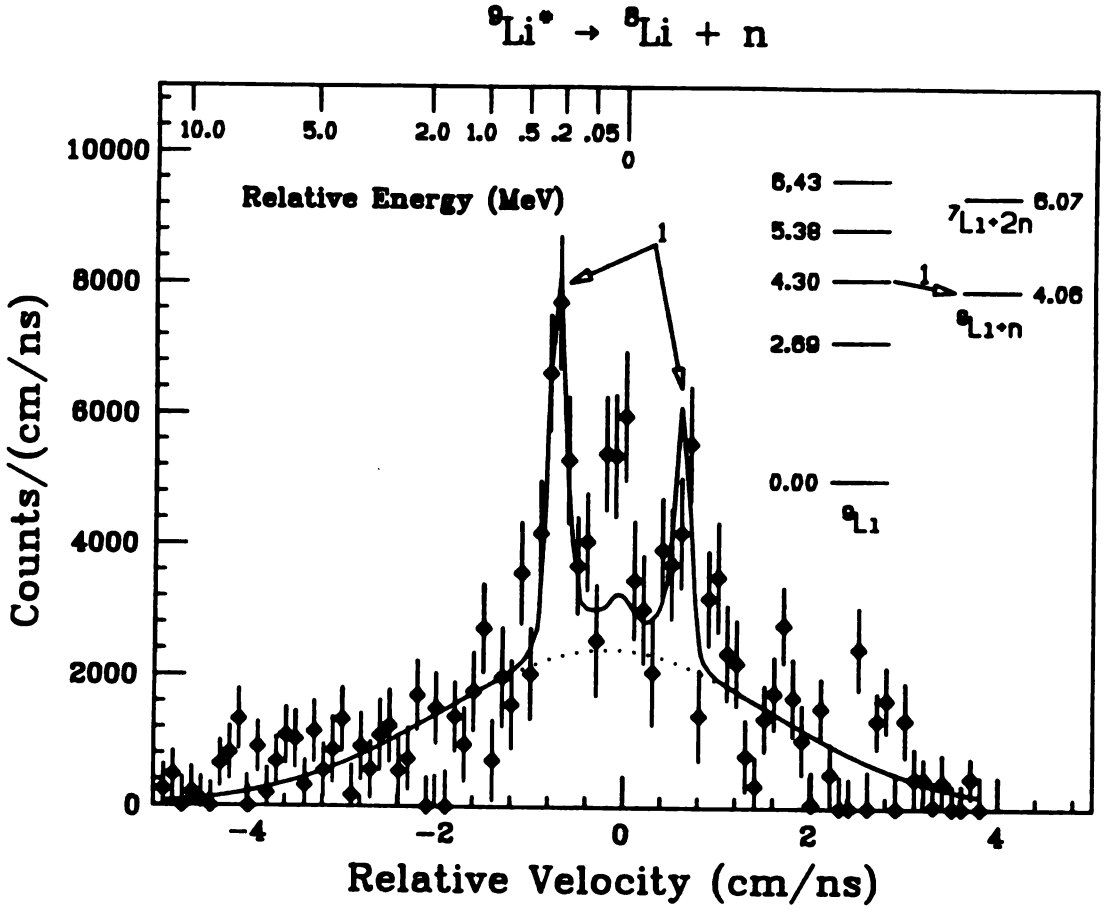

Figure IV.14 - Relative velocity spectrum for ^{8}Li + n at 15°. The resonance comes from the decay indicated in the energy level diagram. A relative energy scale is included for reference. The line shows a fit to the data that is explained in the text. The dotted line shows the background used.

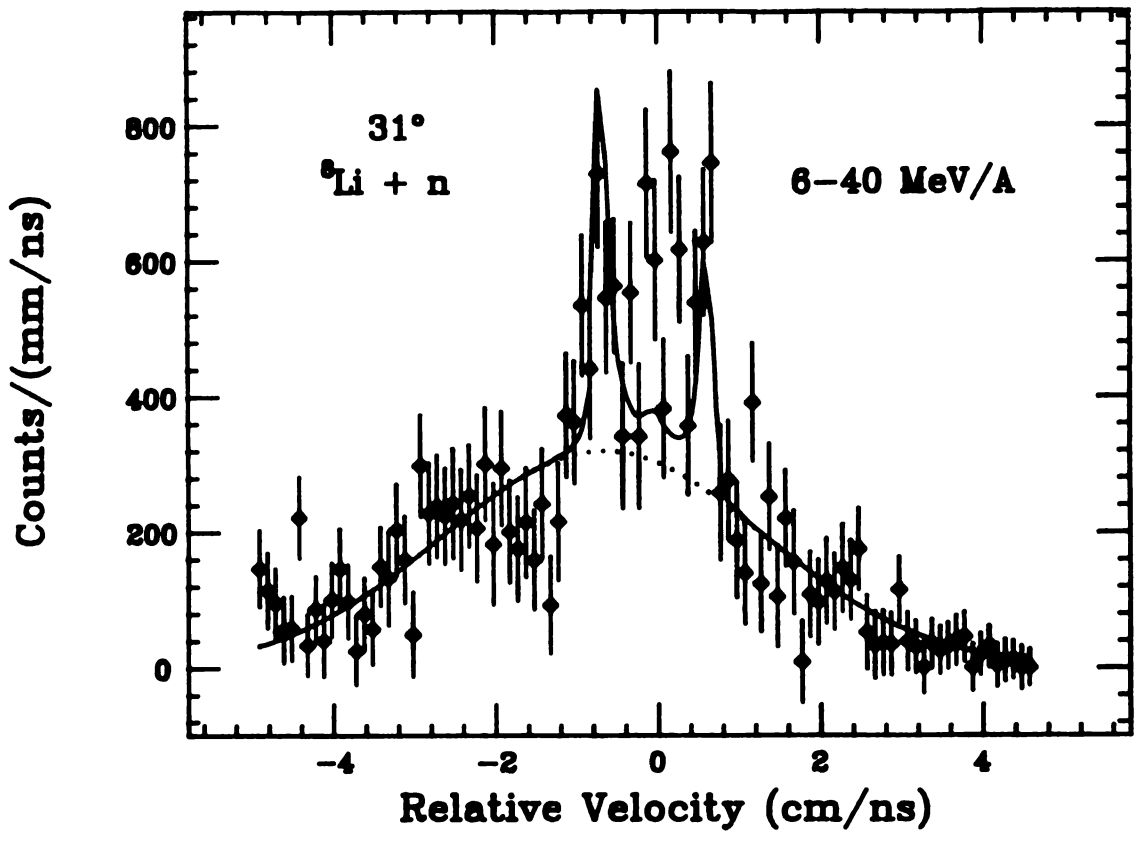

Figure IV.15 - Relative velocity spectrum for ^{8}Li + n at 31° and for ^{8}Li energies above 6 MeV/A.

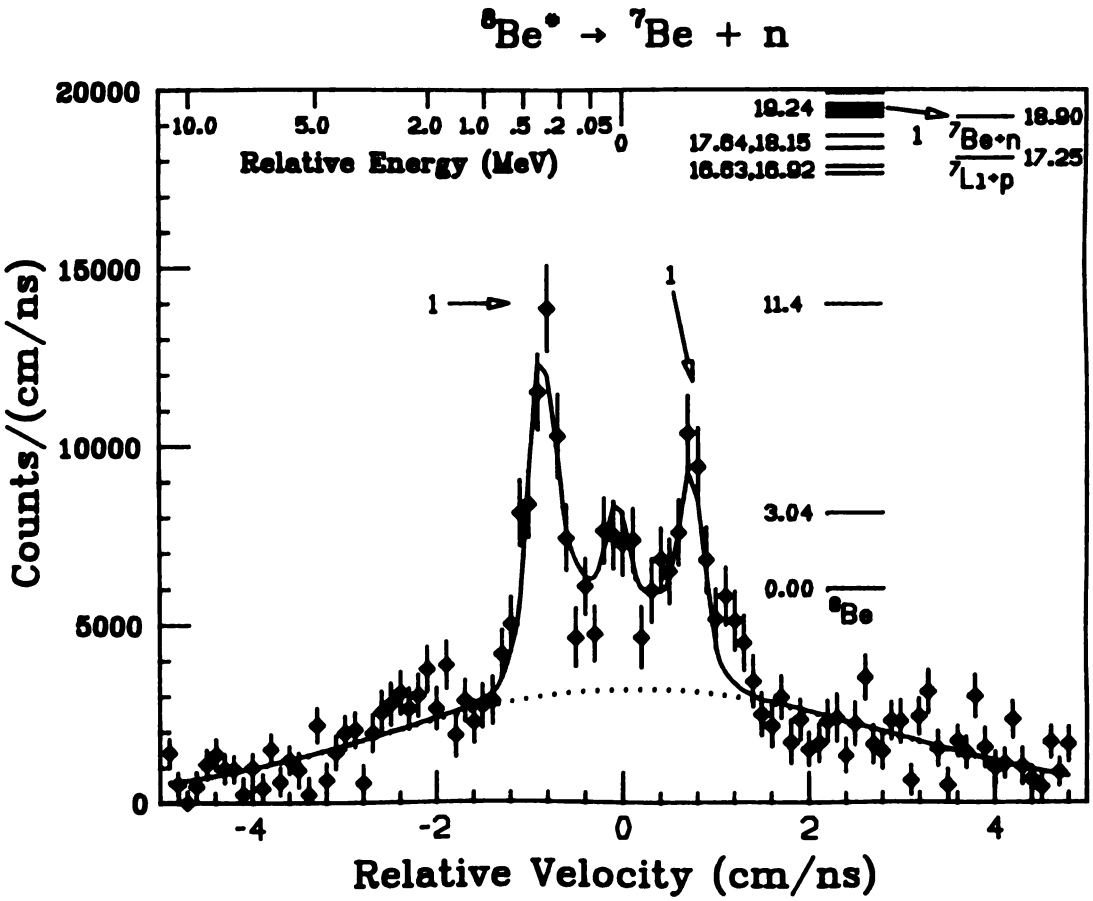

Figure IV.16 - Relative velocity spectrum for ^{7}Be + n at 15°. The resonance comes from the decay indicated in the energy level diagram. A relative energy scale is included for reference. The line shows a fit to the data that is explained in the text. The dotted line shows the background used.

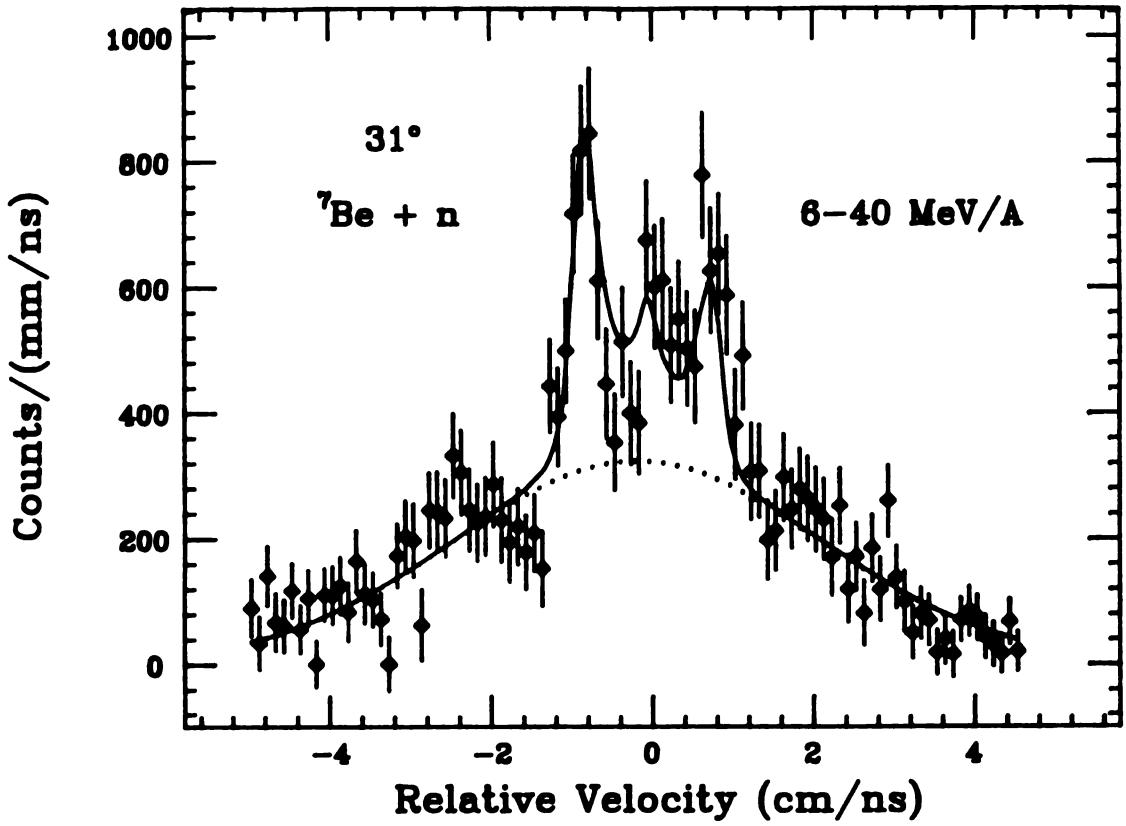

Figure IV.17 - Relative velocity spectrum for ^{7}Be + n at 31° and for ^{7}Be energies above 6 MeV/A.

5. ^{9}Be + n

Figure IV.18 shows the relative velocity spectrum for ^{9}Be + n at 15° for ^{9}Be kinetic energies between 6 and 40 MeV/nucleon. Two sets of peaks are observed in this spectrum. One set, at ±1.0 cm/ns, is due to the decays of the 7.371-MeV ($J^{\pi}= 3^{-}$, Γ = 15.7 keV) and 7.542-MeV ($J^{\pi}= 2^{+}$, Γ = 6.3 keV) states of ^{10}Be to the ground state of ^{9}Be. Because of the experimental resolution (~2 mm/ns), these two states cannot be separated. The second set, at ± 2.3 cm/ns, is due to the decays of the overlapping 9.27-MeV ($J^{\pi}= 4^{-}$, Γ = 150 keV) and 9.4-MeV ($J^{\pi}= 2^{+}$, Γ = 291 keV) states of ^{10} Be to the ground state of ^{9}Be. Using the data from McLa88, it is estimated that the decay to the ground state from these two states accounts for 93 ± 8 % of the total width. With widths of 150 and 291 keV and a separation of only 130 keV, these two states are not resolvable. Figure IV.19 shows the ^{9}Be + n relative velocity spectra at 31° and 64° for ^{9}Be kinetic energies between 6 and 40 MeV/nucleon. The decay of the 7.37-MeV + 7.54-MeV states can be seen at all three angles, and the decay of the 9.27-MeV + 9.4-MeV states can be seen at 15° and 31°. Figure IV.20 contains ^{9}Be + n relative velocity spectra at 15° for cuts on ^{9}Be kinetic energy of 6-10 MeV/nucleon, 6-15 MeV/nucleon, and 15-40 MeV/nucleon. Figure IV.21 shows ^{9}Be + n relative velocity spectra at 31° for energy cuts of 6-15 MeV/nucleon and 15-40 MeV/nucleon.

Table IV.8 contains the populations of the 7.37-MeV + 7.54-MeV group of states and the 9.27-MeV + 9.4-MeV group of states extracted from the fits to the spectra shown in Figures IV.18-21. Because of a lack of statistics, no populations are reported for the 9.27-MeV + 9.4-MeV group of states for kinetic energies below 15 MeV/nucleon.

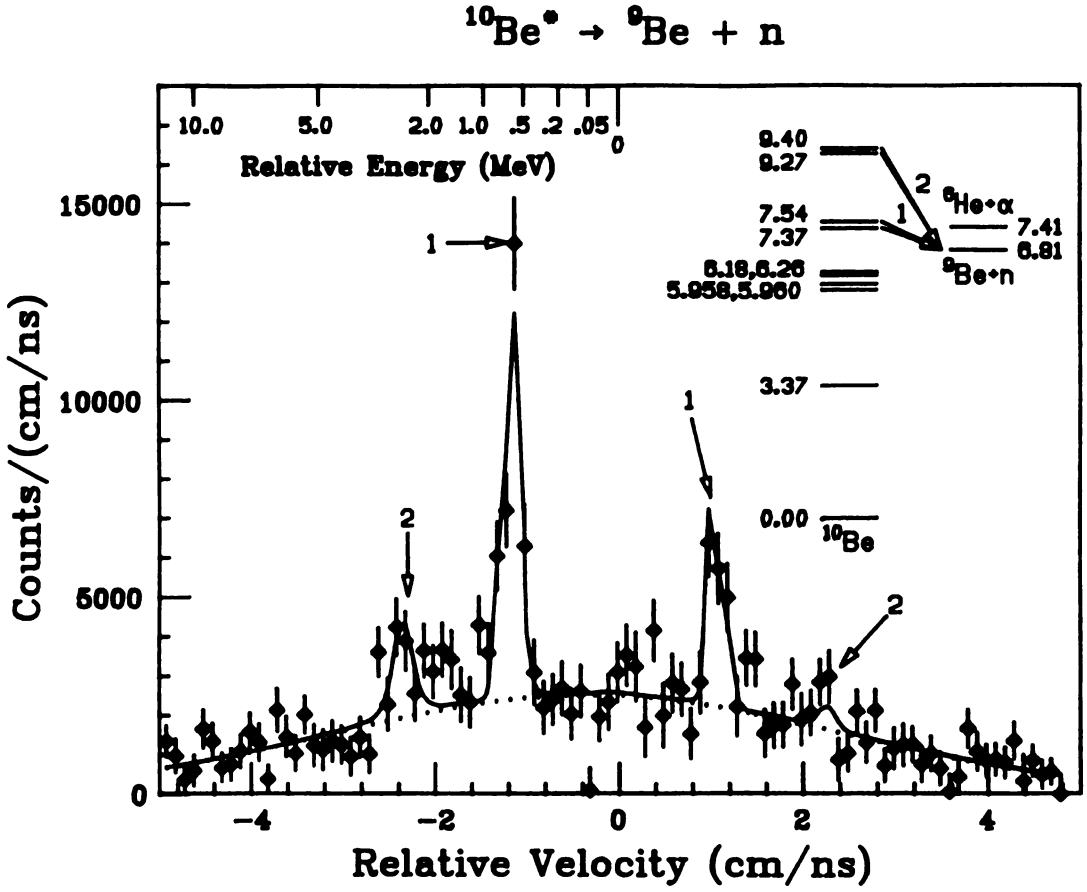

Figure IV.18 - Relative velocity spectrum for ^{9}Be + n at 15° and for ^{9}Be kinetic energies above 6 MeV/A. The resonances come from the decays indicated in the energy level diagram. A relative energy scale is included for reference. The line shows a fit to the data using a background that is shown with the dotted line. The fit is explained in the text.

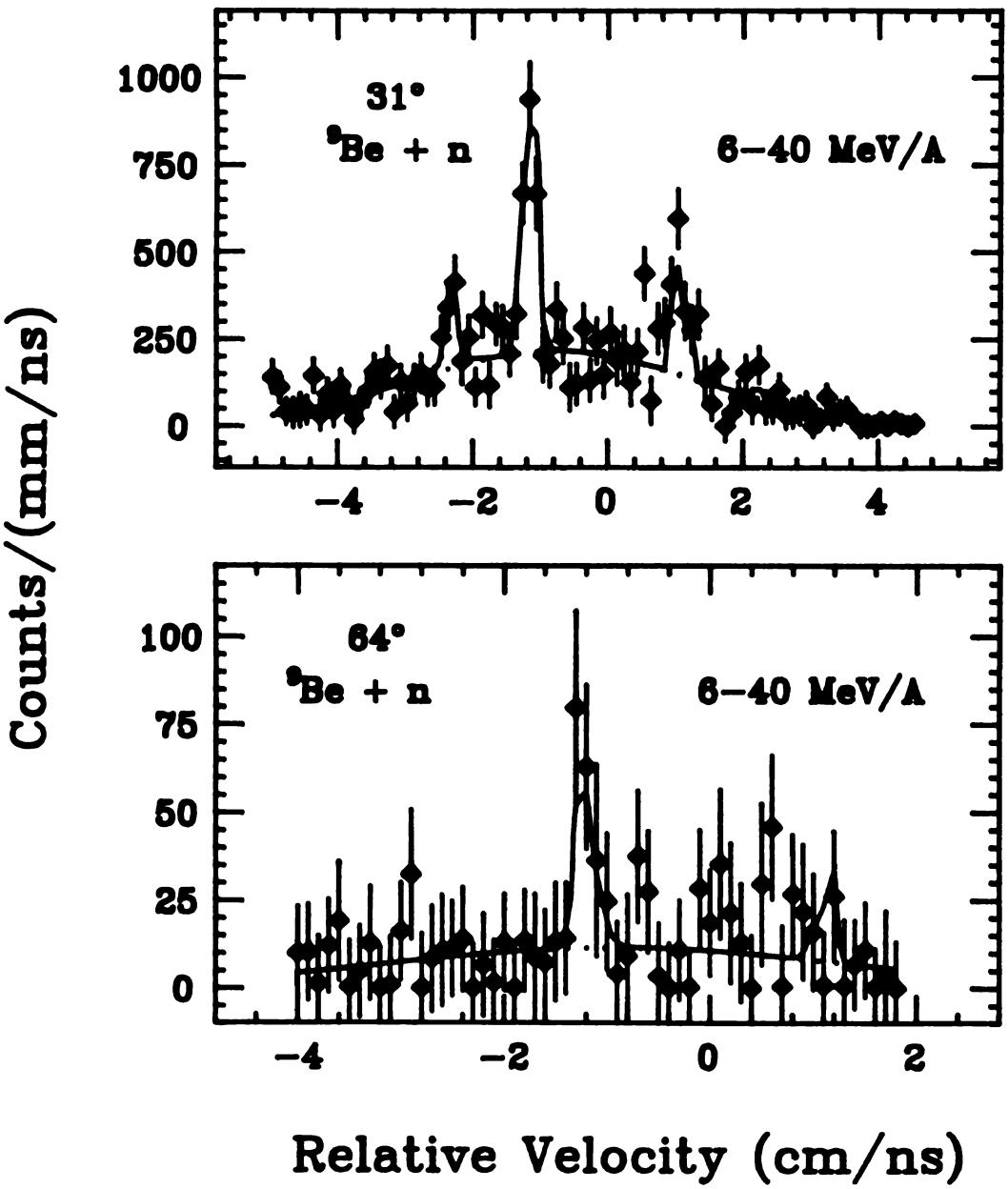

Figure IV.19 - Relative velocity spectra for ^{9}Be + n at 31° and 64° and for all ^{9}Be kinetic energies above 6 MeV/A.

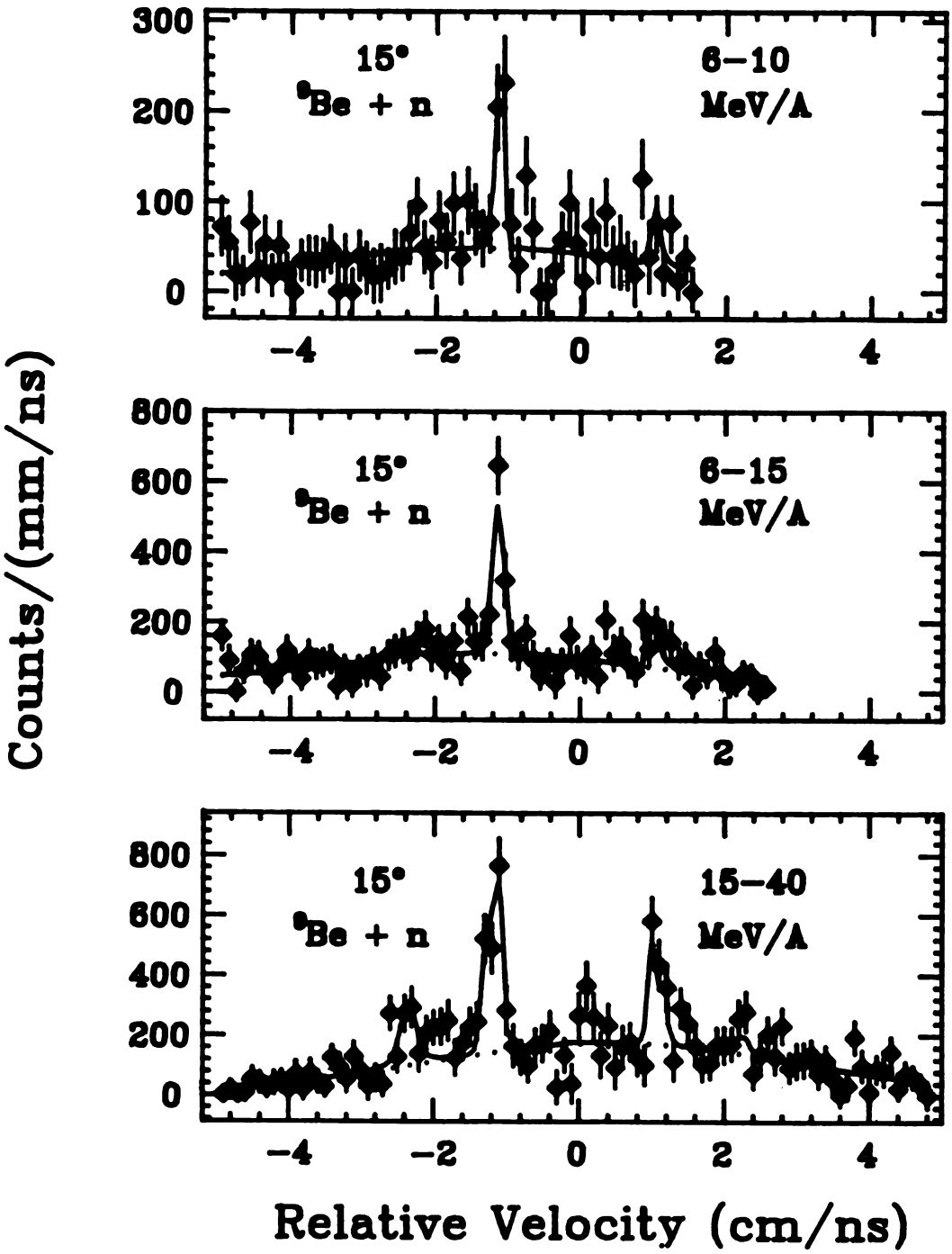

Figure IV.20 - Relative velocity spectra for ^{9}Be + n at 15° and for the indicated cuts on ^{9}Be kinetic energy.

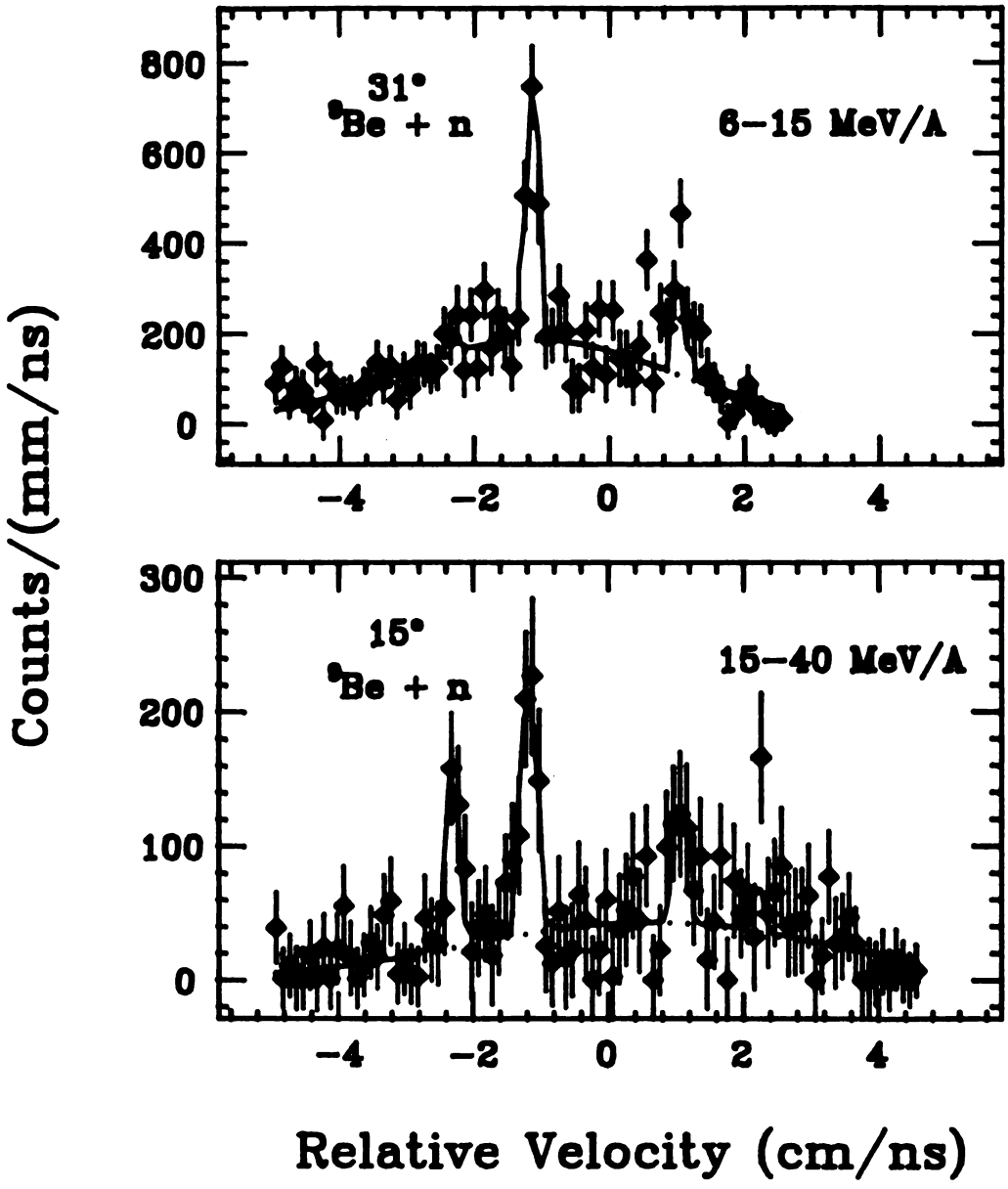

Figure IV.21 - Relative velocity spectra for ^{9}Be + n at 31° and ^{9}Be kinetic energies from 6-15 MeV/A, and for ^{9}Be + n at 15° and ^{9}Be kinetic energies from 15-40 MeV/A.

Table IV.8 - Populations of the 7.37-MeV + 7.54-MeV group of states and the 9.27-MeV + 9.4-MeV group of states in ^{10}Be for the indicated cuts on ^{9}Be kinetic energy and for the indicated angles. The units are in mb/sr, and the uncertainty in the last significant digit(s) is written in the parenthesis following each value of the population.

^{10}Be(7.37-MeV + 7.54-MeV) Population

Energy Range	15°	31°	64°
6-40 MeV/A			0.014(4)
6-15 MeV/A	1.08(17)	0.33(4)	
15-40 MeV/A	1.16(12)	0.10(7)	
6-10 MeV/A	0.55(12)		

^{10}Be(9.27-MeV + 9.40-MeV) Population

Energy Range	15°	31°
6-15 MeV/A	0.43(53)	0.10(7)
15-40 MeV/A	1.59(42)	0.16(3)

6. ^{10}Be + n

The decay of the 3.89-MeV ($J \geq 7/2$, $\Gamma \leq 10$ keV) state in ^{11}Be to the first excited state of ^{10}Be (3.368-MeV, $J^{\pi} = 2^{+}$) gives the central peak observed in ^{10}Be + n relative velocity spectra. Figure IV.22 shows the relative velocity spectrum for ^{10}Be + n at 31°, along with an energy-level diagram showing the observed decays in that spectrum. The decay of the 3.96-MeV ($J^{\pi} = 3/2^{-}$, $\Gamma = 15$ keV) state of ^{11}Be to the first excited state of ^{10}Be is also seen. Figure IV.23 shows the relative velocity spectra for ^{10}Be + n at 15° and 64° for ^{10}Be kinetic energies between 6 and 40 MeV/nucleon. Statistics were good enough to determine the population of both states for cuts on kinetic energy of 6-10 MeV/nucleon, 10-14 MeV/nucleon, 14-18 MeV/nucleon, 18-22 MeV/nucleon, 22-26 MeV/nucleon, 26-30 MeV/nucleon, and 30-40 MeV/nucleon at 15°, and for cuts of 6-10 MeV/nucleon, 10-14 MeV/nucleon, and 14-40 MeV/nucleon at 31°. Figure IV.24 shows relative velocity spectra for ^{10}Be + n at 15° for the indicated energy cuts, and Figure IV.25 shows ^{10}Be + n spectra at 31° for the indicated cuts on energy. The populations of both states extracted from the fits to the spectra shown in Figures IV.24 and IV.25 are shown in Table IV.9.

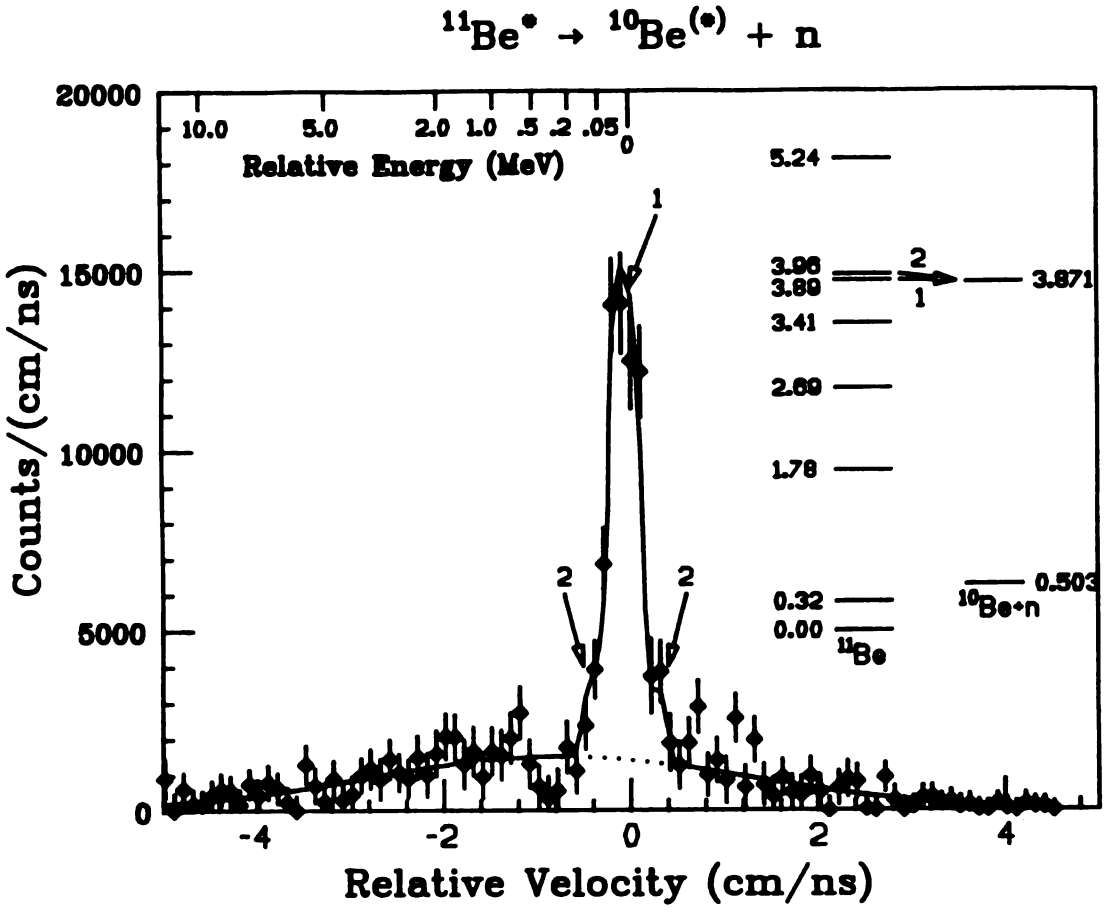

Figure IV.22 - Relative velocity spectrum for ^{10}Be + n at 31° and for ^{10}Be kinetic energies above 6 MeV/A. The resonances come from the decays indicated in the energy level diagram. A relative energy scale is included for reference. The line shows a fit to the data using a background that is shown with the dotted line. The fit is explained in the text.

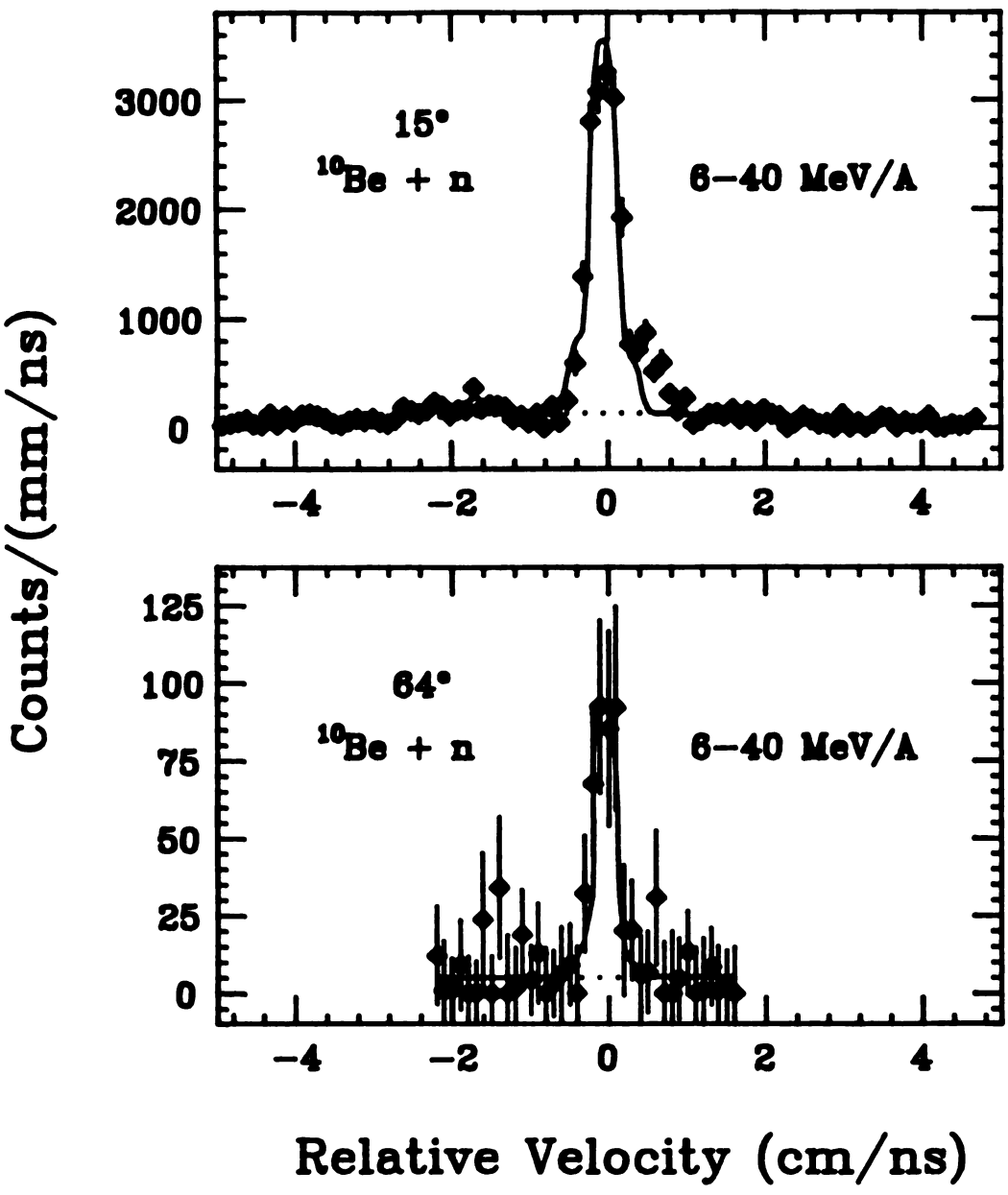

Figure IV.23 - Relative velocity spectra for ^{10}Be + n at 15° and 64° and for all ^{10}Be kinetic energies above 6 MeV/A.

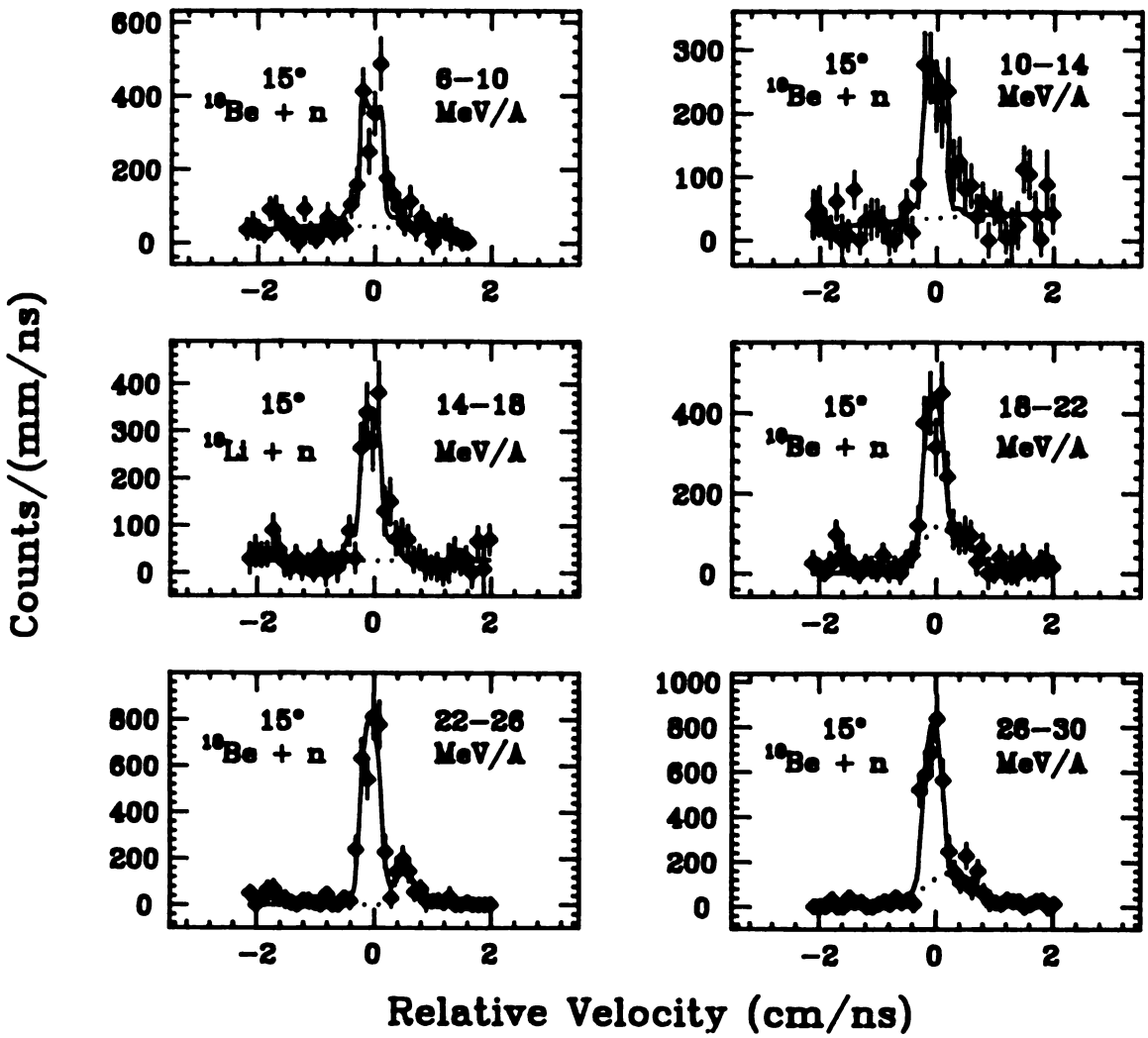

Figure IV.24 - Relative velocity spectra for ^{10}Be + n at 15° and for the indicated cuts on ^{10}Be kinetic energy.

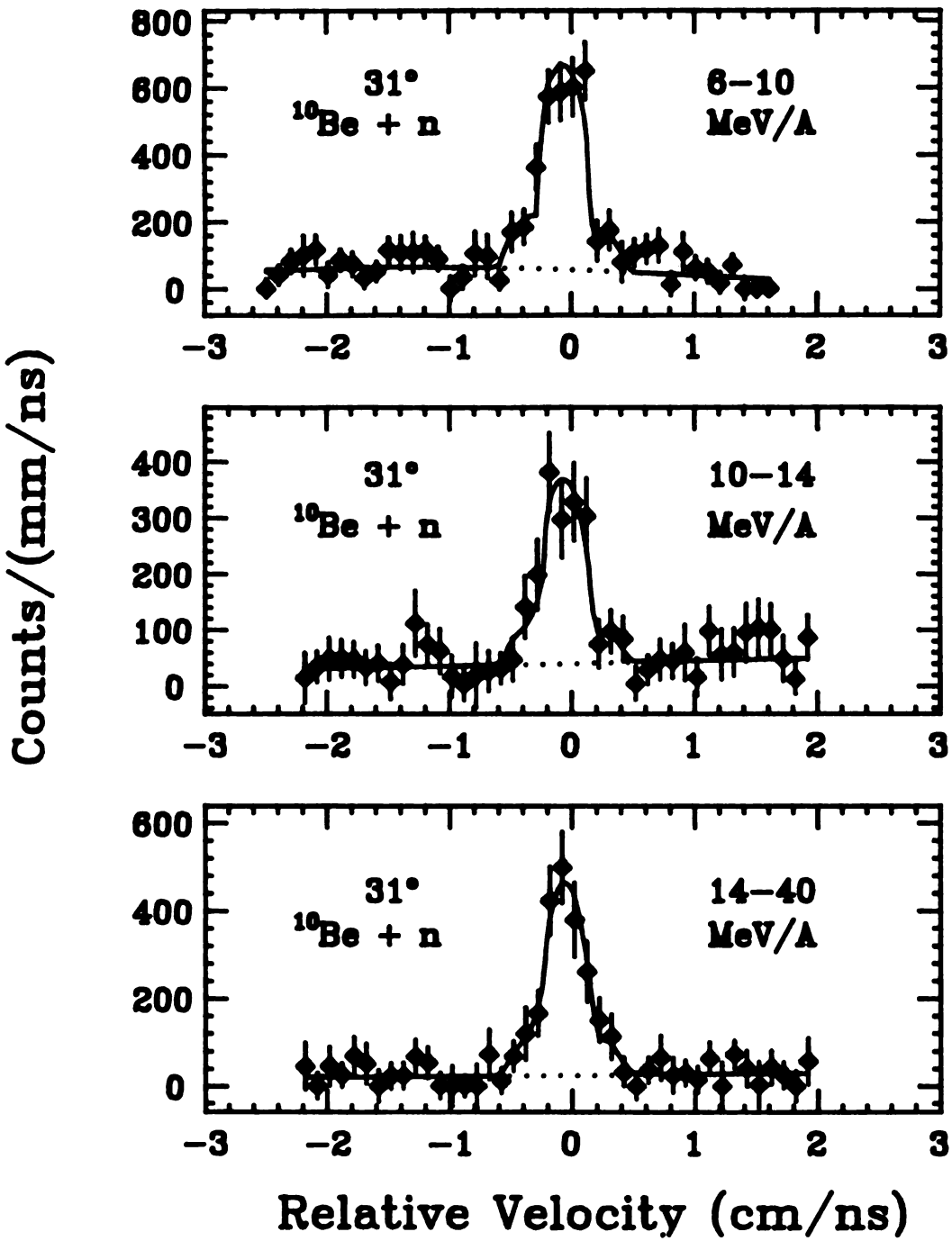

Figure IV.25 - Relative velocity spectra for ^{10}Be + n at 31° and for the indicated cuts on ^{10}Be kinetic energy.

Table IV.9 - Populations of the 3.89-MeV state and the 3.96-MeV state in ^{11}Be for the indicated cuts on ^{10}Be kinetic energy and for the indicated angles. The units are in mb/sr, and the uncertainty in the last significant digit(s) is written in the parenthesis following each value of the population.

^{11}Be(3.89-MeV) Population (mb/sr)

15°		31°	
Energy Range	Population	Energy Range	Population
6-10 MeV/A	0.037(3)	6-10 MeV/A	0.0148(12)
10-14 MeV/A	0.019(2)	10-14 MeV/A	0.0065(8)
14-18 MeV/A	0.021(2)	14-40 MeV/A	0.0071(8)
18-22 MeV/A	0.023(4)		
22-26 MeV/A	0.044(3)		
26-30 MeV/A	0.039(4)		
30-40 MeV/A	0.020(2)		

^{11}Be(3.96-MeV) Population (mb/sr)

15°		31°	
Energy Range	Population	Energy Range	Population
6-10 MeV/A	0.025(15)	6-10 MeV/A	0.016(4)
10-14 MeV/A	0.078(76)	10-14 MeV/A	0.005(2)
14-40 MeV/A	0.105(76)	14-40 MeV/A	0.0057(17)

7. $^{11}B + n$

Two unbound-state populations can be determined from relative velocity spectra for $^{11}B + n$. Looking at Figure III.7, which is for $^{11}B + n$ at 31° and for 6 MeV/nucleon $\leq E_{^{11}B} \leq$ 40 MeV/nucleon, it is noted that the large, central peak is due to the decay of the 3.388-MeV ($J^{\pi}=3^{-}$, Γ = 3.1 keV) state in ^{12}B to the ground state of ^{11}B. Because of the large collection efficiency for that decay, it is possible to obtain good statistical accuray for the state population even when the fragment kinetic energy gate is small. Figure IV.26 shows relative velocity spectra for $^{11}B + n$ at 15° for 2-MeV/nucleon wide cuts on ^{11}B kinetic energy. The energy cuts are indicated in each plot. Figure IV.27 shows relative velocity spectra for $^{11}B + n$ at 31° for the indicated cuts on kinetic energy. Figures IV.28 and IV.29 show relative velocity spectra for cuts of 6-15 MeV/nucleon and 15-40 MeV/nucleon on kinetic energy at 15° and 31°, respectively. Figure IV.30 shows the relative velocity spectrum for kinetic energies between 6 and 40 MeV/nucleon at 64°. As can be seen in Figures III.7, IV.28, and IV.29, the decay of the 3.759-MeV state ($J^{\pi}= 2^{+}$, Γ = 40 keV) of ^{12}B to the ground state of ^{11}B is also detected for the corresponding cuts on kinetic energy. The populations of the 3.388-MeV and 3.759-MeV states extracted from the fits to the spectra shown in Figures IV.26-29 are listed in Table IV.10 in units of mb/sr. The population of the 3.388-MeV state in ^{12}B for ^{11}B kinetic energies between 6 and 40 MeV/nucleon at 64° is 0.0074 ± 0.0007 mb/sr.

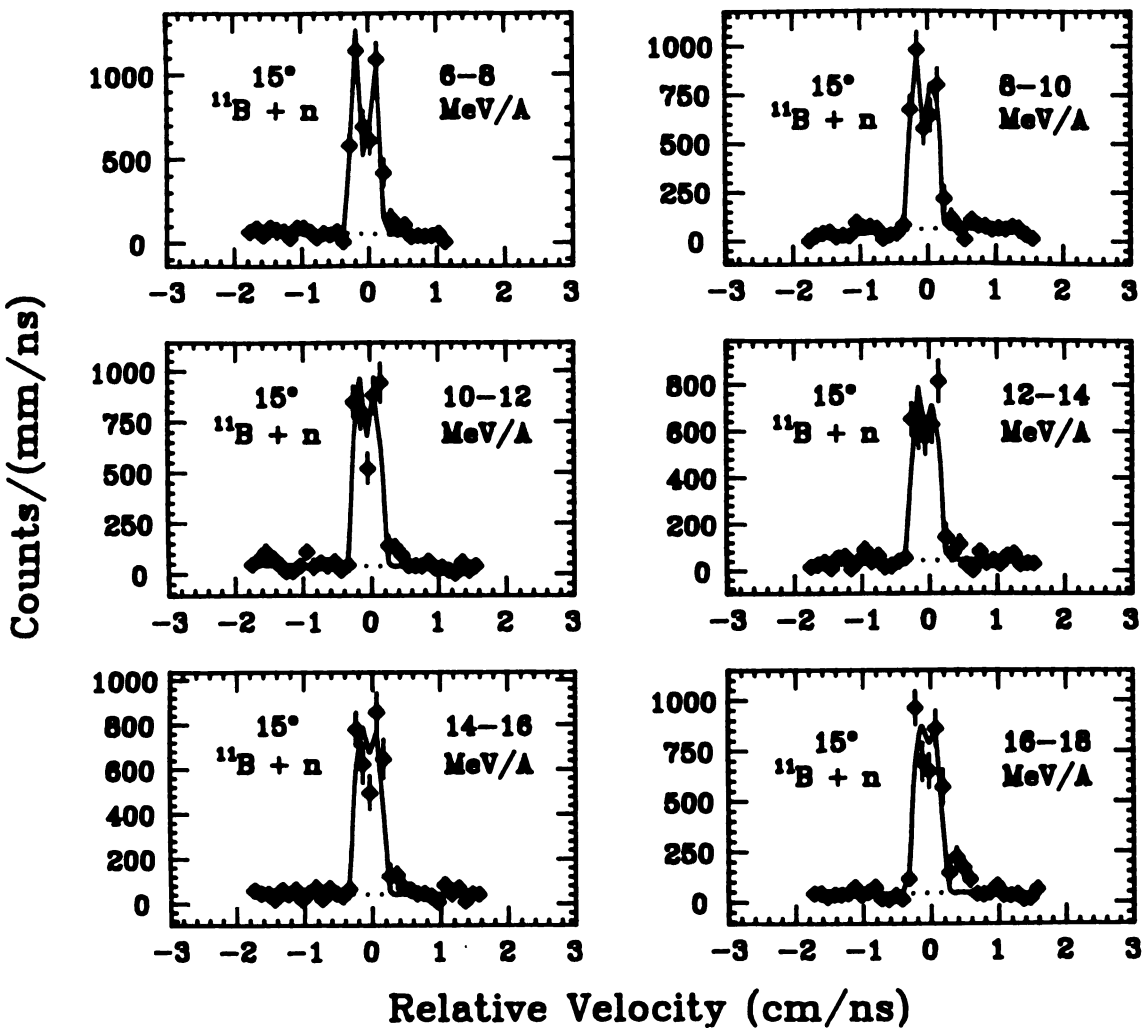

Figure IV.26 - Relative velocity spectra for ^{11}B + n at 15° and for the indicated cuts on ^{11}B kinetic energy.

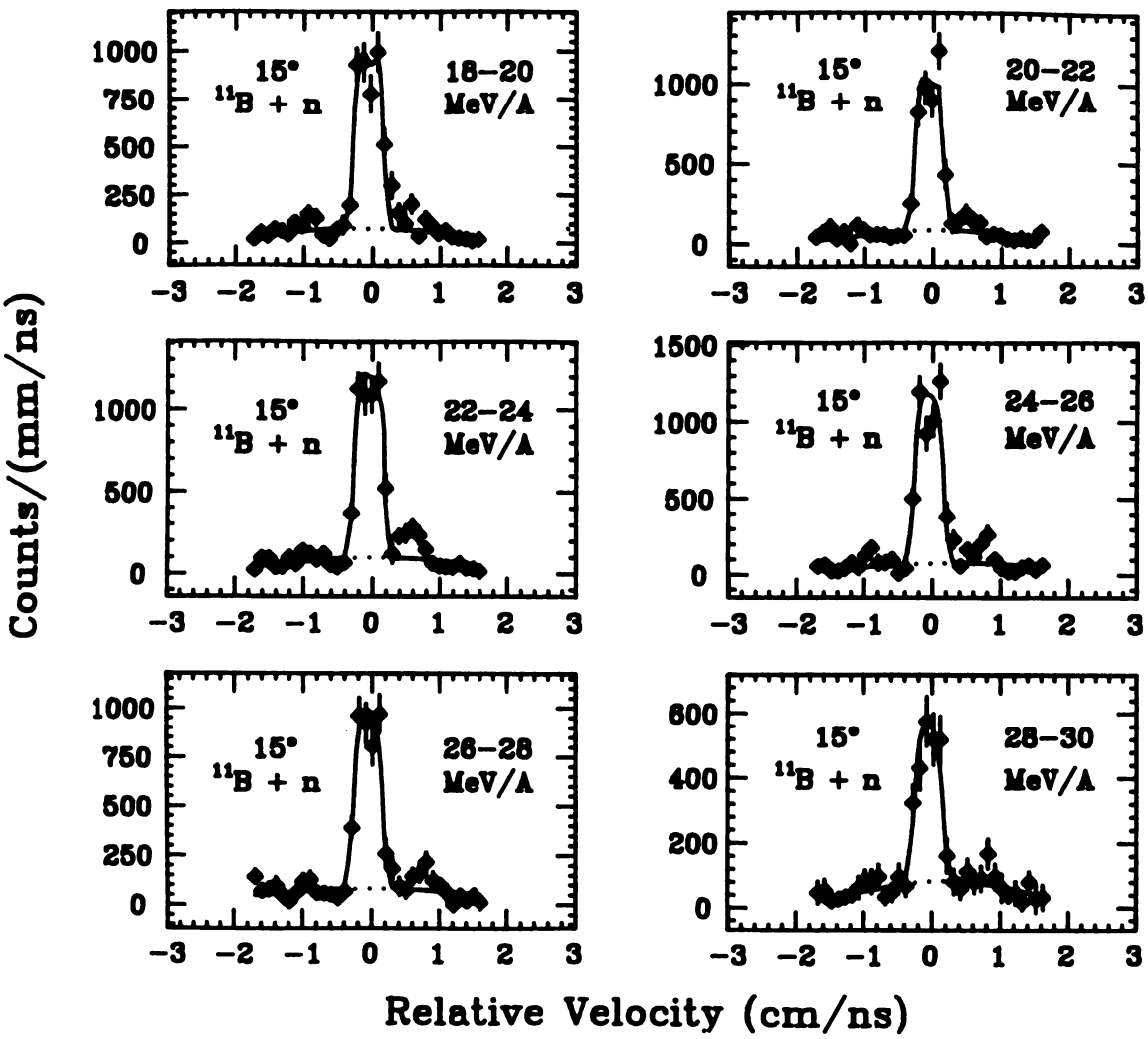

Figure IV.26 - (cont'd.).

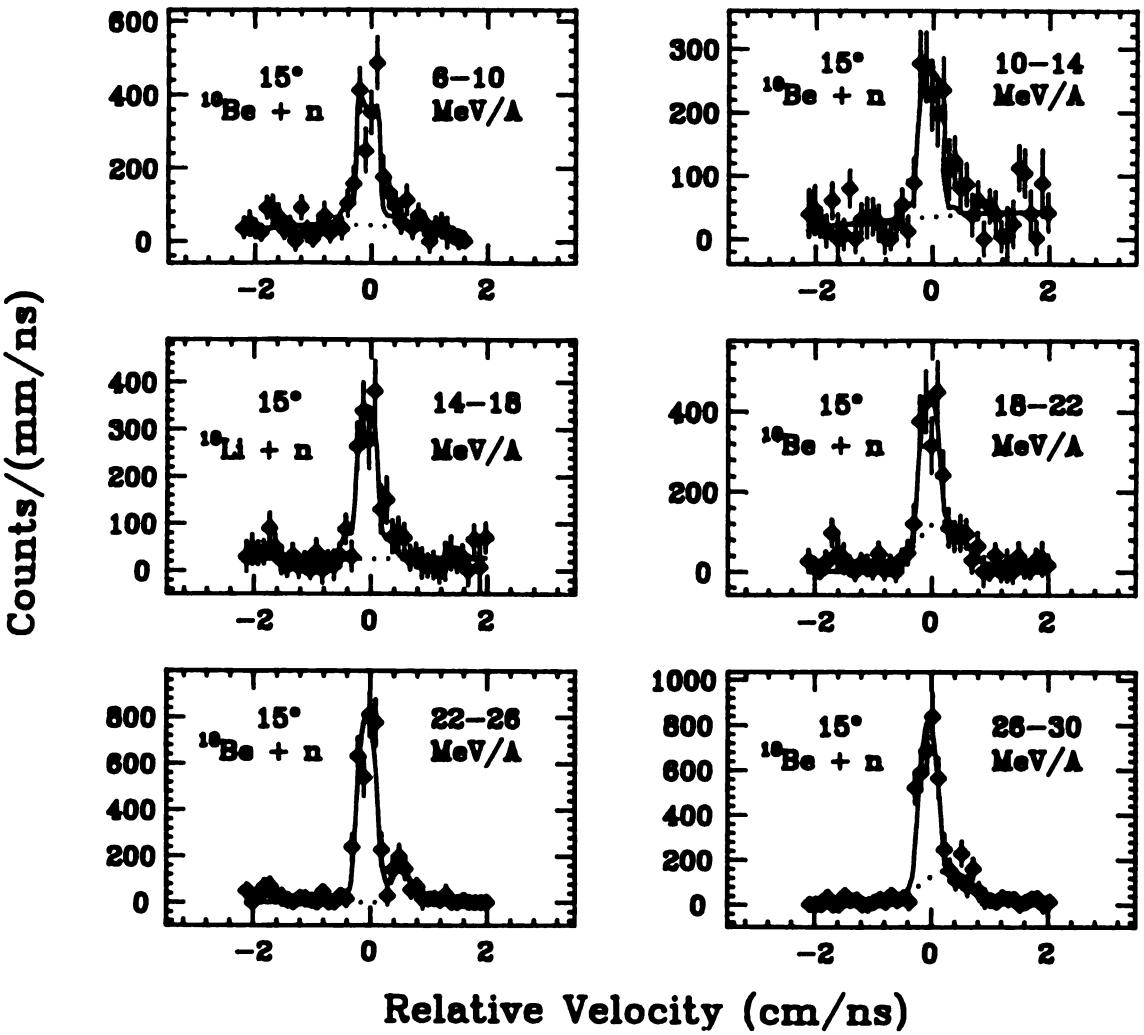

Figure IV.24 - Relative velocity spectra for ^{18}Be + n at 15° and for the indicated cuts on ^{18}Be kinetic energy.

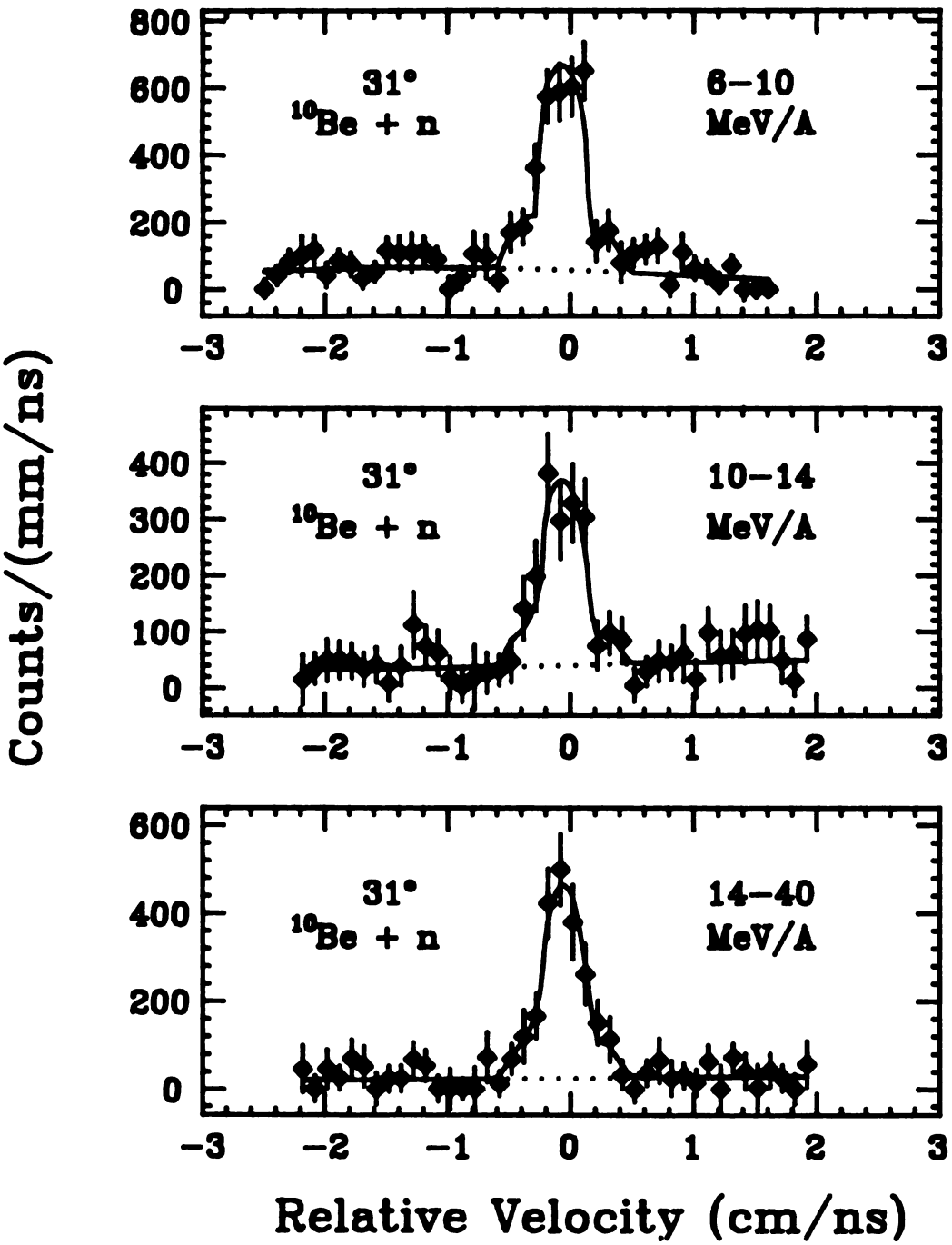

Figure IV.25 - Relative velocity spectra for ^{10}Be + n at 31° and for the indicated cuts on ^{10}Be kinetic energy.

Table IV.9 - Populations of the 3.89-MeV state and the 3.96-MeV state in ^{11}Be for the indicated cuts on ^{10}Be kinetic energy and for the indicated angles. The units are in mb/sr, and the uncertainty in the last significant digit(s) is written in the parenthesis following each value of the population.

^{11}Be(3.89-MeV) Population (mb/sr)

15°		31°	
Energy Range	Population	Energy Range	Population
6-10 MeV/A	0.037(3)	6-10 MeV/A	0.0148(12)
10-14 MeV/A	0.019(2)	10-14 MeV/A	0.0065(8)
14-18 MeV/A	0.021(2)	14-40 MeV/A	0.0071(8)
18-22 MeV/A	0.023(4)		
22-26 MeV/A	0.044(3)		
26-30 MeV/A	0.039(4)		
30-40 MeV/A	0.020(2)		

^{11}Be(3.96-MeV) Population (mb/sr)

15°		31°	
Energy Range	Population	Energy Range	Population
6-10 MeV/A	0.025(15)	6-10 MeV/A	0.016(4)
10-14 MeV/A	0.078(76)	10-14 MeV/A	0.005(2)
14-40 MeV/A	0.105(76)	14-40 MeV/A	0.0057(17)

7. $^{11}B + n$

Two unbound-state populations can be determined from relative velocity spectra for $^{11}B + n$. Looking at Figure III.7, which is for $^{11}B + n$ at 31° and for 6 MeV/nucleon $\leq E_{^{11}B} \leq$ 40 MeV/nucleon, it is noted that the large, central peak is due to the decay of the 3.388-MeV ($J^{\pi}=3^{-}$, Γ = 3.1 keV) state in ^{12}B to the ground state of ^{11}B. Because of the large collection efficiency for that decay, it is possible to obtain good statistical accuray for the state population even when the fragment kinetic energy gate is small. Figure IV.26 shows relative velocity spectra for $^{11}B + n$ at 15° for 2-MeV/nucleon wide cuts on ^{11}B kinetic energy. The energy cuts are indicated in each plot. Figure IV.27 shows relative velocity spectra for $^{11}B + n$ at 31° for the indicated cuts on kinetic energy. Figures IV.28 and IV.29 show relative velocity spectra for cuts of 6-15 MeV/nucleon and 15-40 MeV/nucleon on kinetic energy at 15° and 31°, respectively. Figure IV.30 shows the relative velocity spectrum for kinetic energies between 6 and 40 MeV/nucleon at 64°. As can be seen in Figures III.7, IV.28, and IV.29, the decay of the 3.759-MeV state ($J^{\pi}= 2^{+}$, Γ = 40 keV) of ^{12}B to the ground state of ^{11}B is also detected for the corresponding cuts on kinetic energy. The populations of the 3.388-MeV and 3.759-MeV states extracted from the fits to the spectra shown in Figures IV.26-29 are listed in Table IV.10 in units of mb/sr. The population of the 3.388-MeV state in ^{12}B for ^{11}B kinetic energies between 6 and 40 MeV/nucleon at 64° is 0.0074 ± 0.0007 mb/sr.

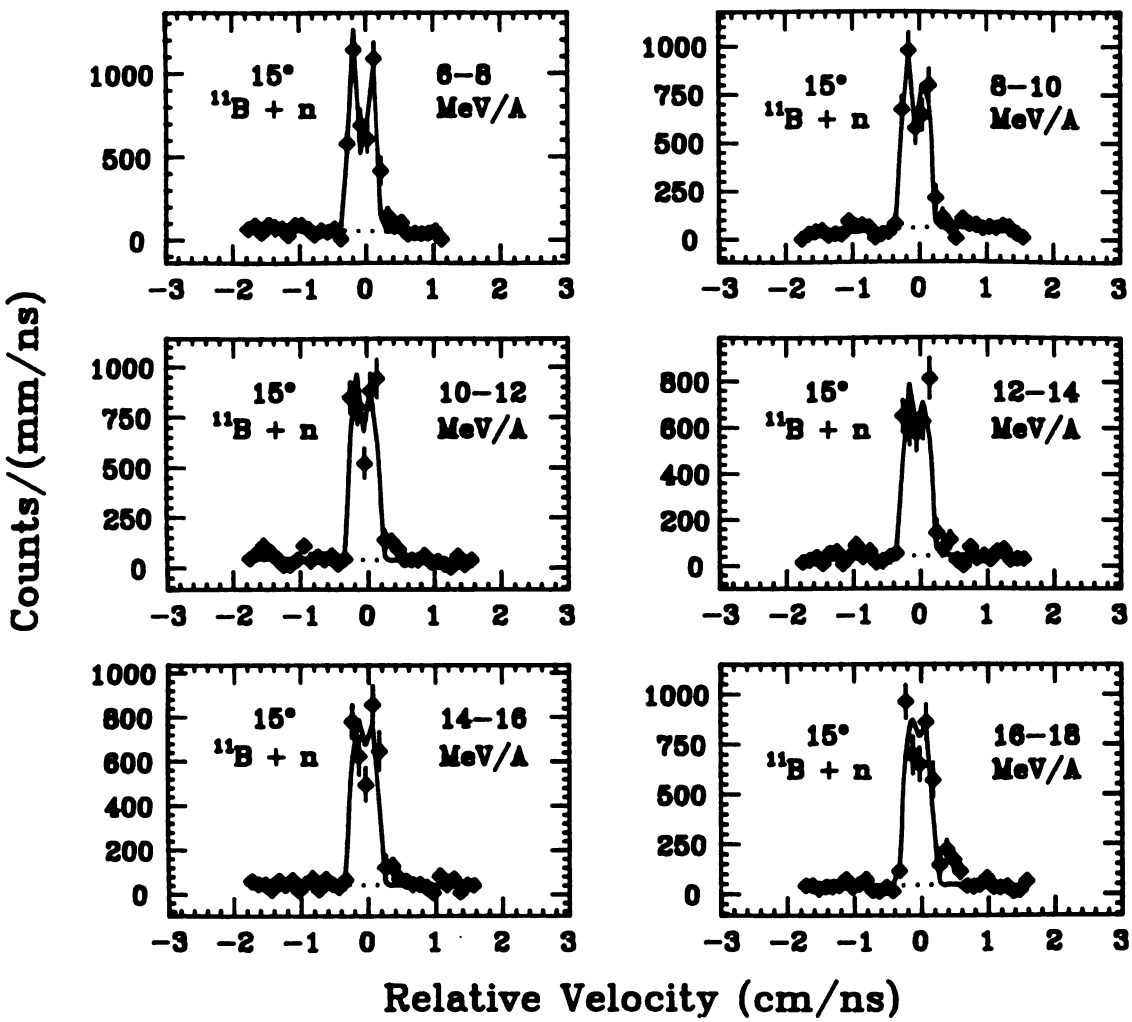

Figure IV.26 - Relative velocity spectra for ^{11}B + n at 15° and for the indicated cuts on ^{11}B kinetic energy.

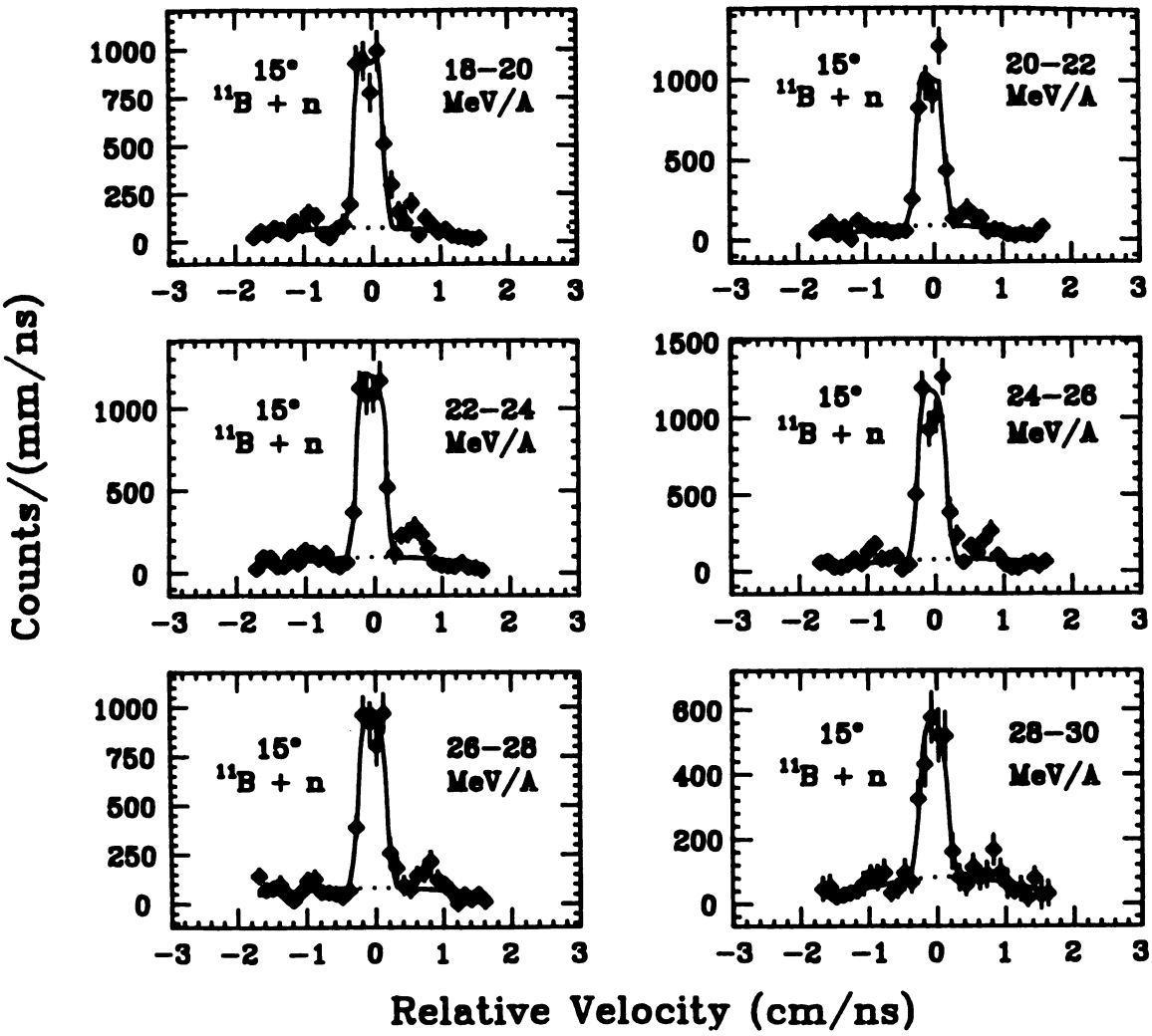

Figure IV.26 - (cont'd.).

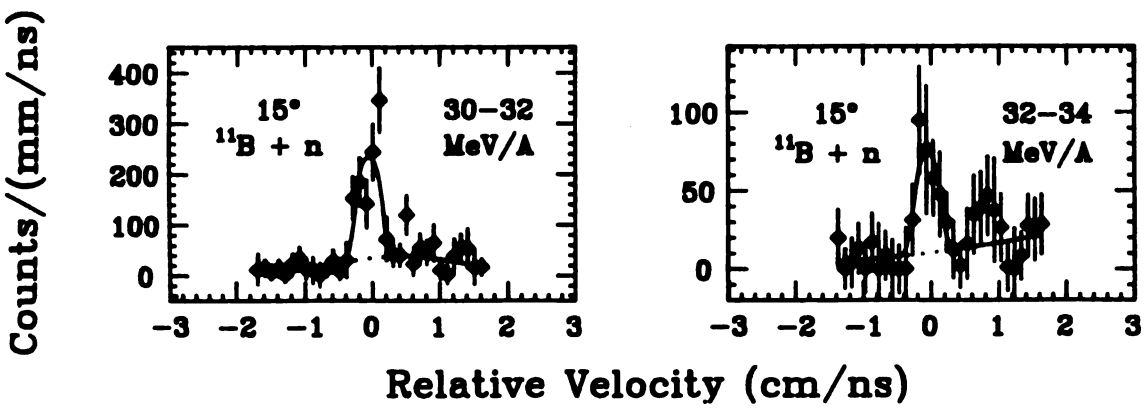

Figure IV.26 - (cont'd.).

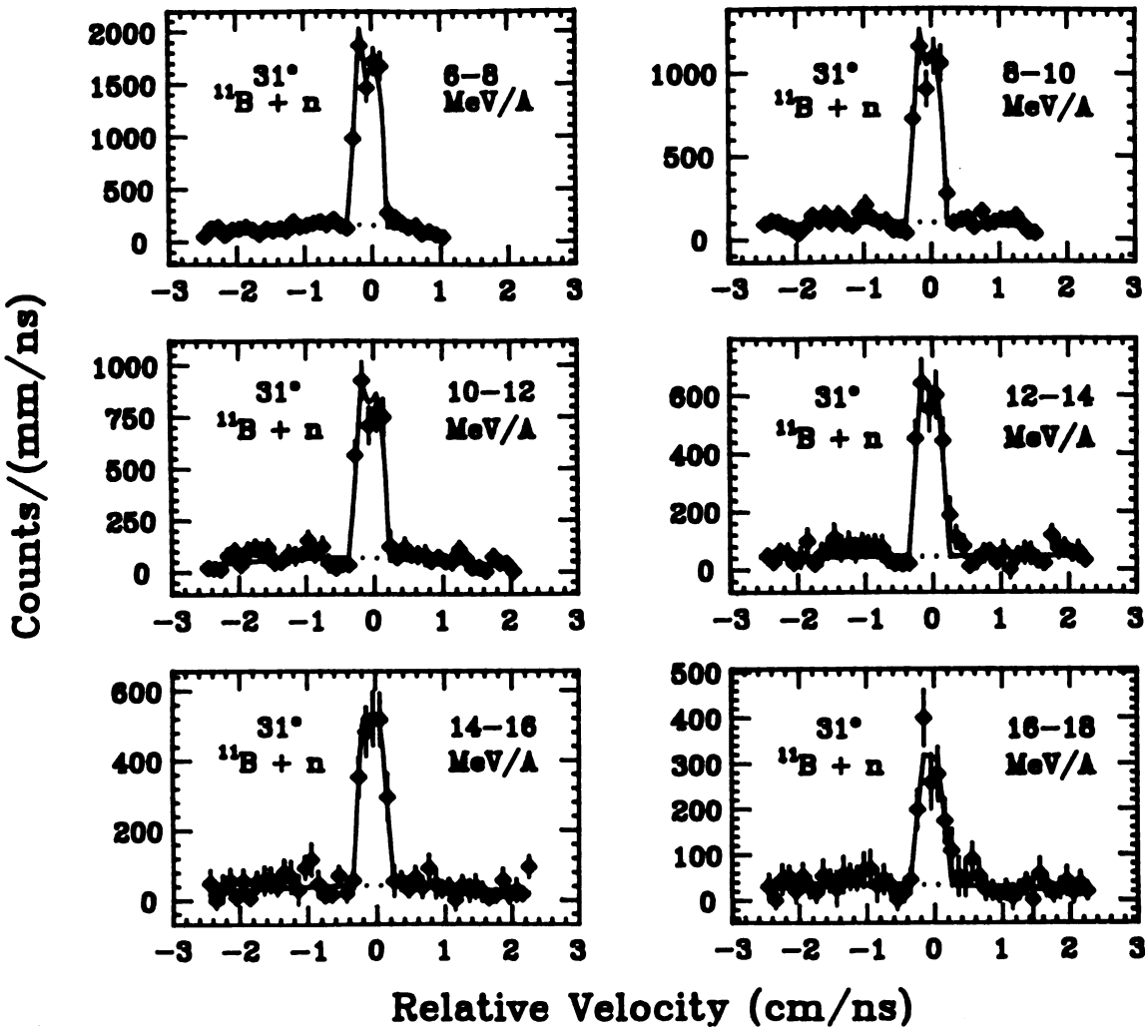

Figure IV.27 - Relative velocity spectra for ^{11}B + n at 31° and for the indicated cuts on ^{11}B kinetic energy.

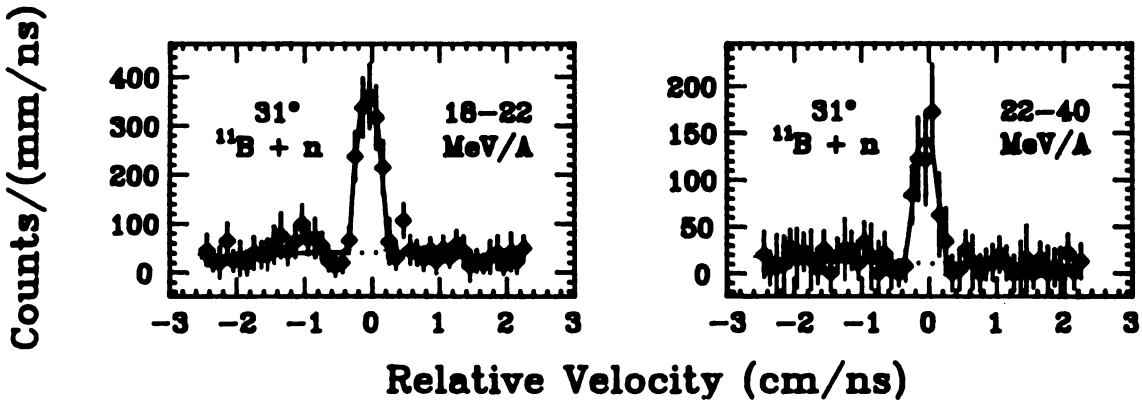

Figure IV.27 - (cont'd.).

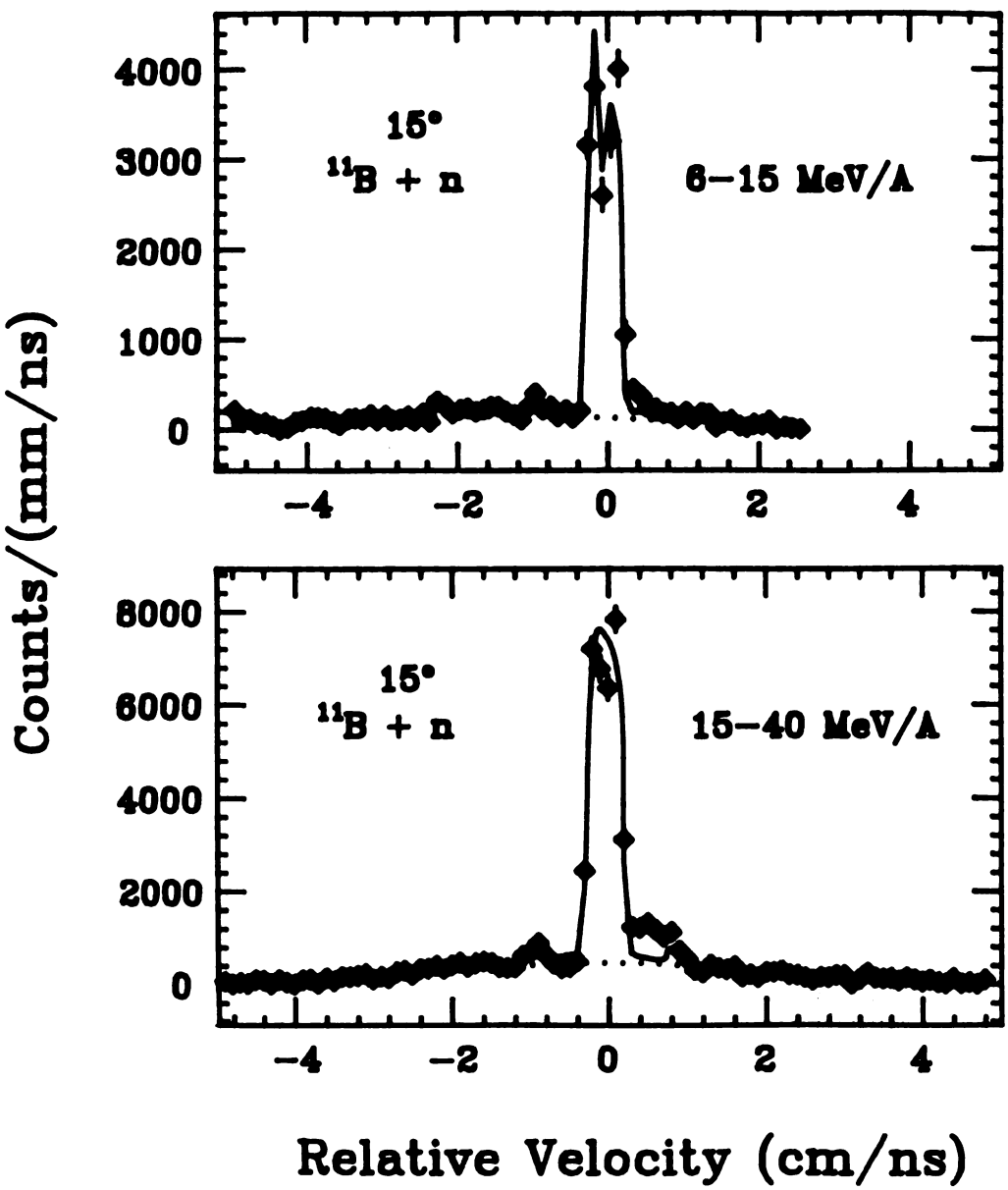

Figure IV.28 - Relative velocity spectra for ^{11}B + n at 15° and for ^{11}B kinetic energies from 6-15 MeV/A and 15-40 MeV/A.

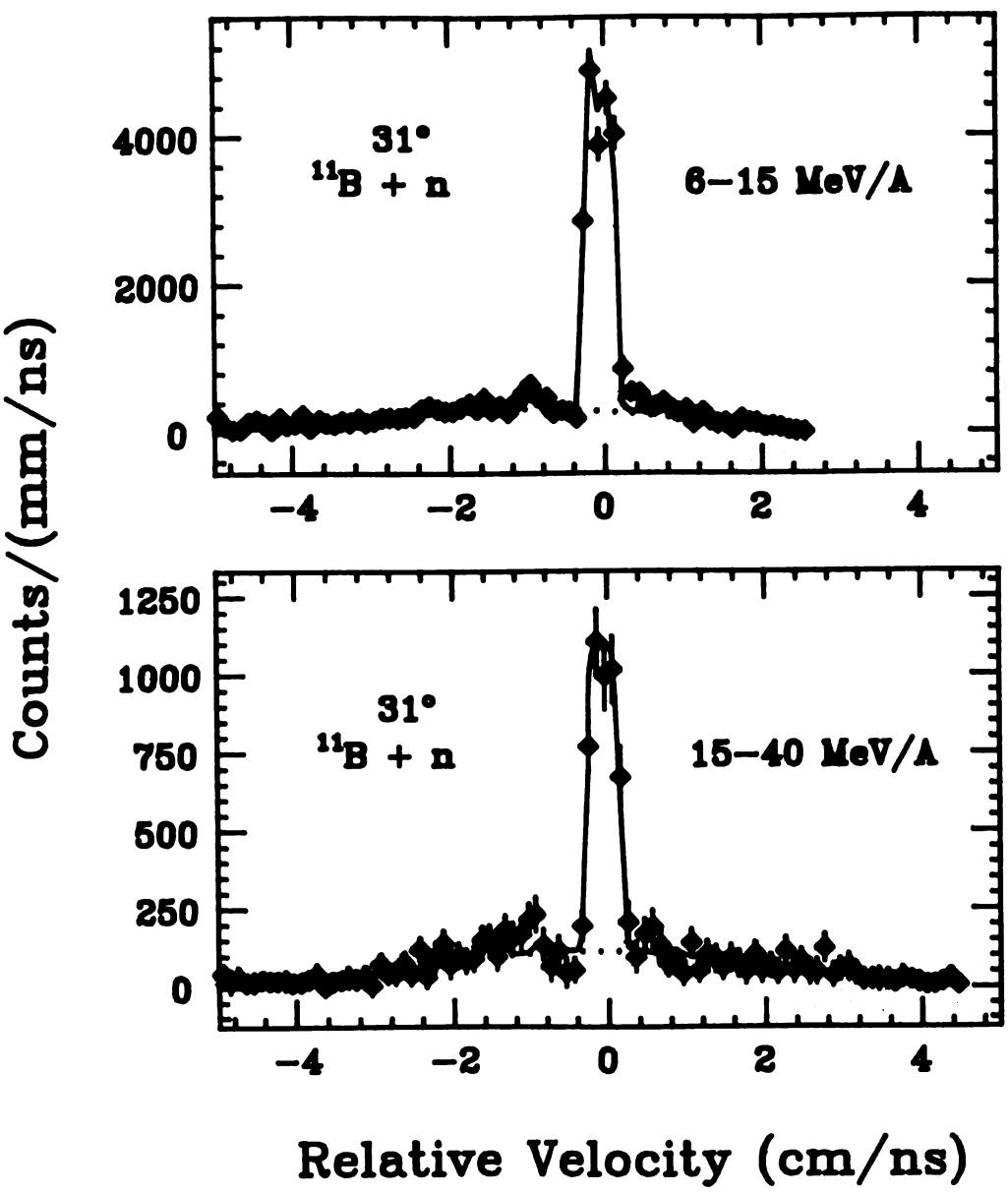

Figure IV.29 - Relative velocity spectra for ^{11}B + n at 31° and for ^{11}B kinetic energies from 6-15 MeV/A and 15-40 MeV/A.

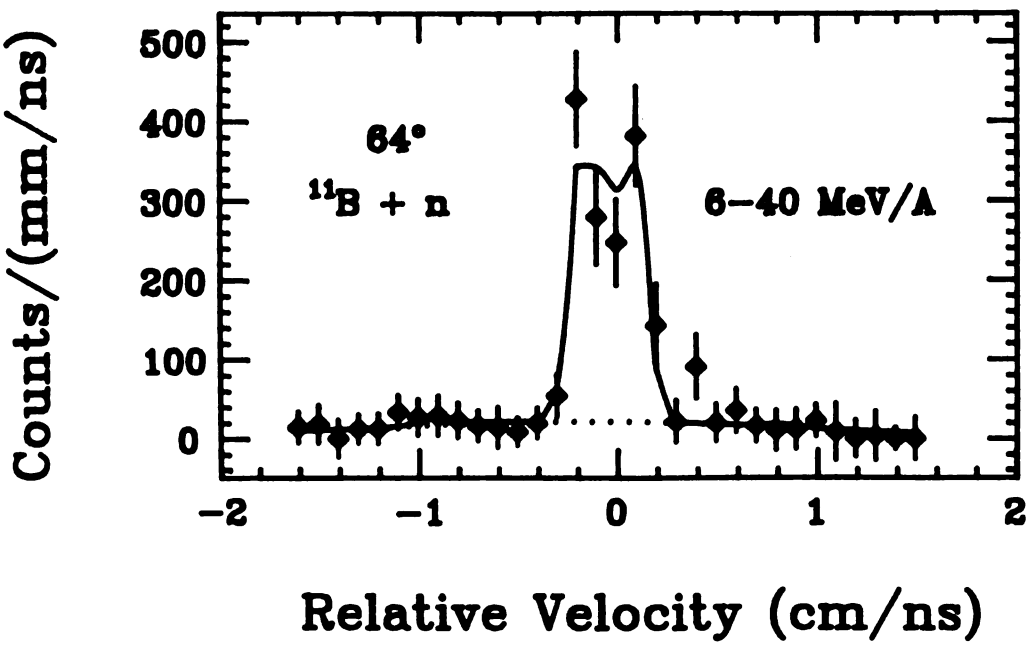

Figure IV.30 - Relative velocity spectrum for ^{11}B + n at 64°.

Table IV.10 - Populations of the 3.388-MeV state and the 3.76-MeV state in ^{12}B for the indicated cuts on ^{11}B kinetic energy and for the indicated angles. The units are in mb/sr, and the uncertainty in the last significant digit(s) is written in the parenthesis following each value of the population.

^{12}B(3.388-MeV) Population (mb/sr)

15°		31°	
Energy Range	Population	Energy Range	Population
6-40 MeV/A	0.856(16)	6-40 MeV/A	0.141(3)
6-15 MeV/A	0.423(11)	6-15 MeV/A	0.122(3)
15-40 MeV/A	0.501(11)	15-40 MeV/A	0.0207(12)
6-8 MeV/A	0.144(7)	6-8 MeV/A	0.052(2)
8-10 MeV/A	0.095(5)	8-10 MeV/A	0.0295(15)
10-12 MeV/A	0.090(5)	10-12 MeV/A	0.0206(13)
12-14 MeV/A	0.065(4)	12-14 MeV/A	0.0144(10)
14-16 MeV/A	0.063(4)	14-16 MeV/A	0.0108(9)
16-18 MeV/A	0.066(4)	16-18 MeV/A	0.0064(7)
18-20 MeV/A	0.072(4)	18-22 MeV/A	0.0067(7)
20-22 MeV/A	0.068(4)	22-40 MeV/A	0.0025(5)
22-24 MeV/A	0.077(4)		
24-26 MeV/A	0.074(4)		
26-28 MeV/A	0.057(3)		
28-30 MeV/A	0.031(3)		
30-32 MeV/A	0.014(2)		
32-34 MeV/A	0.004(1)		

Table IV.10 (cont'd.).

^{12}B(3.76-MeV) Population (mb/sr)

15°		31°	
Energy Range	Population	Energy Range	Population
6-15 MeV/A	0.38(8)	6-15 MeV/A	0.11(2)
15-40 MeV/A	0.59(7)		

8. 12C + n

The decay from three groups of unbound states in ^{13}C can be seen in the relative velocity spectrum for ^{12}C + n at 15° in Figure III.5, which is for ^{12}C kinetic energies between 15 and 40 MeV/nucleon. The set of peaks at ±0.5 cm/ns comes from the decay of the 9.5-MeV ($J^{\pi} = 9/2^{+}$, Γ = 5 keV) state of ^{13}C to the first excited state of ^{12}C (4.44-MeV, $J^{\pi}= 2^{+}$). This decay accounts for approximately 90% of the total decay width (Ohnu86). The set of peaks at ± 2 cm/ns comes from the decay of the 6.868-MeV ($J^{\pi}= 5/2^{+}$, Γ = 6 keV) state of ^{13}C to the ground state of ^{12}C. The set of peaks at ±2.4 cm/ns comes from the decay of three unresolved states in ^{13}C (the 7.492-MeV, $J^{\pi}=7/2^{+}$, $\Gamma \leq 5$ keV state, the 7.547-MeV, $J^{\pi}=5/2^{-}$, Γ = 1.2 keV state, and the 7.686-MeV, $J^{\pi}= 3/2^{+}$, Γ = 70 keV state) that decay to the ground state of ^{12}C. Statistics were good enough to determine the populations of the 9.5-MeV state and the 7.49-MeV + 7.55-MeV + 7.69-MeV group of states at 15° for cuts on kinetic energy of 6-10 MeV/nucleon, 10-15 MeV/nucleon, 15-20 MeV/nucleon, 20-25 MeV/nucleon, 25-30 MeV/nucleon, and 30-40 MeV/nucleon. The spectra for these cuts on energy are shown in Figure IV.31. Figure IV.32 shows the relative velocity spectra for a cut of 6-15 MeV/nucleon at 15° and 31°. Figure IV.33 shows relative velocity spectra at 31° and 64° for kinetic energies between 6 and 40 MeV/nucleon. Table IV.11 lists the populations extracted from the fits to the spectra shown in Figures IV.31-33.

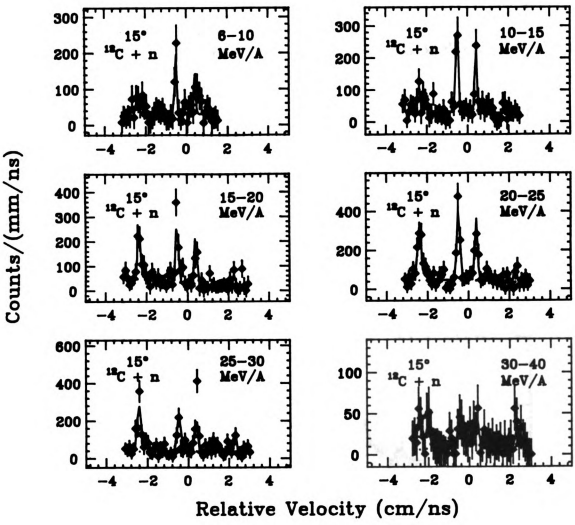

Figure IV.31 - Relative velocity spectra for ^{12}C + n at 15° and for the indicated cuts on ^{12}C kinetic energy.

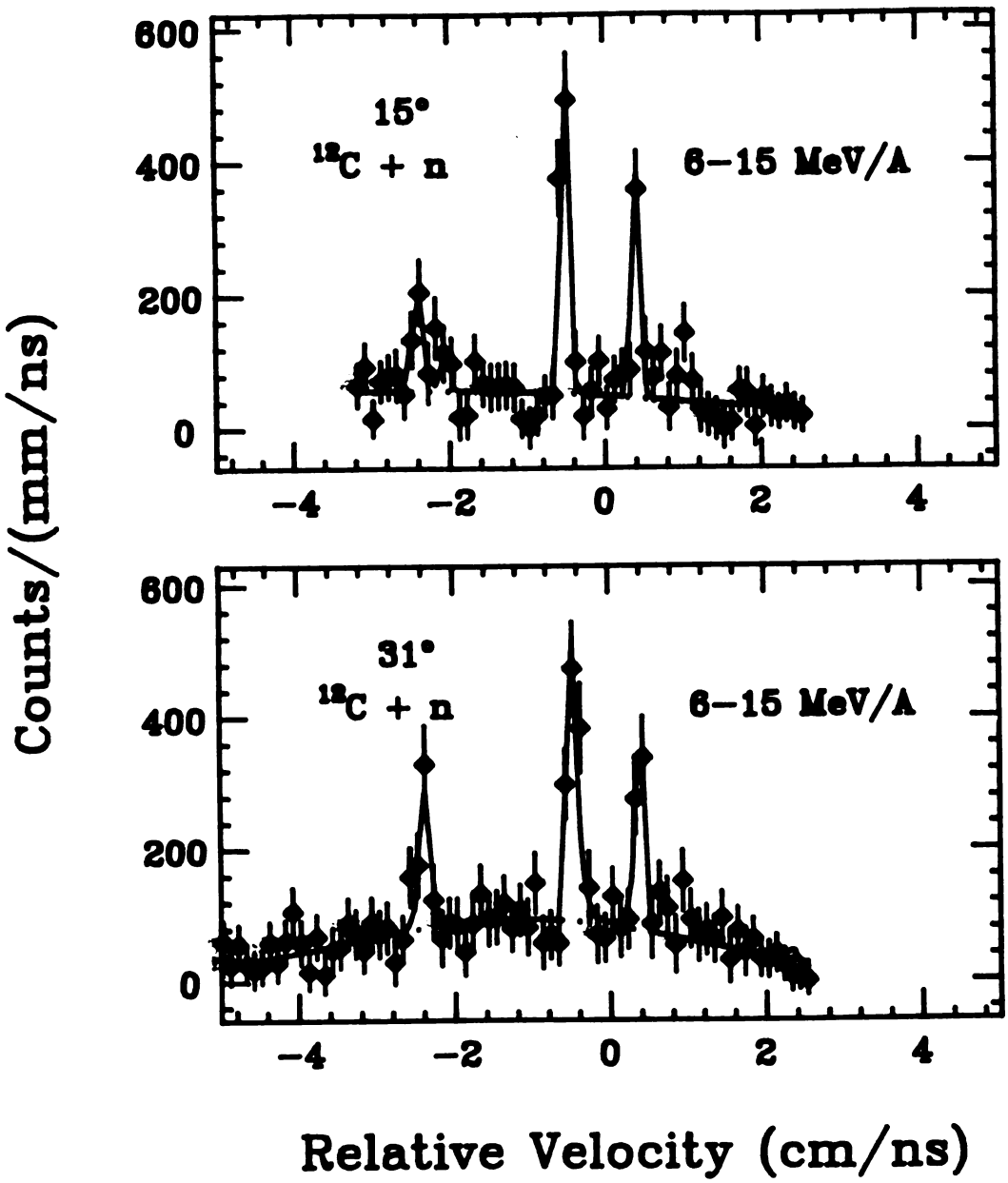

Figure IV.32 - Relative velocity spectra for ^{12}C + n at 15° and 31° for ^{12}C kinetic energies from 6-15 MeV/A.

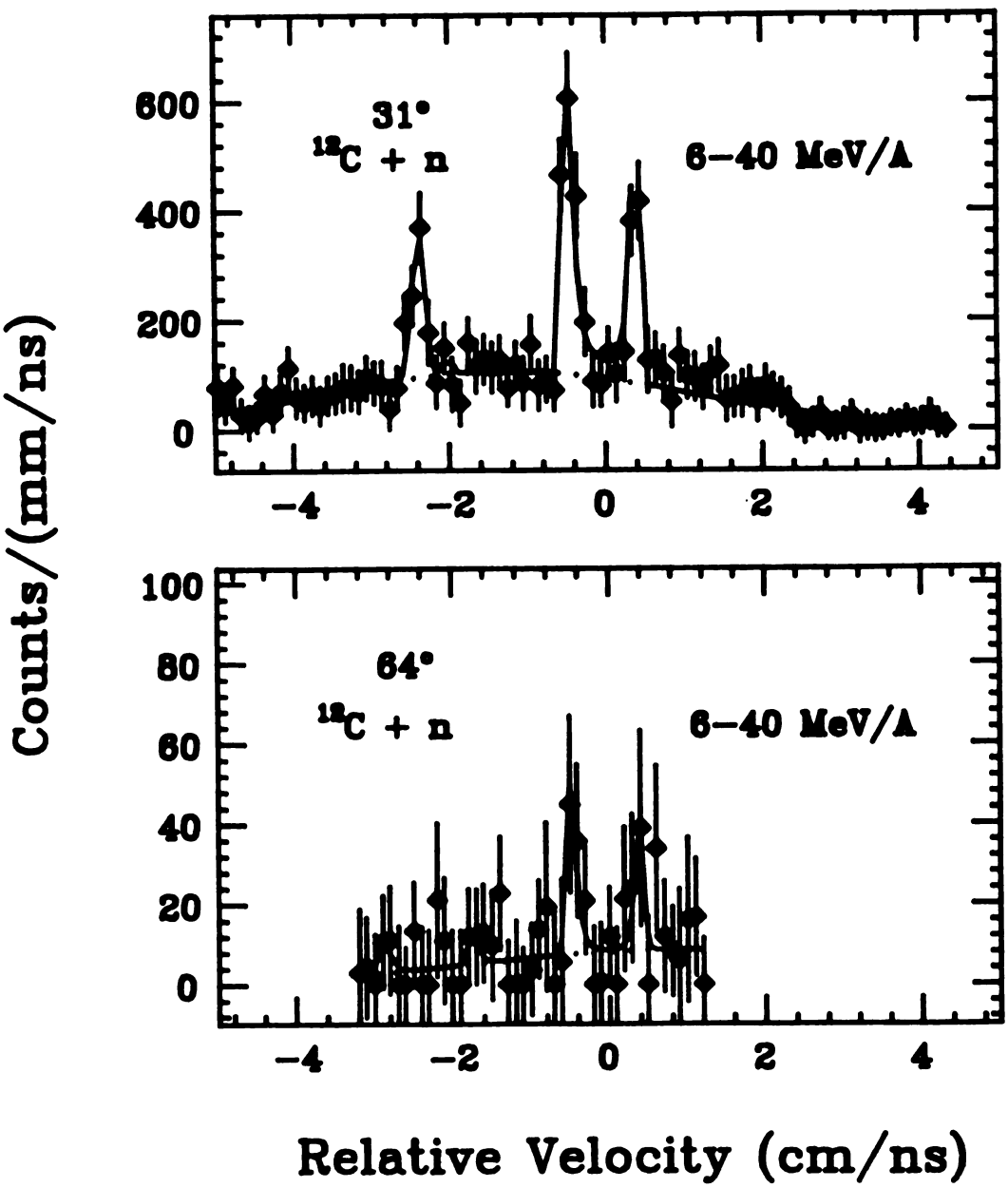

Figure IV.33 - Relative velocity spectra for ^{12}C + n at 31° and 64° for ^{12}C kinetic energies above 6 MeV/A.

Table IV.11 - Populations of the 6.86-MeV state, the 7.49-MeV + 7.55-MeV + 7.69-MeV group of states, and the 9.5-MeV state in ^{13}C for the indicated cuts on ^{12}C kinetic energy and for the indicated angles. The units are in mb/sr, and the uncertainty in the last significant digit(s) is written in the parenthesis following each value of the population.

15° Populations

Energy Range	6.86-MeV Pop.	7.55-MeV Pop.	9.5-MeV Pop.
6-15 MeV/A	0.33(18)	1.1(4)	0.209(20)
15-40 MeV/A	0.55(12)	4.3(5)	0.245(17)
6-10 MeV/A		0.53(26)	0.082(17)
10-15 MeV/A		0.53(21)	0.107(14)
15-20 MeV/A		1.2(3)	0.076(10)
20-25 MeV/A		1.6(3)	0.105(11)
25-30 MeV/A		1.29(25)	0.053(8)
30-40 MeV/A		0.21(11)	0.010(4)

31° Populations

Energy Range	6.86-MeV Pop.	7.55-MeV Pop.	9.5-MeV Pop.
6-15 MeV/A		0.29(8)	0.043(5)
6-40 MeV/A	0.045(42)	0.39(9)	0.053(6)

64° Populations

Energy Range	6.86-MeV Pop.	7.55-MeV Pop.	9.5-MeV Pop.
6-40 MeV/A			0.0031(12)

9. $^{13}C + n$

The decay of the 8.318-MeV ($J^{\pi} = 2^{+}$, Γ = 3.4 keV) state of ^{14}C to the ground state of ^{13}C can be seen in the relative velocity spectrum for ^{13}C + n at 15° in Figure IV.34. Included in Figure IV.34 is an energy level diagram showing the decay seen in the relative velocity spectrum. Figure IV.35 contains the relative velocity spectrum for ^{13}C + n at 15° for 15 MeV/nucleon ≤ $E_{^{13}C}$ ≤ 40 MeV/nucleon and the spectrum at 31° for 6 MeV/nucleon ≤ $E_{^{13}C}$ ≤ 40 MeV/nucleon. Although other possible decays are seen in Figures IV.34 and IV.35 (see relative velocities between -2.8 cm/ns and -1.8 cm/ns), the lack of statistics does not allow a population to be reliably extracted from these decays. The populations of the 8.318-MeV state extracted from the fits to the spectra shown in Figures IV.34 and IV.35 are listed in Table IV.12.

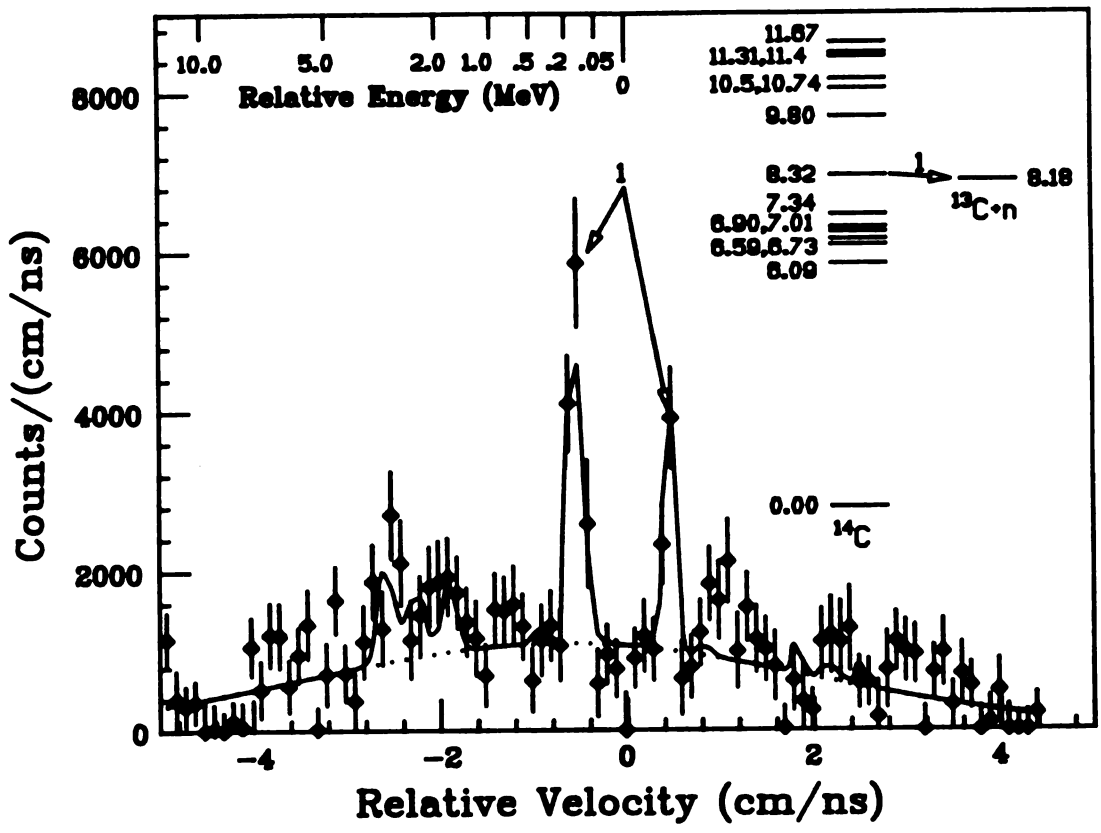

Figure IV.34 - Relative velocity spectrum for $^{13}C + n$ at 15° and for ^{13}C kinetic energies above 6 MeV/A. The resonance comes from the decay indicated in the energy level diagram. A relative energy scale is included for reference. The line shows a fit to the data using a background that is shown with the dotted line. The fit is explained in the text.

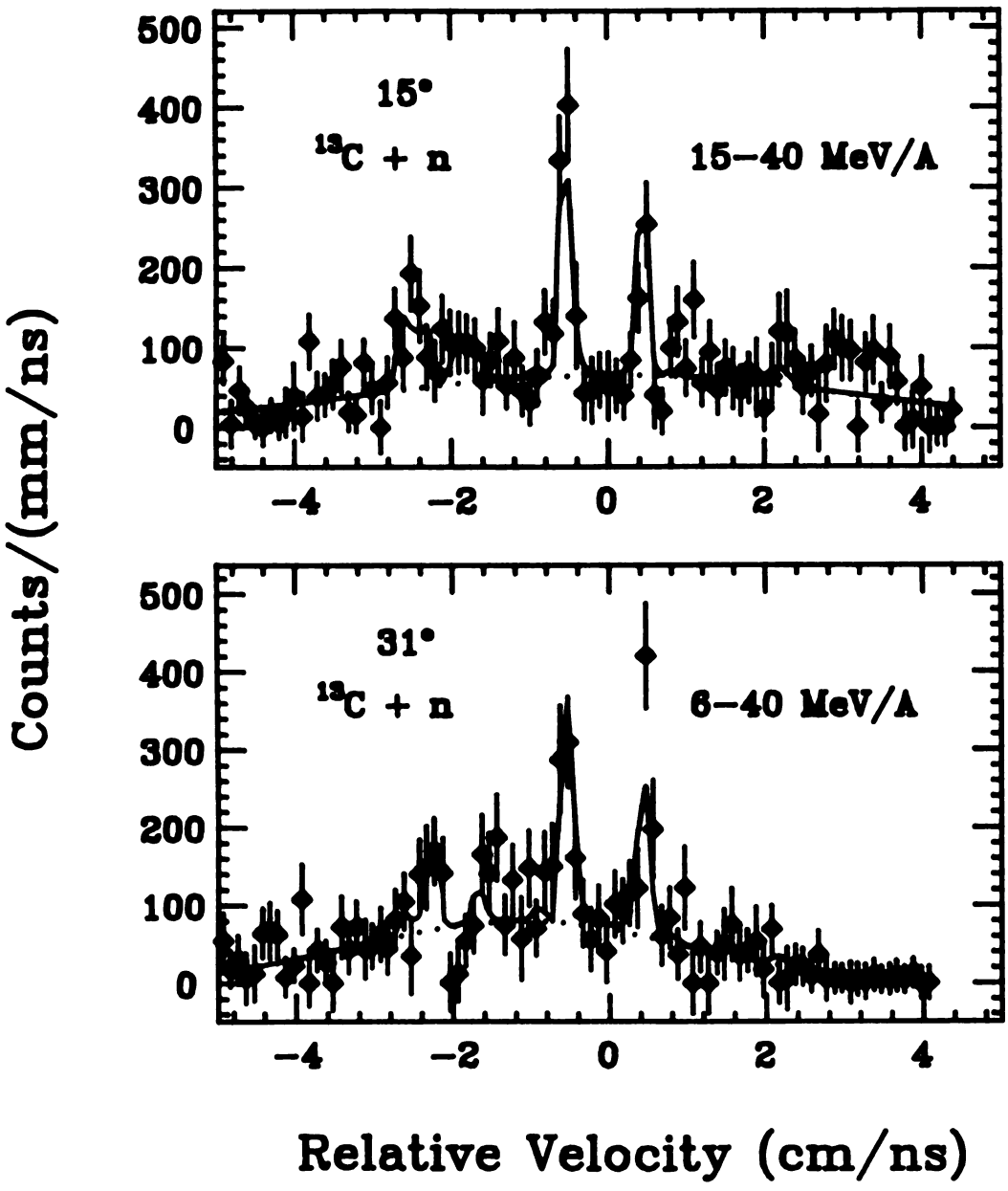

Figure IV.35 - Relative velocity spectra for ^{13}C + n at 15° and for ^{13}C kinetic energies from 6-15 MeV/A, and at 31° for kineitc energies above 6 MeV/A.

Table IV.12 - Populations of the 8.318-MeV state in ^{14}C for the indicated cuts on ^{13}C kinetic energy and for the indicated angles. The units are in mb/sr, and the uncertainty in the last significant digit(s) is written in the parenthesis following each value of the population.

15°		31°	
Energy Range	Population	Energy Range	Population
6-40 MeV/A	0.171(19)	6-40 MeV/A	0.034(5)
15-40 MeV/A	0.098(13)		

Chapter V: Comparisons of the Data with Model Predictions

As was mentioned in Chapter I, there is some evidence that suggests that DI IMFs are produced from a thermal reaction mechanism. If DI IMFs come from a thermal source, the ratios of two state populations should be described by a Boltzmann population distribution (Equation I.1). One would expect the DI population ratios from all of the IMFs to reflect the same source temperature, independent of IMF mass, since spectral temperatures derived from IMF singles spectra are independent of IMF mass (Bloc88, Deak90). A temperature can be readily calculated from the population ratios using Equation I.1, and those temperatures can be compared with each other to see if they all agree with a single source temperature. However, the effects of sequential feeding (Hahn 87) from higher-lying states into unbound-state and bound-state populations will yield an experimentally measured "apparent" temperature different from the "true", or initial, source temperature. Thus, if one is to test whether or not a large number of population ratios from different isotopes are described by a thermal source with a single temperature, the effects of sequential feeding must be taken into account.

In this chapter the population data from Chapter IV will be compared with the predictions of a sequential-decay model to determine whether or not the data can be described by a thermal reaction model. The model used in this thesis is described in Section A of this chapter. Section B compares two-level population ratios of several IMFs with the model's predictions. In Section C all of the populations of a particular

isotope that had three or more measured populations will be checked to see if they are produced from a source with a single temperature.

A. The Sequential Decay Model

The model used for this work has been reported on in several papers (Xu89, Poch85a, Poch85b, Naya89, Naya90), so only the major features will be described here. The model calculation creates a primary, or "initial", population of IMFs in bound and unbound states, with all of the populations characterized by a single temperature. The decay of these fragments is then followed until a ground-state fragment is reached. The decay of a fragment from the initial distribution may follow several steps before finally decaying to a ground-state fragment. The populations of the "final step" states, i.e., the populations of the levels that decay directly to a bound state of a fragment, are also calculated in the model. Population ratios, such as the ones measured in the laboratory, are then calculated using the final step unbound-state populations and the final ground-state populations predicted by the model.

For this thesis the model calculated the feeding from higher-lying states in nuclei with $Z \leq 13$. The model considered both discrete states and continuum states in these nuclei. When known, complete spectroscopic information (level energy, spin, parity, width, branching ratio, isospin) for each level was put in for the discrete states. When unknown, values for the spin, isospin, and parity were selected randomly from a set of most likely values that were determined from the noninteracting shell model developed by B.A. Brown of Michigan State University. Unknown branching ratios were calculated using the Hauser-Feshbach formula (Haus52). The feeding calculation was repeated for different choices of the randomly selected values to determine the uncertainty in the calculation due to these values.

The initial population of a particular level is given by:

$$P_i \propto P_o(A_i,Z_i)(2J_i+1)\exp(-E_i^*/T), \qquad (V.1)$$

where $P_o(A_i,Z_i)$ denotes the initial ground-state population. The initial population was assumed thermal up to a cutoff energy $E_{cut}=\zeta A_i$. The value of ζ used in this thesis was 5 MeV, in keeping with calculations previously done with this model. P_o has the following parameterization:

$$P_o(A_i,Z_i) \propto \exp(-fV_c/T + Q/T). \qquad (V.2)$$

V_c is the coulomb barrier for emission of a fragment or light particle from a parent nucleus and Q is the ground state Q value, where V_c and Q are given by

$$V_c = Z_i(Z_p - Z_i)e^2/\{r_o[A_i^{1/3} + (A_p - A_i)^{1/3}]\} \qquad (V.3)$$

and

$$Q = [B(A_p - A_i, Z_p - Z_i) + B_i] - B(A_p, Z_p). \qquad (V.4)$$

The value of r_o used in Equation V.3 is 1.2 fm, and the values of A and Z of the parent nucleus (A_p and Z_p in Equations V.3 and V.4) are 122 and 54, respectively (A_p and Z_p are equal to the sum of the projectile and target A and Z). The binding energies B(A,Z) in Equation V.4 were calculated from the Weizsäcker mass formula.

The parameter f of Equation V.2 was used as a fitting parameter to compare the experimental and calculated element-bound-state yields. Figure V.1 shows the best fits to the element yields for IMFs at 15° with kinetic energies above 6 MeV/nucleon for various values of T. The solid histograms in each plot in Figure V.1 represent the model

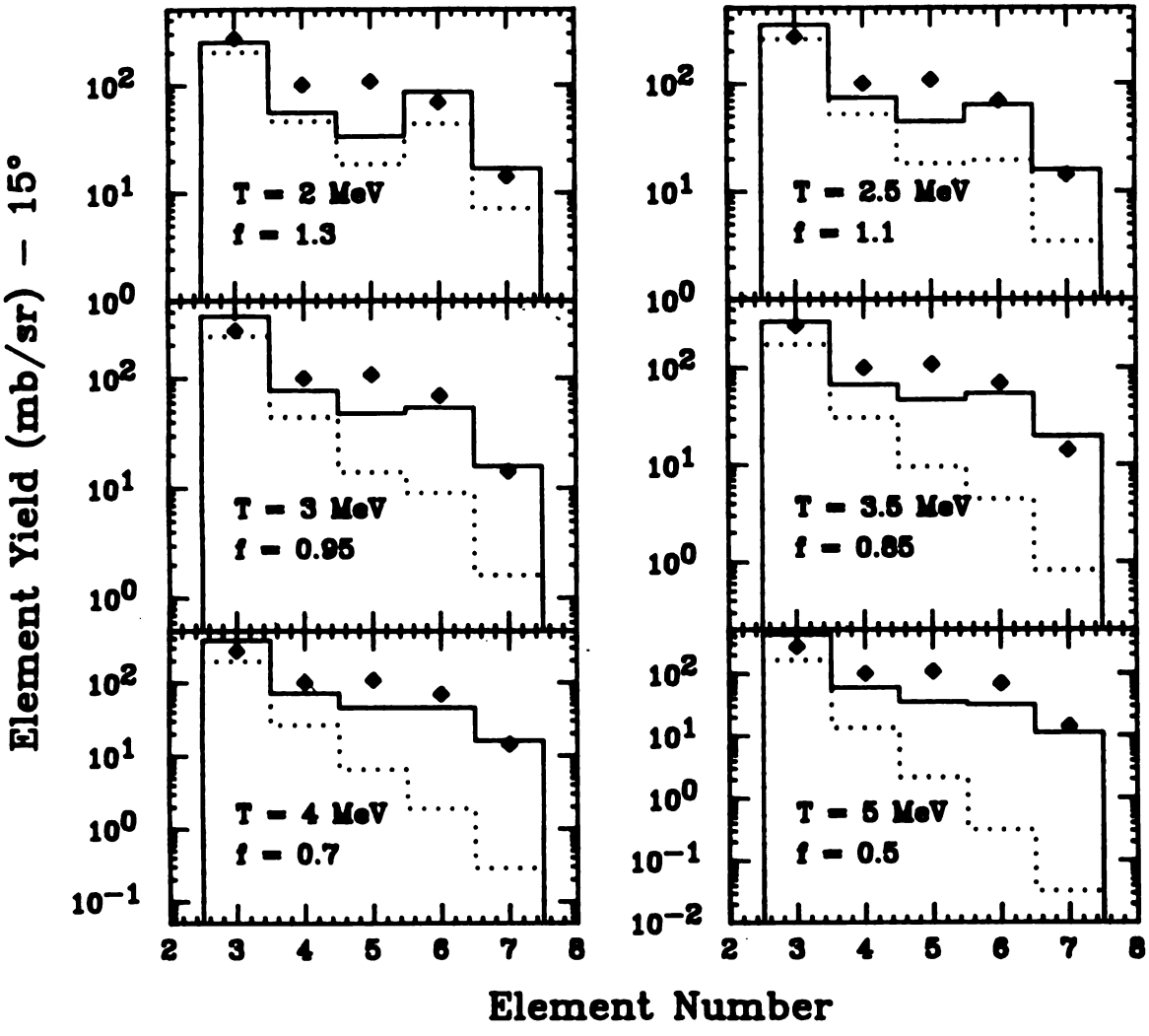

Figure V.1 - Element cross sections at 15° for Z = 3 to Z = 7. The solid histograms represent the predictions for the element cross sections from a sequential decay model. The dotted histograms represent the initial distribution of the elements in the model. The values of T and f used in the calculation (see text) are shown in each plot. The value of f shown is the value which best fit the data for the given temperature T.

predictions of the final step ground state yields using the indicated values of T and f. The dotted histograms represent the initial ground state populations as calculated by the model.

It is evident from comparing the solid histograms with the dotted histograms in Figure V.1 that the effect of feeding into the final yields increases as the atomic number increases. The effect of feeding also increases as the temperature increases. The increase of feeding with an increase of source temperature is to be expected, as one would expect the population of high-lying states to increase as the temperature increases. However, the fact that the feeding is greater for higher-Z elements is a bit surprising since the elements with a relatively lower-Z have proportionly more higher-lying states that can feed into them than do the higher-Z elements. One possible explanation for this surprising result may be that if the majority of the sequential decays are one or two-step processes, many of those high-lying states will never decay down to one of the lower-Z elements, such as lithium. For example, the ground state of ^{7}Li may be fed by the following four-step decay sequence:

$$^{14}N^{*} \rightarrow p + {}^{13}C^{*} \rightarrow \alpha + {}^{9}Be^{*} \rightarrow n + {}^{8}Be^{*} \rightarrow p + {}^{7}Li$$

If the majority of decays takes one or two steps, however, this type of decay sequence may never occur. Thus, the elements with a relatively lower Z may not have as many high-lying states feeding them as was first thought.

Figure V.2 shows the χ^2 values extracted from fits to the 15° yields (and for energies above 6 MeV/nucleon) as a function of f for a source temperature T = 2.5 MeV. From plots such as the one in Figure V.2, it is estimated that the uncertainty in f is less than 0.05. Table V.1 shows the best fit values of f as a function of IMF angle, IMF energy cut, and source temperature (T). The model predictions of the state populations in Sections B and C were calculated using the values of f from Table V.1 for the corresponding source temperatures.

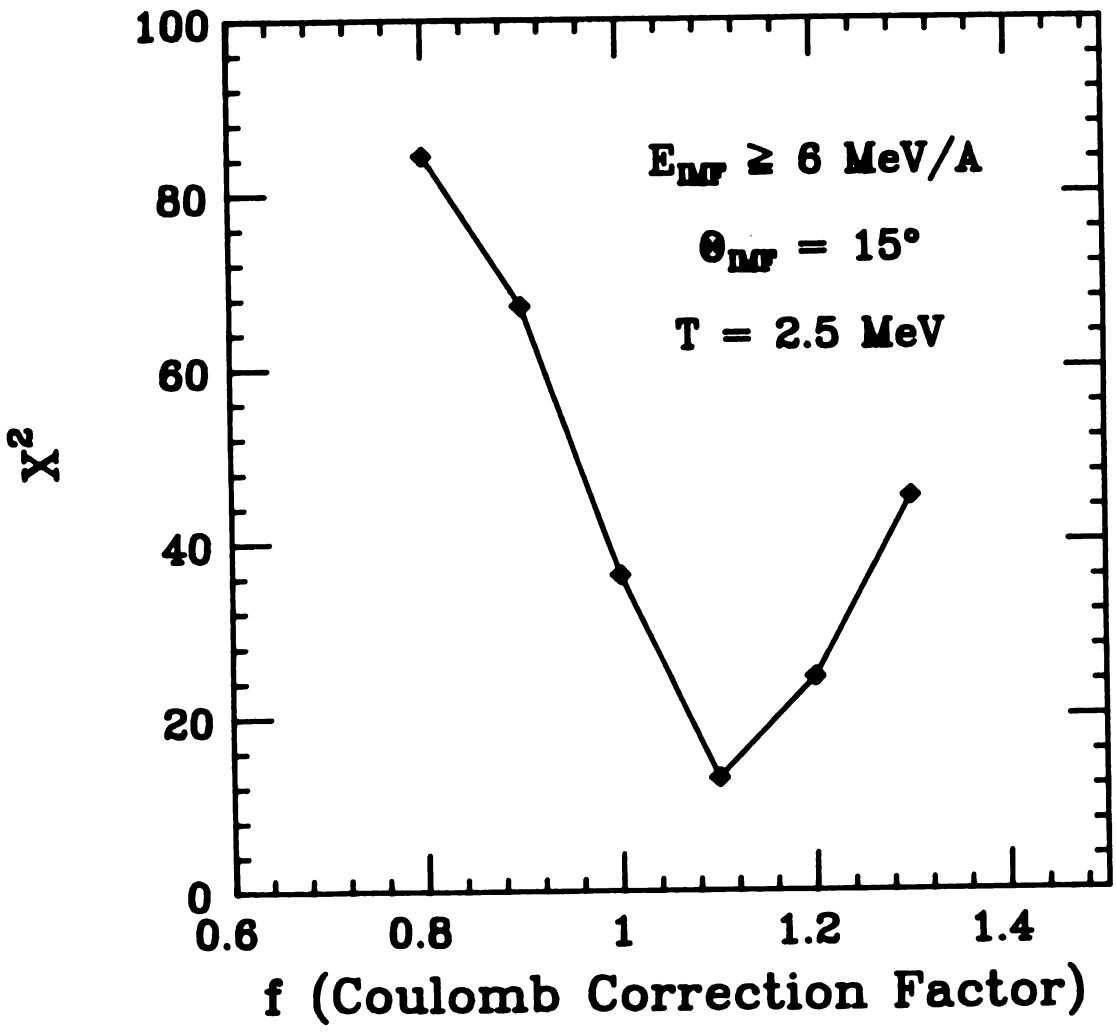

Figure V.2 - X^2 values as a function of f from fits to the element yields with the predictions of the sequential decay model. The temperature used in each fit represented in the plot was 2.5 MeV.

Table V.1 - The best values of f (see Equation V.2) for the given values of IMF angle, IMF energy cut, and source temperature. The uncertainty in f is estimated to be less than 0.05. The unit for IMF energy is MeV.

	15°			
Source Temperature	E/A ≥ 6	E/A ≥ 15	6 ≤ E/A ≤ 15	6 ≤ E/A ≤ 10
2.0 MeV	1.3	1.3	1.3	1.3
2.5 MeV	1.1	1.1	1.1	1.1
3.0 MeV	0.95	0.95	1.0	1.0
3.5 MeV	0.85	0.85	0.85	0.85
4.0 MeV	0.7	0.7	0.7	0.75
5.0 MeV	0.5	0.5	0.55	0.55

31°		64°	
Source Temperature	E/A ≥ 6	Source Temperature	E/A ≥ 6
2.0 MeV	1.2	2.0 MeV	1.0
2.5 MeV	1.1	2.5 MeV	0.9
3.0 MeV	1.0	3.0 MeV	0.8
3.5 MeV	0.8	3.5 MeV	0.7
4.0 MeV	0.7	4.0 MeV	0.6
5.0 MeV	0.5	5.0 MeV	0.45

B. Two-Level Population Ratios

As was mentioned in the introduction to this chapter, the ratio of two populations from the same nucleus may be used as a test of the thermal nature of the reaction producing DI IMFs. In this section the ratio of an unbound-state population to the bound state population is calculated using the results from Chapter V. These "two-level" population ratios are then compared to the ratios that are calculated using the "final step" state populations predicted by the model described in Section A.

In total, eleven unbound-state populations were determined from seven isotopes whose bound-state populations were also determined. The ratios of an unbound-state population to its corresponding bound-state population are shown in Figure V.3. The data are labeled with the appropriate unbound-state energy. The error bars include all of the uncertainties discussed in Chapter III. The lefthand plot in Figure V.3 is for IMFs at 15°. The open symbols are for QE ratios, and the solid symbols are for the DI ratios. The middle plot of Figure V.3 shows the data for DI IMFs at 31° and the righthand plot shows the data at 64°.

At 15°, the region of kinetic energy taken to be DI is 6-10 MeV/nucleon except for the 8.3-MeV state in ^{14}C and the 3.756-MeV state in ^{12}B, where statistics were good enough only for a cut from 6 to 15 MeV/nucleon. It was not possible to determine the populations of the 4.236-MeV state in ^{9}Li and the 9.27-MeV + 9.4-MeV states in ^{10}Be for any cuts below 15 MeV/nucleon. The percentage of QE data from 6 to 10 MeV/nucleon and from 6 to 15 MeV/nucleon for a particular isotope can be seen in Table IV.1. All of the data above 15 MeV/nucleon is at least 87% QE. Again, the percentage of QE data in a particular kinetic energy range was estimated from the analysis of IMF singles spectra using Equations IV.1 and IV.2.

The DI region at 31° was taken to be all energies above 6 MeV/nucleon, except for the 3.388-MeV and 3.756-MeV states in ^{12}B and the 7.37-MeV + 7.54-MeV group of states in ^{10}Be, where the DI region was taken to be 6-15 MeV/nucleon. The reason for

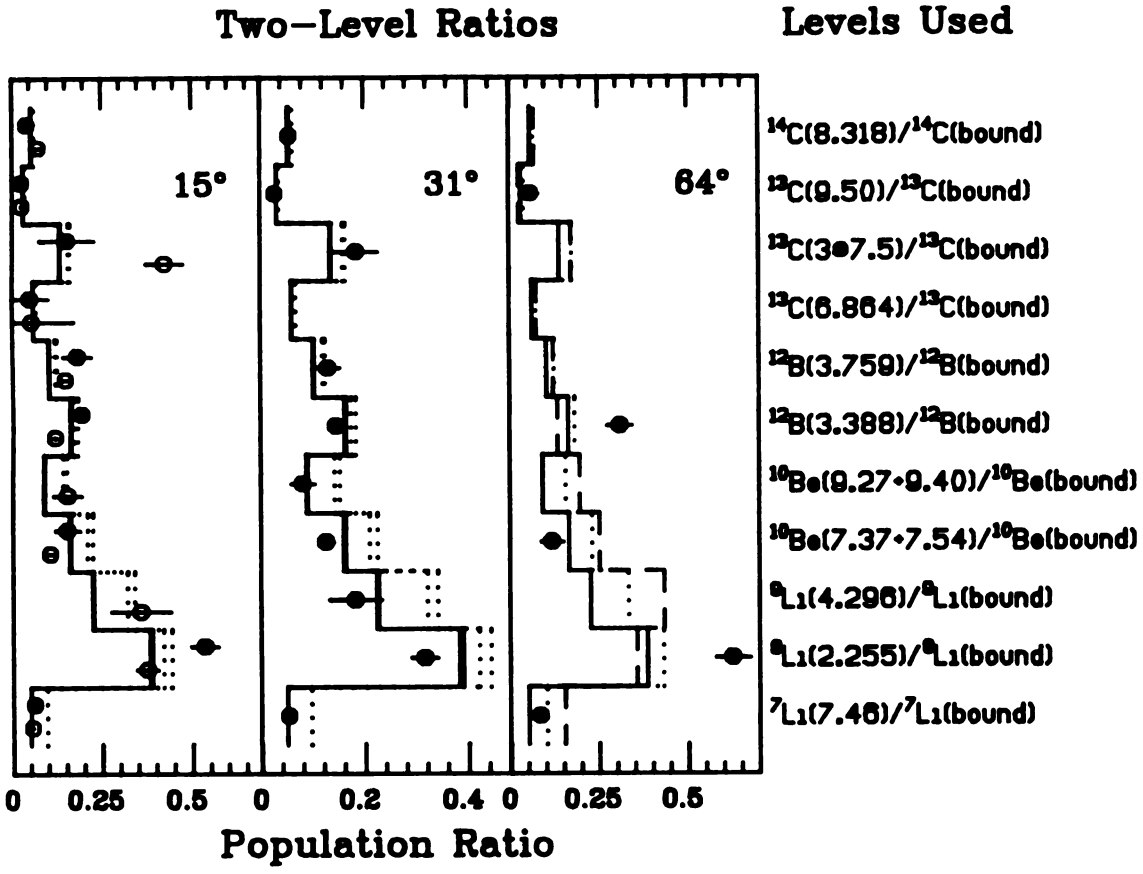

Figure V.3 - The lefthand plot contains the population ratios at 15° with the solid symbols representing the DI data and the open symbols representing the QE data. The middle plot is for DI IMFs at 31°, and the righthand plot is for DI IMFs at 64°. The solid histograms in every plot indicate the ratios calculated from a sequential feeding model for T_{source}=2.5MeV, and the dotted histograms indicate the calculated ratios for T_{source}=3.5 MeV. The dashed line in the righthand plot indicates the ratios predicted by the sequential feeding model for T_{source}= 6.0 MeV. The bound states and unbound states used to calculate the ratios are shown on the righthand side of the figure.

taking a smaller kinetic energy gate was to reduce the amount of contamination from QE processes. Statistics were not good enough to take the 6-15 MeV/nucleon gate for the 9.27-MeV + 9.4-MeV group of states in ^{10}Be, so the gate used in this case was E $\geq$ 6 MeV/nucleon. All of the data at 64° is DI.

The histograms in Figure V.3 represent the population ratios calculated with the final bound-state and unbound-state populations predicted by the sequential decay model. Looking at Figure V.3, one notes that for each initial source temperature there is a pair of histograms showing the prediction of the measured population ratio. The pair of histograms represents the uncertainty in the calculation by showing the highest and lowest values of the population ratio obtained from the feeding model calculations.

The dotted histograms in Figure V.3 show the predictions of the population ratios for an initial source temperature of 3.5 MeV, and the solid histograms show the predictions for a temperature of 2.5 MeV. It is in this range of initial source temperatures that the model best predicts the measured DI population ratios. The dashed line in the righthand plot is for a source temperature of 6.0 MeV.

Looking at the DI population ratios at 15° (solid symbols), it is seen that seven of the nine ratios are fitted by the model predictions for initial temperatures between 2.5 and 3.5 MeV. Of the two that were not fitted, only one, that being the 2.255-MeV state in ^{8}Li, is more than two standard deviations away from the model predictions. This may not be surprising since 43% of the inclusive ^{8}Li data in this region comes from QE processes. At 31°, eight of the ten DI population ratios are fitted by the model calculations for source temperatures between 2.5 and 3.5 MeV.

Based on the results for DI ratios at 15° and 31°, it appears that the data is consistent with production from a thermal source whose temperature is between 2.5 and 3.5 MeV. However, the data at 64° cannot be fitted by the model predictions, even for a range of 2.5 to 6 MeV. Only one point, the point for the 9.5-MeV state in ^{13}C, agrees with the model predictions with source temperatures between 2.5 and 3.5 MeV. The

point for the 7.46-MeV state in ^{7}Li agrees with a source temperature between 3.5 and 6 MeV, but the other three points are outside the range between 2.5 and 6 MeV.

Looking at the data and model predictions for the 3.388-MeV state in ^{12}B and the 7.37-MeV + 7.54-MeV states in ^{10}Be at 64°, it appears that no model calculation will agree with the data. As the source temperature increases from 2.5 to 3.5 MeV the predicted ratio also increases, but as the temperature increases to 6 MeV, the predicted ratio decreases to a value below the prediction for 2.5 MeV. This indicates that the model predicts a maximum value of the ratio that is below the measured ratio in both cases.

It is interesting to note that, for the most part, the measured DI and QE population ratios at 15° (Figure V.3) are similar. The noteable exceptions are the group of states near 7.5 MeV in ^{13}C, the 3.388-MeV state in ^{12}B, and the 7.37-MeV + 7.54-MeV pair of states in ^{10}Be. Otherwise, it appears that the population ratios for QE IMFs are similar to those for DI IMFs. Thus, the amount of QE contamination in a predominantly DI region does not produce a significant error in the determination of R for the DI process, in most cases.

C. Multilevel Populations

Another test which can be applied to the DI population data to see if they are consistent with emission from a thermal source is to check whether three or more populations from the same nucleus can be fitted with a single temperature. Figure V.4 shows a plot of the natural logarithm of the population (divided by the appropriate spin factor) of each of the three unbound states and of the bound states detected for ^{13}C at 15° for the indicated cuts on fragment energy. Each point is plotted at its appropriate level energy. All of the bound states were treated as a single state whose level energy is 2.3 MeV, and whose effective spin factor (2J+1) is 12.22 (see Appendix A).

If all four groups of states were populated according to a Boltzmann population distribution, and if the effect of sequential feeding was negligible, then all four points in

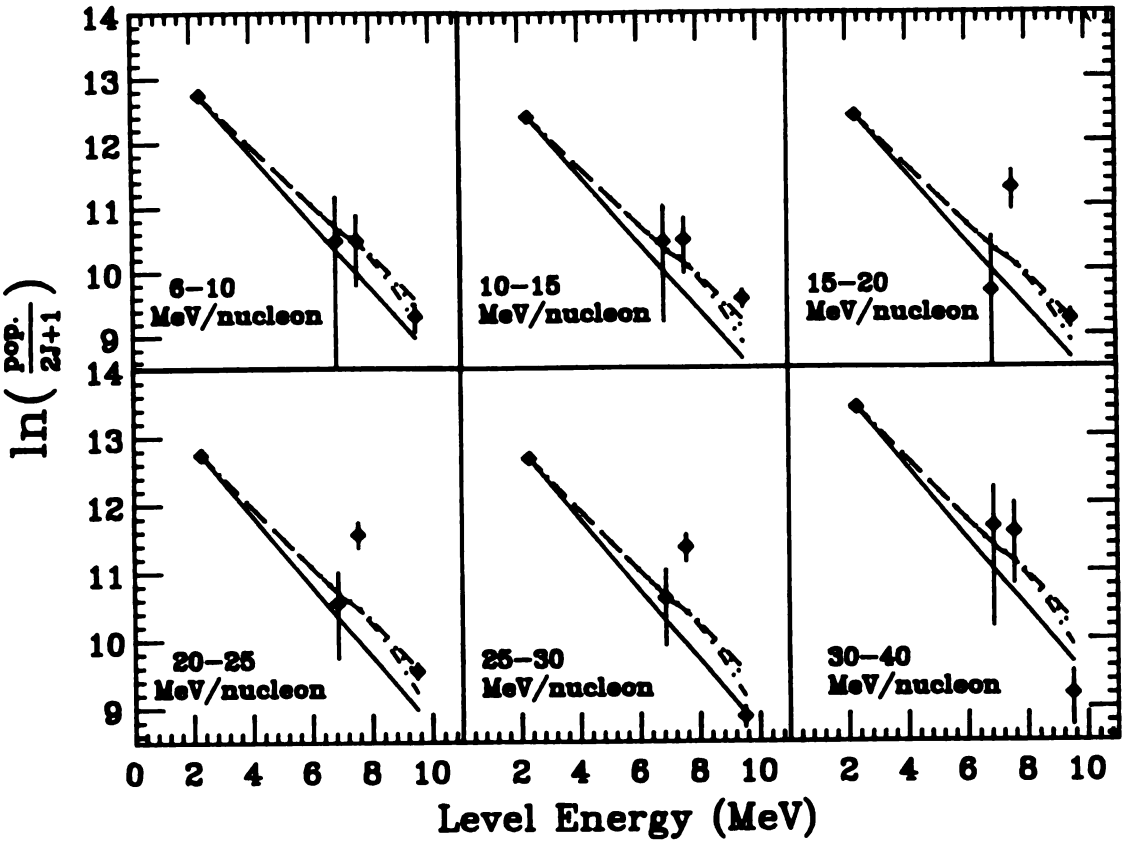

Figure V.4 - Plots of the natural logarithm of the populations of the detected levels in ^{11}C versus the level energy for various cuts on fragment kinetic energy. The solid, dashed, dotted, and dot-dashed lines in each plot show the predictions from the sequential feeding model for initial source temperatures of 2, 3, 4, and 5 MeV, respectively.

each plot of Figure V.4 would lie on a straight line. This appears to be the case for $E_{^{12}C}$ between 6 and 10 MeV/nucleon and for $E_{^{12}C}$ between 10 and 15 MeV/nucleon. The solid, dashed, dotted and dot-dashed lines in each plot indicate the predicted populations (relative to the bound-state population) from the sequential feeding model for initial temperatures of 2, 3, 4 and 5 MeV, respectively. Below 10 MeV/nucleon, the data is fitted with the model calculations using initial temperatures of 3, 4, and 5 MeV. The data for 10-15 MeV/nucleon is nearly fitted with the model calculation. According to Table IV.1, 25% of the bound-state yield below 15 MeV/nucleon is quasielastic, while below 10 MeV/nucleon it is 12%. Thus it appears that for the ^{13}C data dominated by DI processes, the measured populations are indicative of a thermal reaction mechanism. Above 15 MeV/nucleon none of the data can be fitted with the model calculation, although the data from 30-40 MeV/nucleon is nearly fitted. This is consistent with the assumption of a nonthermal reaction mechanism for the production of QE IMFs.

Figure V.5 shows the plot of the logarithm of three populations in ^{12}B, the 3.76-MeV state, the 3.388-MeV state, and the bound states. The bound states were treated as the a single state with a level-energy of 1.13 MeV and an effective spin factor of 16.35. The left plot in Figure V.5 is for 15° and 6-15 MeV/nucleon, the middle plot is for 15° and 15-40 MeV/nucleon, and the right plot is for 31° and 6-15 MeV/nucleon. The lines represent the same temperatures as in Figure V.4. As in Figure V.4, the QE data (middle plot) is not fitted by any of the model predictions. However, none of the DI data is fitted, either, which is in contrast to the results presented in Figure V.4, where the DI data is fitted and the QE data is not.

Figure V.6 shows plots of the logarithm of three populations in ^{10}Be, the 7.37-MeV + 7.54-MeV group of states, the 9.27-MeV + 9.4-MeV group of states, and the bound states. The bound states were plotted as a single state with an energy of 3.7 MeV and an effective spin factor of 15.95. The left plot is for 15° and kinetic energies above 15

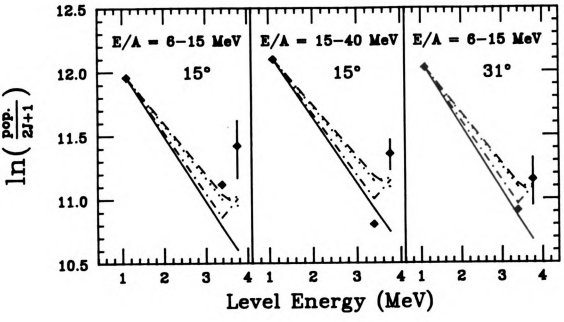

Figure V.5 - Plots of the natural logarithm of the populations of the detected levels in ^{11}B versus the level energy for various cuts on IMF energy at 15° and 31°. The lines have the same meaning as in Figure V.4.

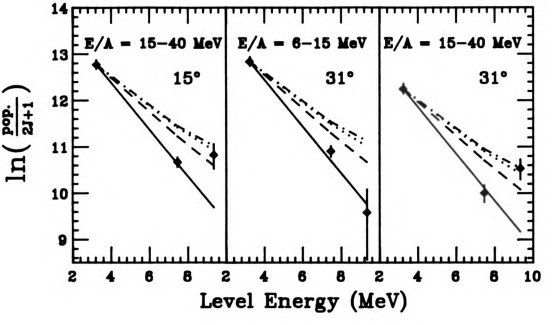

Figure V.6 - Plots of the natural logarithm of the populations of the detected levels in ^{10}Be versus the level energy for various cuts on IMF energy at 15° and 31°. The lines have the same meaning as in Figure V.4.

MeV/nucleon, the middle plot is for 31° and energies below 15 MeV/nucleon, and the right plot is for 31° and energies above 15 MeV/nucleon. The lines represent the same temperatures as in Figures V.4 and V.5. As in Figures V.4 and V.6 the QE data (above 15 MeV/nucleon) cannot be fitted with a single temperature. It appears that the DI data (31° below 15 MeV/nucleon) can be fitted with a temperature between 2 and 3 MeV.

In regards to the nature of the DI reaction mechanism, the results from the two-level and multilevel data are not clear. Some of the DI data can be fitted with a thermal model, but there are some exceptions which are not fitted. What this set of data may indicate is that the DI reaction mechanism may indeed be thermal in nature, but that there are other effects present during the reaction which are not accounted for in the model which can alter some of the measured populations such that they appear to be nonthermal. One such effect could be final-state interactions (Boal84), for example. The data may also indicate that while feeding calculations like the one used here may be generally correct, it may not be correct for every final state.

Chapter VI: R versus Kinetic Energy

While there are a few cases shown in Chapter V where the QE population data is clearly different than the DI population data, for the most part no distinction can be made between the two. However, it should be pointed out that up to this point most of the data shown has been for rather large cuts on IMF kinetic energy. The difference between QE and DI data becomes more obvious when the populations are examined with smaller cuts on kinetic energy, particularly when R (Equation I.1) is plotted as a function of the kinetic energy. For four isotopes, namely ^{7}Li, ^{8}Li, ^{12}B, and ^{13}C, statistics were good enough to take smaller gates on kinetic energy.

The dependence of the ratio of an unbound-state population to the bound-state population on IMF kinetic energy is shown for the 7.456-MeV state in ^{7}Li, the 2.255-MeV state in ^{8}Li, the 3.388-MeV state in ^{12}B, and the 9.5-MeV state and 7.5-MeV group of states in ^{13}C in Figures VI.1-VI.4, respectively. The upper plots show R versus kinetic energy, while the lower plots show the corresponding singles spectra. In Figure VI.1, the filled points show the data after correcting the inclusive spectra for ^{8}Be contamination, and the open symbols show the data before the correction. The top plot in Figure VI.4 is for the group of three states near 7.5-MeV in ^{13}C, and the middle plot is for the 9.5-MeV state. For reference, a temperature scale computed using Equation I.1 without corrections for feeding is included in the upper plots of Figures VI.1-VI.4. The numbers in the upper plots indicate the percentage of QE data in the bound-state yield at a particular energy gate.

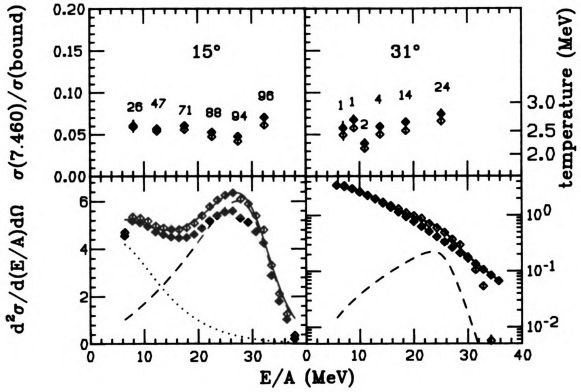

Figure VI.1 - The upper plots show the ratio of the population of the neutron-unbound 7.46–MeV state in ^{7}Li to the ^{7}Li bound-state population as a function of fragment kinetic energy at 15° and 31°. Open symbols represent the data before correcting for ^{8}Be contamination, and filled symbols represent the data after the correction. The temperature scale on the right hand side was deduced from Equation I.1. The lower plots show the ^{7}Li singles spectra at 15° and 31°. The open and filled symbols have the same meanings as for the upper plots. The solid, dotted, and dashed lines are from a fit described in the text. The numbers in the upper two plots indicate the percentage of QE ^{7}Li in the bound-state yield for the corresponding energy bin.

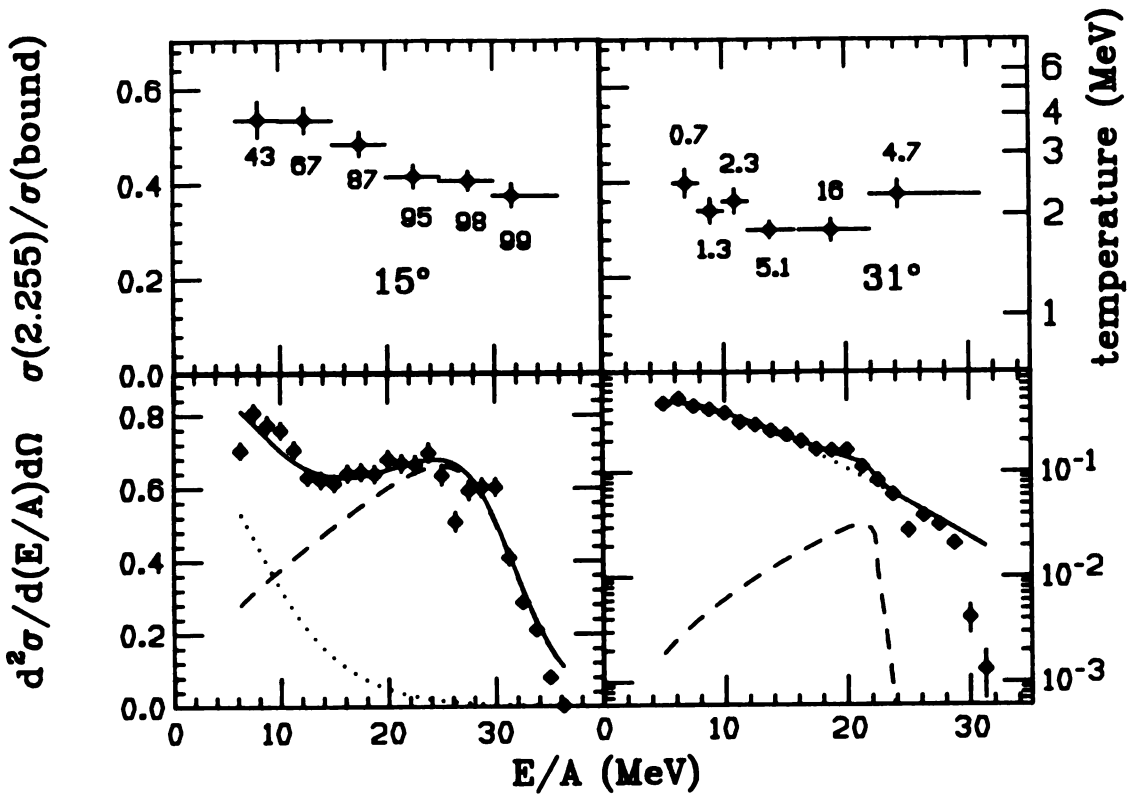

Figure VI.2 - The upper plots show the ratio of the population of the neutron-unbound 2.255–MeV state in ^{8}Li to the ^{8}Li bound-state population as a function of fragment kinetic energy at 15° and 31°. The lower plots show ^{8}Li singles spectra at 15° and 31°. The solid, dotted, and dashed lines are from a fit described in the text. The numbers in the upper two plots indicate the percentage of QE ^{8}Li in the bound-state yield for the corresponding energy bin.

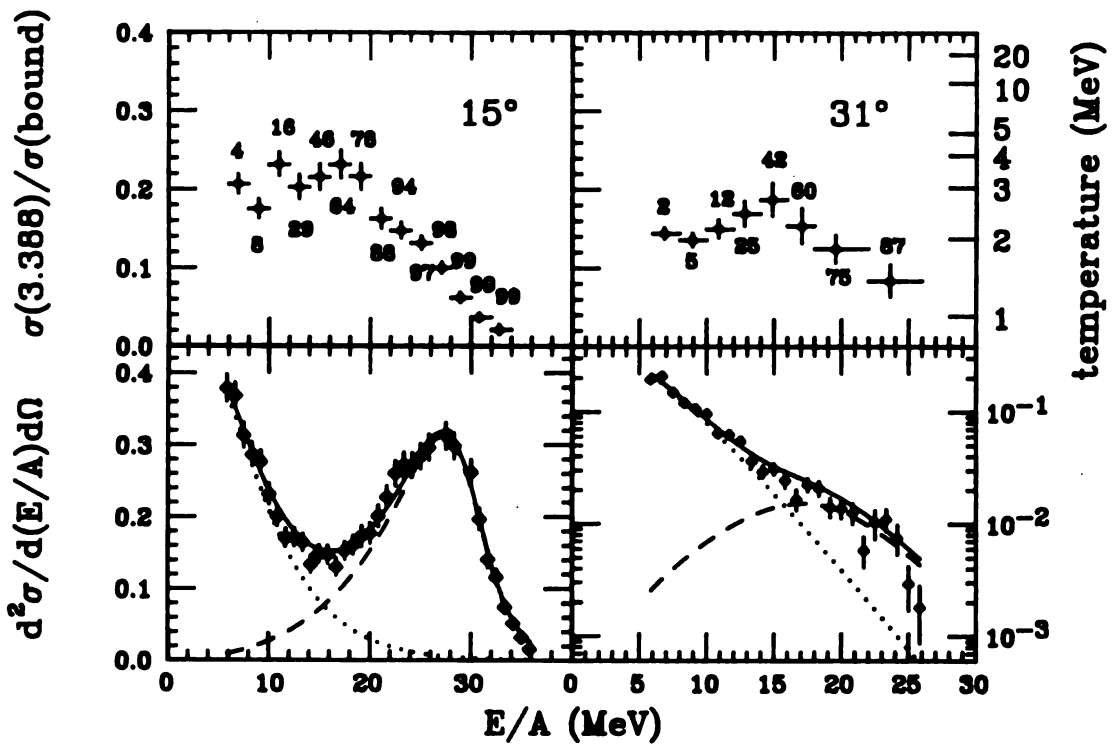

Figure VI.3 - The upper plots show the ratio of the population of the neutron-unbound 3.388–MeV state in ^{12}B to the ^{12}B bound-state population as a function of fragment kinetic energy at 15° and 31°. The lower plots show ^{12}B singles spectra at 15° and 31°. The solid, dotted, and dashed lines are from fits described in the text. The numbers in the upper plots indicate the percentage of QE ^{12}B in the bound-state yield for the corresponding energy bin.

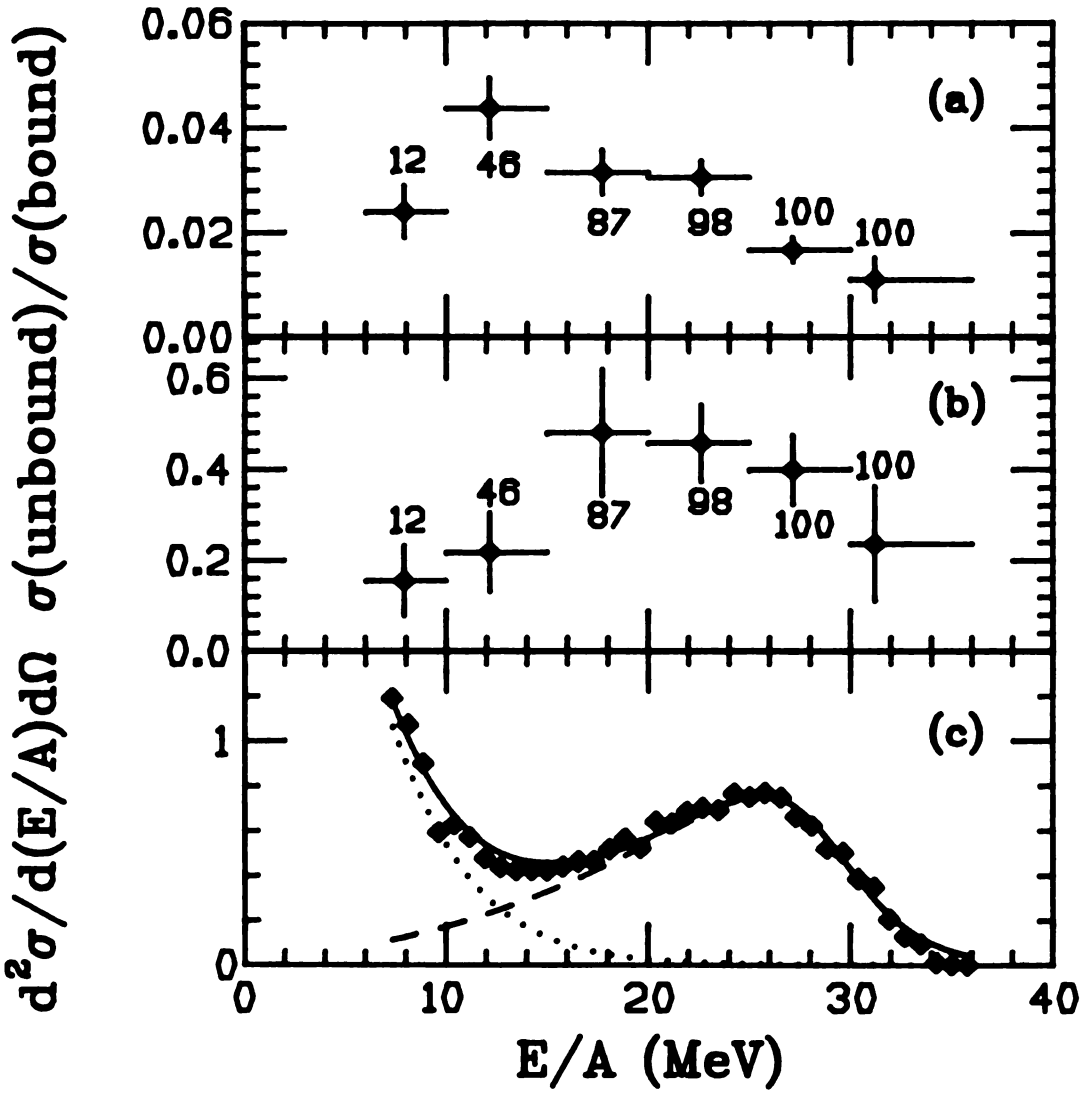

Figure VI.4 - (a) and (b) show the population ratios of neutron-unbound states in ^{11}C to the ^{11}C bound states as a function of ^{12}C kinetic energy at 15°. In (a) the unbound state is at 9.50 MeV, and in (b) there are three unresolved unbound states at 7.49-MeV, 7.55-MeV, and 7.69-MeV. The numbers in (a) and (b) indicate the percentage of QE ^{11}C in the bound-state yield for the corresponding energy bin. (c) shows the ^{11}C singles spectrum at 15°. The solid, dotted, and dashed lines are from a fit described in the text.

A. QE IMFs

The dependence of R on IMF kinetic energy for QE events may be seen in Figures VI.1-VI.4 for large kinetic energies. It is interesting to note that for the two isotopes with a mass close to the mass of the projectile, ^{12}B and ^{13}C (Figures VI.3 and VI.4), the ratio decreases as the fragment kinetic energy increases, and it appears that the ratio goes to zero as the fragment velocity approaches the beam velocity. However, for the two isotopes with about half the mass of the projectile, ^{7}Li and ^{8}Li (Figures VI.1 and VI.2), the ratio appears to be constant, or decreasing slightly, with the ratio still above zero for fragment velocities near the beam velocity. In terms of a nucleon-exchange model, the difference in R versus kinetic energy between IMFs with half-beam mass and near-beam mass is consistent with the picture of collisions with smaller impact parameter (hence more mixing between target and projectile nucleons) for the lower-mass IMFs. Even for IMF velocities near the velocity of the beam, one might expect that the lower-mass IMFs to be in a higher state of excitation than the higher-mass IMFs since a projectile which has lost half of its nucleons is much more deformed than a projectile that has lost only one or two nucleons.

The dependence of R versus kinetic energy was measured for the 6.8-MeV state in ^{11}B and the 4.4-MeV state in ^{12}C for projectilelike fragments created in the E/A = 20 MeV, ^{14}N + ^{164}Dy reaction, and it was found that the ratio was essentially constant with kinetic energy and above zero near the velocity of the beam (Siwe85). Note that these results are quite different from the results presented here for IMFs with similar mass, namely ^{12}B and ^{13}C. In fact, their results more closely resemble the results presented here for ^{7}Li and ^{8}Li. It is not known if the discrepancy between the results here and those of (Siwe85) is due to the different beam energy and target or due to the fact that one set of ratios is for unbound states, and the other is for bound states. Regardless, measurements such as these give an indication of the amount of excitation energy deposited in the QE fragment, and the dependence of the ratio on kinetic energy

may bear important information on the details of models used to predict the production of QE IMFs, such as the nucleon-exchange model (Wilc89) or the participant-spectator model (Deak89).

B. DI IMFs

The kinetic energy dependence of the ratio of an unbound-state population to a bound-state population for DI IMFs may be seen in Figures VI.1 and VI.4 at 31° and in Figure VI.3 for low energies at 15° and 31°. The dependence of the ratio of the 2.255-MeV state population in ^{8}Li (Figure VI.2) to the bound-state population on kinetic energy indicates a slightly decreasing or constant ratio with increasing kinetic energy. A constant ratio would be consistent with emission from a thermal source, assuming that effects due to evaporative cooling could be neglected. The data for the 7.46-MeV state in ^{7}Li (Figure VI.1) and the 3.388-MeV state in ^{12}B (Figure VI.3) are consistent with the dependence of the ratio on kinetic energy observed for the 2.255-MeV state in ^{8}Li, although there is clearly a need for data at lower fragment kinetic energies to firmly establish this dependence for DI IMFs.

Chapter VII: Measured Feeding into Bound States

Although the effects of sequential feeding will alter the measured populations from their initial distributions, very little data exists that measures the magnitude of the feeding into the bound states. Because of this, most analyses have relied on model calculations to correct their data for feeding, just as has been done in this thesis. The amount of feeding through several neutron-unbound channels into bound states has been measured, and this data can be used as a check on the accuracy of feeding calculations used for this work.

Table VII.1 shows the percentage of a bound-state population that came from the decay of a neutron-unbound state. For example, 1.5 % of the ^{11}B bound-state yield at 15° was ^{11}B that came from the decay of the 3.388-MeV state in ^{12}B. The last six columns show the predictions for the amount of feeding according the sequential feeding model calculations, using initial temperatures of 2 MeV, 2.5 MeV, 3 MeV, 3.5 MeV, 4 MeV, and 5 MeV. Most of the data matches the model calculations for an initial temperature between 2.5 and 4 MeV, which is in agreement with the temperatures fitted with the DI population data. The model calculations could not match the data within uncertainties for one case, that being the feeding at 15° from the group of three levels around 7.5 MeV in ^{13}C to the ground state of ^{12}C.

The idea of sequential feeding was first introduced as a possible explanation for the discrepancy between population temperatures and spectral temperatures. It was thought that accounting for the feeding would raise the initial population temperatures enough that they would agree with the spectral temperatures. Although feeding does raise the population temperatures, it is not enough to account for the difference.

Table VII.1 - Percent feeding from neutron-unbound states into their corresponding daughter-fragment inclusive yields at various angles. The uncertainty in the last significant digit(s) is enclosed in the parenthesis following the value of the feeding. The last 6 columns show predictions for the percent feeding from a sequential feeding calculation described in the text. The initial temperature used in the calculation is indicated in the column heading.

parent state	Θ	exp % feeding	model 2 MeV	model 2.5 MeV	model 3 MeV	model 3.5 MeV	model 4 MeV	model 5 MeV
^{7}Li(7.46)	15°	5.0(3)	2.1	5.1	8.7	12.3	15.4	20.5
^{7}Li(7.46)	31°	5.0(3)	2.2	5.1	8.7	12.3	16.0	21.6
^{7}Li(7.46)	64°	8.7(7)	2.2	5.3	9.0	13.2	16.5	21.6
^{8}Li(2.255)	15°	6.6(3)	1.2	2.8	4.7	6.8	8.6	11.7
^{8}Li(2.255)	31°	9.3(5)	1.2	2.8	4.8	6.8	9.0	12.3
^{8}Li(2.255)	64°	7.6(5)	1.2	2.9	5.0	7.4	9.3	12.3
^{9}Li(4.296)	15°	4.3(10)	0.5	1.2	2.1	3.1	4.1	5.8
^{9}Li(4.296)	31°	3.8(10)	0.5	1.2	2.1	3.1	4.1	5.8
^{8}Be(19.23)	15°	4.0(2)	1.5	3.6	6.1	9.0	11.9	17.3
^{8}Be(19.23)	31°	3.1(3)	1.5	3.6	6.2	9.0	11.9	17.1
^{10}Be(7.5)	15°	6.6(6)	2.3	5.7	9.5	13.1	15.7	18.7
^{10}Be(7.5)	31°	6.5(6)	2.4	5.7	9.7	13.1	16.3	20.0
^{10}Be(7.5)	64°	4.9(6)	2.4	5.8	9.9	14.0	16.8	20.0
^{10}Be(9.5)	15°	6.(2)	1.	3.	6.	9.	11.	14.
^{10}Be(9.5)	31°	4.2(12)	1.1	3.1	6.0	8.8	11.6	15.1
Σ^{10}Be	15°	12.(2)	3.	9.	15.	22.	27.	33.
Σ^{10}Be	31°	10.7(13)	3.4	8.8	15.6	22.0	27.9	35.1
^{11}Be(3.89)	15°	1.20(4)	0.13	0.34	0.61	0.91	1.21	1.75
^{11}Be(3.89)	31°	0.80(4)	0.13	0.34	0.62	0.91	1.23	1.82
^{11}Be(3.89)	64°	1.3(3)	0.1	0.4	0.6	0.9	1.3	1.8

Table VII.1 (cont'd.).

parent state	Θ	exp % feeding	model 2 MeV	model 2.5 MeV	model 3 MeV	model 3.5 MeV	model 4 MeV	model 5 MeV
^{11}Be(3.96)	15°	1.10(14)	0.25	0.66	1.19	1.78	2.35	3.38
^{11}Be(3.96)	31°	0.60(11)	0.26	0.66	1.20	1.78	2.41	3.52
Σ^{11}Be	15°	2.69(14)	0.38	1.00	1.80	2.69	3.56	5.13
Σ^{11}Be	31°	1.30(12)	0.39	1.00	1.82	2.69	3.64	5.34
^{12}B(3.388)	15°	1.50(3)	1.15	2.03	2.55	2.82	2.80	2.56
^{12}B(3.388)	31°	1.60(4)	1.17	2.03	2.61	2.82	2.92	2.76
^{12}B(3.388)	64°	2.7(3)	1.2	2.1	2.7	3.1	3.0	2.8
^{12}B(3.76)	15°	1.70(18)	0.68	1.27	1.67	1.94	2.04	2.12
^{12}B(3.76)	31°	1.3(2)	0.7	1.3	1.7	1.9	2.1	2.3
Σ^{12}B	15°	3.20(18)	1.83	3.30	4.22	4.76	4.84	4.68
Σ^{12}B	31°	2.9(2)	1.9	3.3	4.3	4.8	5.0	5.0
^{13}C(6.86)	15°	2.7(8)	1.9	3.7	4.8	5.3	5.1	4.6
^{13}C(6.86)	31°	1.4(13)	1.9	3.7	5.0	5.3	5.5	5.4
^{13}C(7.5)	15°	16.(2)	4.	8.	11.	13.	12.	11.
^{13}C(7.5)	31°	12.(3)	4.	8.	12.	13.	13.	13.
^{13}C(9.5)	15°	1.50(8)	0.81	1.95	2.64	2.78	2.41	1.78
^{13}C(9.5)	31°	1.9(2)	0.8	2.0	2.7	2.8	2.7	2.2
^{13}C(9.5)	64°	3.5(12)	0.8	2.1	2.9	3.3	2.9	2.2
Σ^{13}C	15°	21.(2)	7.	14.	19.	21.	20.	18.
Σ^{13}C	31°	16.(3)	7.	14.	20.	21.	22.	20.
^{14}C(8.32)	15°	1.10(12)	1.25	2.10	2.51	2.72	2.68	2.56
^{14}C(8.32)	31°	1.6(2)	1.3	2.1	2.6	2.7	2.9	2.9

However, no attempt has been made to see what effect feeding has on the measured spectral temperatures. If the feeding is dependent on the kinetic energy, then correcting the IMF spectra for the feeding will also be energy dependent. This, then, will change the slope of the spectrum, which in turn will have an effect on the deduced spectral temperature.

The dependence of the feeding on kinetic energy has been measured in detail for one case, that being the feeding from the 3.388-MeV state in ^{12}B to the ground state of ^{11}B. According to Table VII.1, the best value of the initial temperature that matches the feeding from both of the detected neutron-unbound states in ^{12}B is ~2.5 MeV. Using that initial temperature, the model predicts that ~33 % of the yield of ^{11}B at 15° and 31° comes from feeding from all of the possible decay channels that end up in a bound state of ^{11}B. The top two plots in Figure VII.1 show the fraction of feeding into ^{11}B from the 3.388-MeV state in ^{12}B at 15° and 31° as a function of ^{11}B kinetic energy. The solid lines show a convenient fit to the data. The lower two plots show the measured ^{11}B inclusive spectra at 15° and 31° (open symbols) and the spectra corrected for feeding (solid symbols) using a value of 33 % for total feeding. The dependence of the feeding on kinetic energy for all of the possible channels was assumed to be the same as the dependence for the one channel which was measured.

The solid lines through the corrected and uncorrected spectra in the lower plots indicate the fits using the sum of two functions. One function was used to fit the DI part of the two spectra at 15° and 31°, and it has the standarad parameterization of a thermal moving source. Equation IV.2 was used for the other function, which was used to fit the QE part of the data. Only the data at 15° and 31° was used for the fitting. The dotted lines in the lower plots show the contribution from the moving source for the uncorrected data, and the dashed lines show the contribution from the moving source for the corrected data. The value of the temperature of the moving source changed from 11.2 MeV before correcting for feeding to 14.0 MeV after the correction for feeding. The

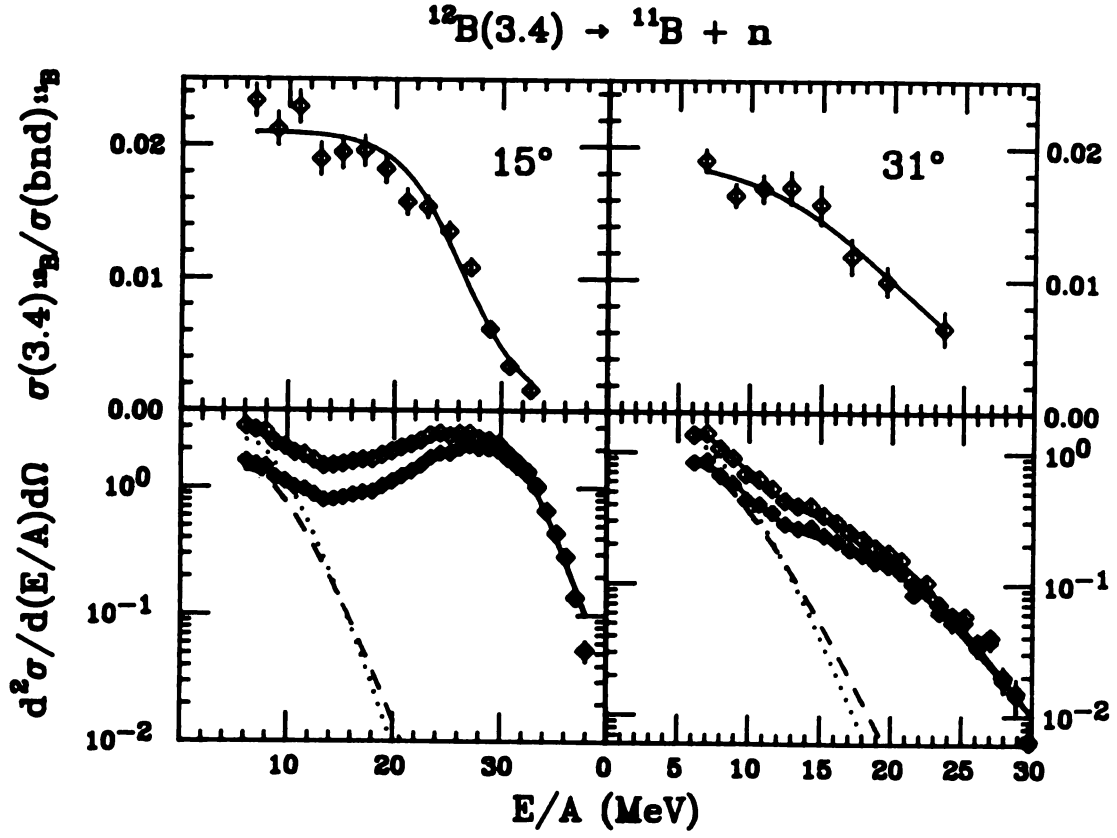

Figure VII.1 - The upper plots show the ratio of the population of the 3.388-MeV state in ^{12}B to the bound-state population of ^{11}B as a function of ^{11}B kinetic energy. The solid lines are a fit to the data. The open symbols in the lower plots show the singles cross section of ^{11}B at 15° and 31° before correcting for feeding, and the closed symbols show the cross sections after the correction. The solid, dashed, and dotted lines in the lower plots come from a fit described in the text.

statistical uncertainty of the value of the temperature is less than 5%, in both cases. It appears, then, that correcting for feeding will increase the spectral temperature extracted from ^{11}B singles spectra, just as correcting for feeding will also increase the population temperatures. Based on these results, the effects of sequential feeding cannot account for the discrepancy between population temperatures and spectral temperatures.

Chapter VIII: Summary and Conclusions

A. Summary

The populations of eleven neutron-unbound states in seven IMFs were measured at 15°, 31°, and 64°, along with the bound-state populations of those seven IMFs. The ratios of unbound-state to bound-state populations for DI IMFs at 15° and 31° were fitted with a statistical sequential decay model using a single initial source temperature between 2.5 and 3.5 MeV. This finding supports the assumption of a statistical, or thermal, origin for DI IMFs. However, at 64°, where all of the IMFs come from DI reactions, fits to most of the measured population ratios were not possible with the sequential decay model. Although the DI and QE reaction mechanisms are quite different, there was basically no difference between QE and DI two-level population ratios for most IMFs.

It is possible to fit the populations of four groups of states detected in ^{13}C (bound states + 3 groups of unbound states) with a single temperature at 15° and $E_{^{13}C} \leq$ 15 MeV/nucleon. This is additional evidence of a thermal origin of DI IMFs. Also, above 15 MeV/nucleon, where QE reactions dominate, the four groups of populations in ^{13}C cannot be fitted. However, the populations of three groups of states in ^{12}B (bound states + 2 unbound states) could not be fitted with a single temperature for either DI or QE reactions.

The functional dependence of the ratio of a neutron-unbound state population to a bound-state population on IMF kinetic energy was investigated for several QE and DI IMFs. For QE IMFs close to the projectile mass, the ratio decreased with increasing

kinetic energy, going to zero as the fragment velocity approached the beam velocity. However, for QE IMFs with about half the mass of the projectile, the ratio only slightly decreased with increasing velocity, and stayed above zero at velocities near the beam velocity. For DI IMFs, the measured ratios can be approximated with a constant functional dependence, but there is a need for data below the IMF kinetic energy threshold used here (6 MeV/nucleon) in order to draw any firm conclusions about the dependence. A constant functional dependence is consistent with emission from a thermal source.

The amount of feeding into bound states was measured for several neutron decay channels. The data is consistent with predictions of the feeding from a sequential decay model. Comparisons of the measured feeding and the predicted feeding from a sequential decay model indicate a source temperature between 2.5 and 4.0 MeV, which is consistent with the temperatures deduced from the analysis of two-level population ratios. The functional dependence of the amount of feeding on IMF kinetic energy was also investigated, and this dependence was used to estimate the correction to the ^{11}B inclusive spectra at 15° and 31°. Correcting for feeding raised the spectral temperature extracted from a moving-source analysis of the ^{11}B spectra from 11.2 MeV to 14.0 MeV

B. Conclusions

The ratios of neutron-unbound state populations to bound-state populations in DI IMFs are in general agreement with model calculations that assume a thermal mechanism for their production. Some of the DI population ratios are not fitted with the model calculations, however, which may suggest that other effects are present in the DI reaction mechanism that are not accounted for in the thermal, sequential decay model. The dependence of the ratio of an unbound-state population to its bound-state population on kinetic energy is consistent with emission from a thermal source, but additional data is needed to come to a definite conclusion. Correcting both the unbound-state populations and inclusive spectra for feeding does not resolve the discrepancy

between population temperatures derived from state populations and spectral temperatures derived from moving source analyses of singles spectra.

No clear difference can be seen between the two-level population ratios of DI and QE IMFs, where the data was sorted into relatively broad cuts on IMF kinetic energy. However, a difference between QE and DI IMFs can be seen in the dependence of the population ratios on narrower cuts on IMF kinetic energy. In addition, a difference in the dependence of the population ratio on kinetic energy is observed between half-beam mass and near-beam mass IMFs.

APPENDICIES

Appendix A

Effective Spin Factors

If a particular state in a fragment is populated according to a Boltzmann population distribution, then the population of that state can be written as:

$$P_i = \text{const} \times (2J_i+1) \times \exp(-E_i/T), \qquad \text{(A.1)}$$

where P_i is the population of a particular state with a level energy E_i and a spin J_i, const is a normalization constant, and T is the temperature of the source that is thermally emitting fragments. Rearranging the terms of Equation A.1 and taking the logarithm of both sides yields

$$\ln[P_i/(2J_i+1)] = \ln(\text{const}) - E_i/T \qquad \text{(A.2)}$$

If a nucleus has two or more states that are populated according to Equation A.1, and if the effects due to sequential feeding are neglected, then when one plotted the value of the lefthand side of Equation A.2 versus E_i, one would expect that every point plotted would lie on a straight line whose slope would be equal to -1/T. A problem occurs, however, if the measured population actually comes from a group of states instead of a single state. For example, the bound state population of ^{13}C contains the populations of the ground state ($J^{\pi} = 1/2^-$), the 3.09-MeV state ($J^{\pi} = 1/2^+$), the 3.68-MeV state ($J^{\pi} = 3/2^-$), and the 3.85-MeV state ($J^{\pi} = 5/2^+$). If the bound state population is to be plotted in the manner just described, then what are the values of E_i and $(2J_i+1)$ that are

to be used for this particular point? The answer may be seen by writing a more general form of Equation A.1 for a single population that comes from many levels.

$$P = \text{const} \times \sum_{i=1}^{n} (2J_i+1) \times \exp(-E_i/T) \qquad \text{(A.3)}$$

where n is the number of individual states, each with level energy E_i and spin J_i, that contribute to the total population P. Adding and subtracting the constant $E_\circ$ to E_i in Equation A.3 yields

$$P = \text{const} \times \sum_{i=1}^{n} (2J_i+1) \times \exp[(E_\circ - E_i - E_\circ)/T]$$

Rearranging the terms,

$$P = \text{const} \times \{\sum_{i=1}^{n} (2J_i+1) \times \exp[(E_\circ - E_i)/T]\} \times \exp(-E_\circ/T)$$

or,

$$P = \text{const} \times (2J_{eff}+1) \times \exp(-E_\circ/T) \qquad \text{(A.4)}$$

where $(2J_{eff}+1)$, called the "effective spin factor," is given by

$$(2J_{eff}+1) = \sum_{i=1}^{n} (2J_i+1) \times \exp[(E_\circ - E_i)/T] \qquad \text{(A.5)}$$

Now the value of the multilevel population P is given by an expression (Equation A.4) for the population from a single level with level energy $E_\circ$ and spin J_{eff} (compare with Equation A.1).

Of course the value of the effective spin factor will vary as a function of the temperature T and effective energy $E_\circ$, but it is possible to choose a value of $E_\circ$ that will minimize the range of values of $(2J_{eff}+1)$ over a particular range of T. Then $2J_{eff}+1$ will

be a function of only T if a Boltzmann population distribution is assumed for the four states. The advantage of choosing E_o in this way is that it reduces the uncertainty in the value of $\ln[P_i/(2J_{eff}+1)]$ (see Equations A.2 and A.4) due to the range of possible values of the effective spin factor.

Figure A.1 shows the value of the effective spin factor for the bound-state population of ^{13}C as a function of temperature for various values of E_o. If the effective spin factor is needed for a range of low temperatures, then a relatively low value of E_o is needed. For the purposes of this paper, the range of temperatures was taken to be 2 to 6 MeV. Table A.1 contains the maximum and minimum values of the effective spin factor in the range of 2 to 6 MeV for the multilevel populations measured here. The values of the effective spin factor shown in the table were calculated using the value of E_o that minimized the range of values of $(2J_{eff}+1)$ for each particular case. The value of the effective spin factor that was used for plotting the population of a "multilevel state" is simply the average of the minimum and maximum spin factors, and the uncertainty of the effective spin factor is one-half the difference between the maximum and minimum values.

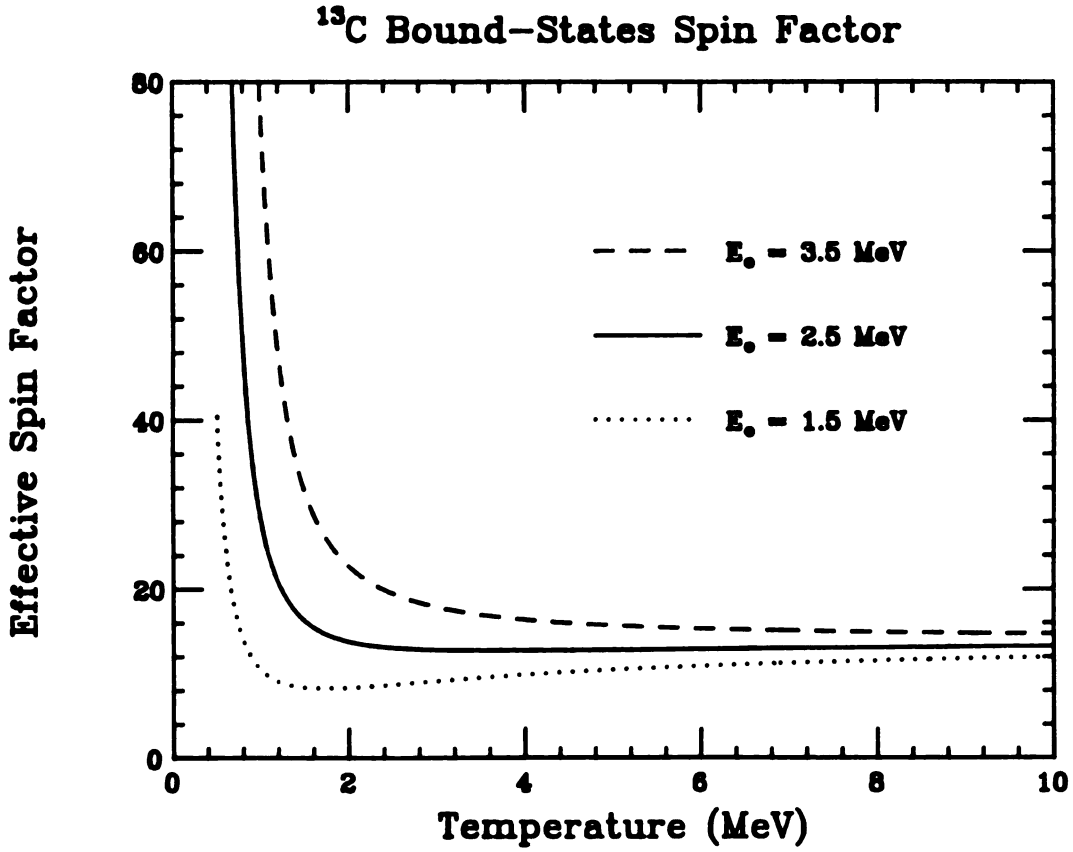

Figure A.1 - Values of the effective spin parameter for the bound states population in ^{13}C as a function of source temperature. Three sets of values are shown for different values of E_o (see Equation A.5), as indicated in the figure.

Table A.1 - Values for E_o and the minimum and maximum effective spin factors $(2J_{eff}+1)$ calculated for states whose measured population consists of populations from 2 or more individual levels. The level energy (in MeV) and spin is given for each individual state that is part of the "multilevel state."

Multilevel State	levels used		E_o	Min.	Max.
	energy	spin	(MeV)	$(2J_{eff}+1)$	$(2J_{eff}+1)$
^{13}C(bound)	g.s.	1/2	2.32	12.02	12.55
	3.089	1/2			
	3.685	3/2			
	3.854	5/2			
^{13}C(7.55)	7.492	7/2	7.55	17.98	17.99
	7.547	5/2			
	7.686	3/2			
^{12}B(bound)	g.s.	1	1.13	16.26	16.44
	0.953	2			
	1.674	2			
	2.621	1			
	2.723	0			
^{10}Be(bound)	g.s.	0	3.70	15.35	16.55
	3.368	2			
	5.958	2			
	5.960	1			
	6.179	0			
	6.263	2			
^{10}Be(7.44)	7.371	3	7.44	12.00	12.00
	7.542	2			
^{10}Be(9.31)	9.27	4	9.32	14.01	14.03
	9.4	2			

Appendix B

Determination of Level Energies and Widths

The measurement of level energies and widths in intermediate-mass fragments (IMFs) has been, and still is, a topic of great interest in the nuclear physics community. A number of experimental techniques (Kull67, Ooth77, Ajze76, Youn71, Ajze78) have been developed over the years that measure these state parameters. Some of the methods are only applicable to particle-unbound states, while others can be applied to both particle-bound and particle-unbound states. All of the methods share a common trait in that they produce a two-body final state, which allows the energy and width to be determined by measuring the kinetic energy and yield of just one reaction product.

A great variety of both particle-bound and particle-unbound states in IMFs is created in intermediate-energy heavy-ion collisions, providing the experimenter a source of excited states to measure and study. However, many of the previous techniques used to measure the level energy and width are not applicable to nuclei created in heavy-ion reactions, since in general heavy-ion reactions result in a *many*-body final state. A method which is applicable is the method of sequential-decay spectroscopy, in which the two-body decay of an unbound state is detected by observing both decay products.

Using the neutron-IMF coincidence data reported on in this thesis, it is possible to measure the energy and width of a level in ^{8}Be and of a level in ^{9}Li with a precision comparable to previous measurements of the widths and energies of these levels. The method used here to measure the level energy and width is an adaptation of the method

of sequential neutron-decay spectroscopy, which separates one excited state of one nucleus from all other states produced in the collision by using a coincidence technique that gives the momenta of the neutron and the daughter nucleus. The vector difference of those momenta determines the decay energy, which is independent of the laboratory kinetic energy of the parent nucleus. This technique has been adapted to include only the coincidence data from colinear neutron-fragment detection systems.

By using colinear detector systems, one can take advantage of the kinematical focussing of the decay neutrons into the neutron detectors. The kinematical focussing greatly increases the counting rate, since much of the neutron flux from the decay of an excited IMF is swept along with the IMF. To give an idea of how much the counting rate is increased, consider the following case of detecting neutrons that come from the decay of the 19.24-MeV state in ^{8}Be, using the colinear detector system at 15°. In total, the three neutron detectors at 15° subtend only 0.17% of the 4π stereradians in which a neutron can be emitted. However, if a neutron is emitted from the decay of the 19.24-MeV state of an excited ^{8}Be nucleus, and if the excited ^{8}Be nucleus is traveling towards the 15° detector with an energy between 6 and 35 MeV/nucleon, then approximately 2.4% of such neutrons will be focussed into the 15° neutron-detector array. Thus the counting rate increases by a factor of about 14 due to the kinematical focussing.

The level energy and width for two states have been deduced from the analysis of relative <u>energy</u> spectra, such as the ones in Figures B.1 and B.2. Figure B.1 shows the relative energy spectrum for ^{7}Be + n at 15°, and Figure B.2 shows the relative energy spectrum for ^{8}Li + n at 15°. Relative energy is defined as the following:

$$E_{rel} \approx \frac{1}{2}\mu v_{rel}^{2},$$

where

$$v_{rel} = v_{daugh} - v_{n}$$

and

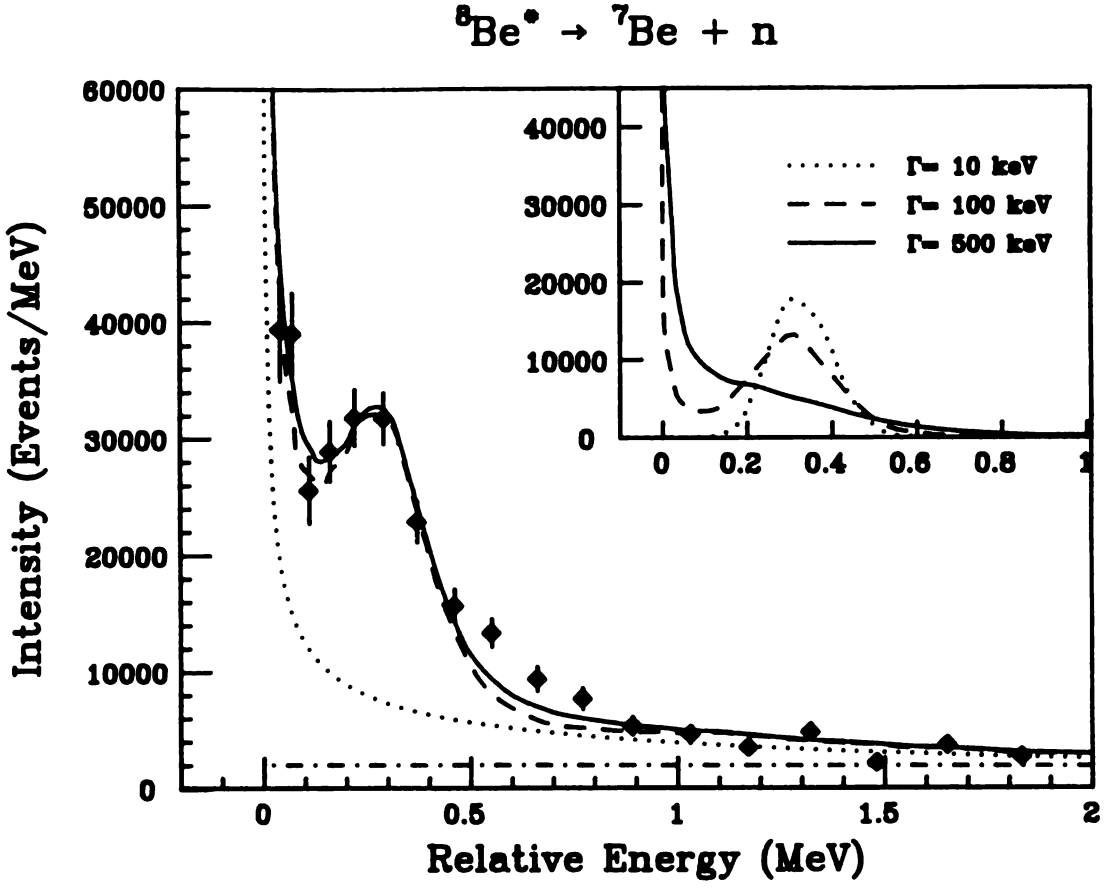

Figure B.1 - Relative energy spectrum for ^{7}Be + neutron at 15°. The dashed line shows the fit using the background indicated with the dot-dashed line, while the solid line shows the fit to the data using the background indicated with the dotted line. The peak at 0.28 MeV comes from the decay of the 19.24-MeV state ($\Gamma \approx 200$ keV) in ^{8}Be. Inserted in the upper right-hand corner is a simulation of the decay of the 19.24-MeV state for Γ = 10 keV (dotted line), Γ = 100 keV (dashed line), and Γ = 500 keV (solid line). There is no background included in the simulations.

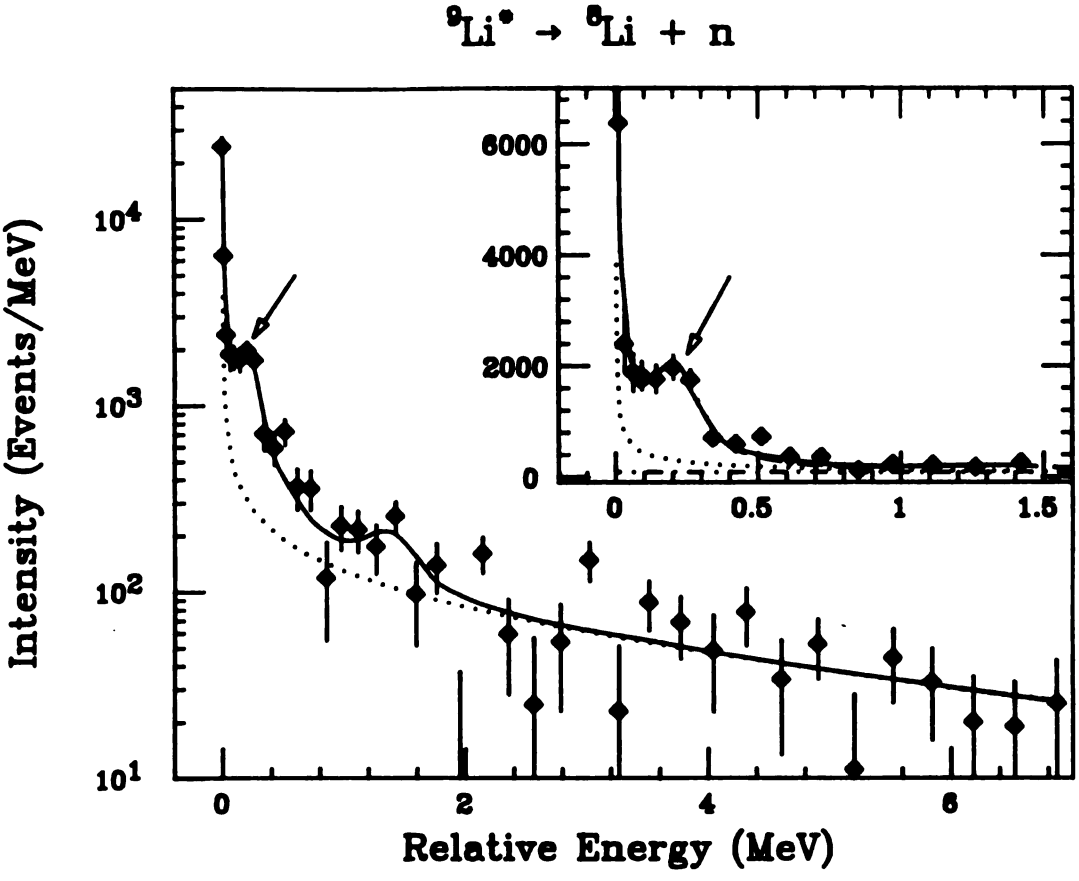

Figure B.2 - Relative energy spectrum for ^{8}Li + neutron at 15°. The solid line shows the fit to the data, and the dotted line shows the background used in the fitting. The peak at 200 keV (indicated by the arrow) is from the decay of the 4.31-MeV state in ^{9}Li to the ground state of ^{8}Li. Shown in the upper right-hand corner is an expanded view of the region of interest.

$$\mu = (m_{daugh} m_n)/(m_{daugh} + m_n).$$

The peak at 0.28 MeV in Figure B.1 is from the decay of the 19.24-MeV state in ^{8}Be, and the peak at 0.2 MeV in Figure B.2 (shown by the arrow) is from the decay of the 4.3-MeV state in ^{7}Li. Inserted in the upper right of Figure B.2 is an expanded view of the region of interest.

The solid and dashed lines in Figures B.1 and B.2 are fits to the spectra using Monte Carlo simulations of the decay into the detection system, added on top of a background represented by the dotted and dot-dashed lines. In Figure B.1, the dotted line was the background used for the fit represented by the solid line, and the dot-dashed line shows the background used for the dashed-line fit. The Monte Carlo simulations were calculated by the code MONTRES, which has been described in the main body of this thesis. The fitting was done by producing a number of simulations for various combinations of level energy and width, holding all other input parameters in the code fixed. These simulations were then used to make a X^2 fit that gridded on the two parameters that were varied.

Inserted in the upper right of Figure B.1 are three simulations of the decay of a 19.24-MeV state in ^{8}Be using values of 10 keV, 100 keV, and 500 keV for the level width. There is no background shown with these simulations. As the level width increases from 10 to 500 keV, not only does the peak shape change, but the spectral shape between 0 and 0.2 MeV also changes. The fact that the number of events in the region between 0 and 0.2 MeV increases as the width increases is an interesting consequence of the kinematical focussing and the size of the width compared to the decay energy, which is about 340 keV. When the width is comparable to the decay energy it is possible to have a decay with an energy significantly lower than 340 keV, although the probability of getting lower, off-resonance energies decreases with energy. However, as the decay energy decreases, the kinematical focussing increases rapidly. It is these two effects

together which conspire to give the spectrum its unique shape between 0 and 0.2 MeV for the larger values of the width.

The widths used for both of the states analyzed here are constants in a Lorentzian resonance function that represents the decay of these states. As it turns out, in both cases the level widths are close enough to the decay energies that it would be prefered to use an energy dependent width in the Lorentzian resonance function. However, an energy dependent width cannot be used for either case. In the case of the 19.24-MeV state in ^{8}Be, there are other decay branches (p and α). The branching ratios for the decays of this state are not known, hence the energy dependent width cannot be deduced, since the partial neutron width is not known. In the case of ^{9}Li, the spin of the 4.3-MeV state is not known, which makes it impossible to calculate neutron penetrabilities for the decay from this state.

Since the precise nature of the background in relative energy spectra is unknown, two different backgrounds were used during the analysis to estimate the uncertainty in the extracted level parameters due to background determination. One of the backgrounds used is a Gaussian in relative velocity space transformed to relative energy space. This type of background is shown by the dotted lines in Figures B.1 and B.2. The other type of background used is essentially a flat background, and it is shown as the dot-dashed line in Figure B.1 and in the insert in Figure B.2. Although these two backgrounds are similar in the high-energy tails of the spectra, they differ a great deal in the low-energy end, which is the region where the fitting is most sensitive. For both of the levels reported on here, the energy and width determined with one background are well within uncertainties of the values obtained with the other background.

Table B.1 contains the energies and widths determined from the best fits to the data for the 19.24-MeV state in ^{8}Be and the 4.3-MeV state in ^{9}Li. Once the best values were found for each type of background, the errors in those values were determined by the following method. A contour plot of the χ^2 values versus decay energy and Γ was

Table B.1 - Level Energies and Widths

Isotope	Level Energy (MeV)	Decay Energy (keV)	Width (keV)	Reference
^{9}Be	19.23(12)	336	210(35)	This work
	19.21	312	208(30)	Kull67
	19.26(30)	362	220(30)	Ooth77
	19.22(30)	322	265(30)	Ajze76
^{9}Li	4.30(15)	233	60(45)	This work
	4.31(30)	247	250(30)	Youn71
	4.31(20)	247	100(30)	Ajze78

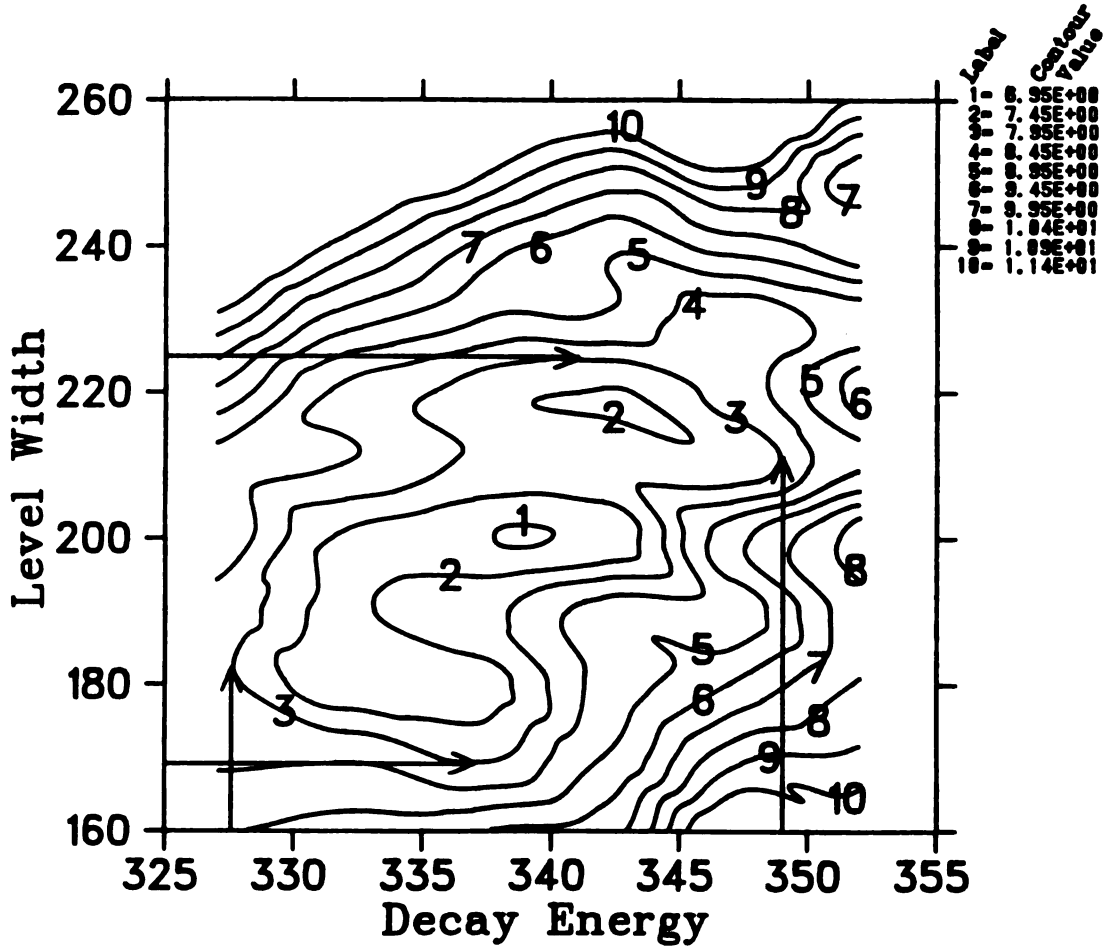

Figure B.3 - Contour plot of the X^2 space gridded on decay energy and level width for ^{7}Be + neutron at 15°, using a Gaussian background. The minimum contoured value is 6.95, and each succeeding contour represents an increase of 0.5 in the total X^2. A legend is included in the upper right of the plot. The arrows indicate the maximum and minimum values of the decay energy and Γ on the contour labeled with a "3", which is for X^2 = 7.95.

made. Figure B.3 shows such a plot for ^{8}Be at 15° using a Gaussian background. The minimum total X^2 is 6.95, and it corresponds to a decay energy of 338 keV and a level width of 200 keV. The contour that represents this value of the total X^2 is labeled with a "1". Each succeeding contour corresponds to an increase of 0.5 to the total X^2. Thus the contour labeled "3" corresponds to a total X^2 of 7.95. A legend is included in the upper right of the plot. The maximum and minimum values for the decay energy and width on the contour that represents the value of $X^2 + 1$, namely 7.95, are taken to be the upper and lower limits on the uncertainties for those parameters. In Figure B.3 the upper and lower limits for the uncertainty of the decay energy are 328 and 349 keV, and the upper and lower limits for the uncertainty of the width are 170 and 225 keV. These limits are indicated with arrows in the figure.

Note that there is some correlation between the decay energy and Γ. If these two parameters were uncorrelated, then the upper and lower limits on the uncertainty of the decay energy would lie on a line of constant energy, and the limits on the uncertainty of the width would lie on a line of constant Γ. This is clearly not the case in Figure B.3. The contour plots for all other isotope-background combinations showed some correlation between Γ and the decay energy.

In the case of the 19.24-MeV state in ^{8}Be, data was obtained at both 15° and 31°. The values and uncertainties reported in Table B.1 for the energy and width of this state are the weighted values and uncertainties from those two angles. No data was obtained at 31° for the 4.3-MeV state in ^{9}Li because of the poor statistical quality. The uncertainties reported in Table B.1 from this measurement also include the effect of an assumed misalignment from colinearity of the detectors by 0.5°, and an assumed flight-path error (1 - 3 cm) that would produce a shift of 0.25 mm/ns in relative velocity. These systematic errors contributed little to the total uncertainty.

Included in Table B.1 are the values for the energies and widths of the 19.24-MeV state in ^{8}Be and the 4.3-MeV state in ^{9}Li from Kull67, Ooth77, Ajze76, Youn71, and

Ajze78. In all of the measurements, the energy and width were determined from either an excitation function of the light particle emitted from a two-body final state or from a spectrum of the light particle. Both the energy and width determined from the analysis reported here for both of these states are within the uncertainties of the previous measurements, except for the width of the 4.3-MeV state in ^{9}Li. The width reported here is lower than either of the previously reported values, although it is consistent (within uncertainties) with the value reported in Ajze78.

When compared to the other results in Table B.1, the accuracy and precision of the method described here that was used to determine the energies and widths of the two reported states indicate this method can be a useful technique when applied to heavy-ion collisions. It should be noted that the experiment was not designed for the purpose of measuring state energies and widths (the main purpose was to measure the populations of those states), so it is conceivable that the technique could be improved. For example, one could simply lengthen the flight paths or reduce the angular acceptance of the fragment detector. It should also be noted that the technique described here is best used for states where the decay energy is small, so some modifications would be necessary if one wanted to achieve the same precision for states of higher decay energy.

Appendix C

8Be Contamination in 7Li Spectra

The fact that ^{7}Li spectra measured with solid-state detectors also contain events from the double-alpha breakup of ^{8}Be has been known and reported on for several years (Wozn72, Bloc86). The reason why this contamination of ^{7}Li spectra is present can be shown by the following: Suppose a ^{8}Be and a ^{7}Li have the same energy,

$$E_{^{7}Li} = E_{^{8}Be}$$

Since the flight times in this experiment for a ^{8}Be to reach the detection system from the target varied between 2 and 8 nsec, and since the lifetime of the ground state of ^{8}Be is on the order of 10^{-16} seconds, all of the ground state ^{8}Be breaks up into two α particles before reaching the detection system. Each α will have approximately one-half of the total energy of the ^{8}Be.

$$E_{\alpha} = 0.5 \times E_{^{8}Be}$$

The magnitude of the ΔE signal for a ^{7}Li can be found using the Bethe-Bloch formula for energy loss in a material, which can be written simply as (neglecting constants and logarithmic factors):

$$\Delta E/\Delta x = mZ^{2}/E,$$

where Δx is the thickness of the material, m is the mass of the particle losing energy, Z is the charge of the particle, and E is the kinetic energy of the particle. Using 7 for the mass of ^{7}Li and Z = 3, the energy loss for ^{7}Li is given by

$$\Delta E/\Delta x)_{^{7}Li} = 63/E_{^{7}Li}. \qquad (C.1)$$

Similarly, the energy loss for an α particle is given by

$$\Delta E/\Delta x)_{\alpha} = 16/E_{\alpha}.$$

If both alphas from the breakup of a ^{8}Be are collected by the detection system, the energy loss in the detector from this erstwhile ^{8}Be particle is

$$\Delta E/\Delta x)_{^{8}Be} = 2\times\Delta E/\Delta x)_{\alpha} = 32/E_{\alpha},$$

and since each α has half of the ^{8}Be energy, the energy loss can be written as

$$\Delta E/\Delta x)_{^{8}Be} = 64/E_{^{8}Be}. \qquad (C.2)$$

If the ^{8}Be and the ^{7}Li particles have the same energy (hence they lie at the same point on the E axis on a ΔE - E plot), Equation C.2 can be written as

$$\Delta E/\Delta x)_{^{8}Be} = 64/E_{^{7}Li} \qquad (C.3)$$

Comparing Equations C.1 and C.3, it is seen that for the same total kinetic energy E, the ΔE signals from these two types of particles differ by 1 part in 64, or about 1.6%. This percentage is smaller than the straggling due to electron-hole production and charge collection in the silicon detectors that were used (which is about 5%, on the average), thus it is not possible to resolve these two different types of particles from each other. Note that this contamination will be present in all ^{7}Li spectra that are measured with detection systems that provide isotope identification with ΔE versus E plots.

If the ^{8}Be spectrum is known, and if the probability for collecting both alphas from the breakup is known, this contamination can be subtracted from the ^{7}Li + ^{8}Be spectrum. The probability of collecting both alphas is a function of the parent ^{8}Be kinetic energy and detector geometry, and it can be calculated using a Monte Carlo simulation. Of course, there is no direct way of measuring a ^{8}Be spectrum, but it can be determined using a technique reported in Bloc86. In this technique the ^{7}Li + ^{8}Be spectrum is measured at the same angle, but for two different solid angles. Once the probability of collecting both alphas (also referred to as the collection efficiency) is

calculated for each solid angle, either the true ^{7}Li spectrum or the ^{8}Be spectrum can be estimated from the following two relations:

$$Y_{tot}(\Omega_1) = Y_{Li}(\Omega_1) + \varepsilon_1 \times Y_{Be}(\Omega_1) \qquad (C.4)$$

$$Y_{tot}(\Omega_2) = Y_{Li}(\Omega_2) + \varepsilon_2 \times Y_{Be}(\Omega_2) \qquad (C.5)$$

where Y_{tot} refers to the measured ^{7}Li + ^{8}Be yield at a particular energy, Y_{Li} refers to the ^{7}Li yield, Y_{Be} refers to the ^{8}Be yield, ε refers to the collection efficiency, and the subscripts 1 and 2 refer to the two solid angles used. Since both Y_{tot} are measured and both ε are calculated, Equations C.4 and C.5 are two equations with only two unknowns, and both Y_{Li} and Y_{Be} can be determined from those equations.

Although the ^{8}Be spectrum was not measured in this experiment, another group (Bloc86) has measured the ^{8}Be spectrum at 50° for the same system as the one here, namely ^{14}N + Ag at 35 MeV/nucleon. In the analysis reported in Bloc86, the ^{8}Be spectrum is assumed to have the same spectral shape as the ^{8}Be spectrum. The ratio of the energy-integrated ^{8}Be yield to the energy-integrated ^{8}Be yield is also calculated in Bloc86, and they report a value of ^{8}Be/^{8}Be of 2.1 ± 0.5. Since the work reported in Bloc86 is for the same system as ours, and since they measured ^{8}Be at an angle where deep-inelastic reactions dominate, it is assumed that the same value of ^{8}Be/^{8}Be is true at 31° and 64°, and that the ^{8}Be spectrum has the same spectral shape as the ^{8}Be spectrum. Thus, the ^{8}Be spectra at 31° and 64° are taken to be 2.1 times the measured ^{8}Be spectra at those angles. (In addition to the ^{8}Be spectrum, the collection efficiency also had to be calculated in order to correct the ^{7}Li + ^{8}Be spectrum. The calculation of the collection efficiency will be discussed below). The measured ^{7}Li + ^{8}Be spectra and the corrected, true ^{7}Li spectra at 31° and 64° are shown in Figure C.1. The corrected spectra are shown with the solid symbols.

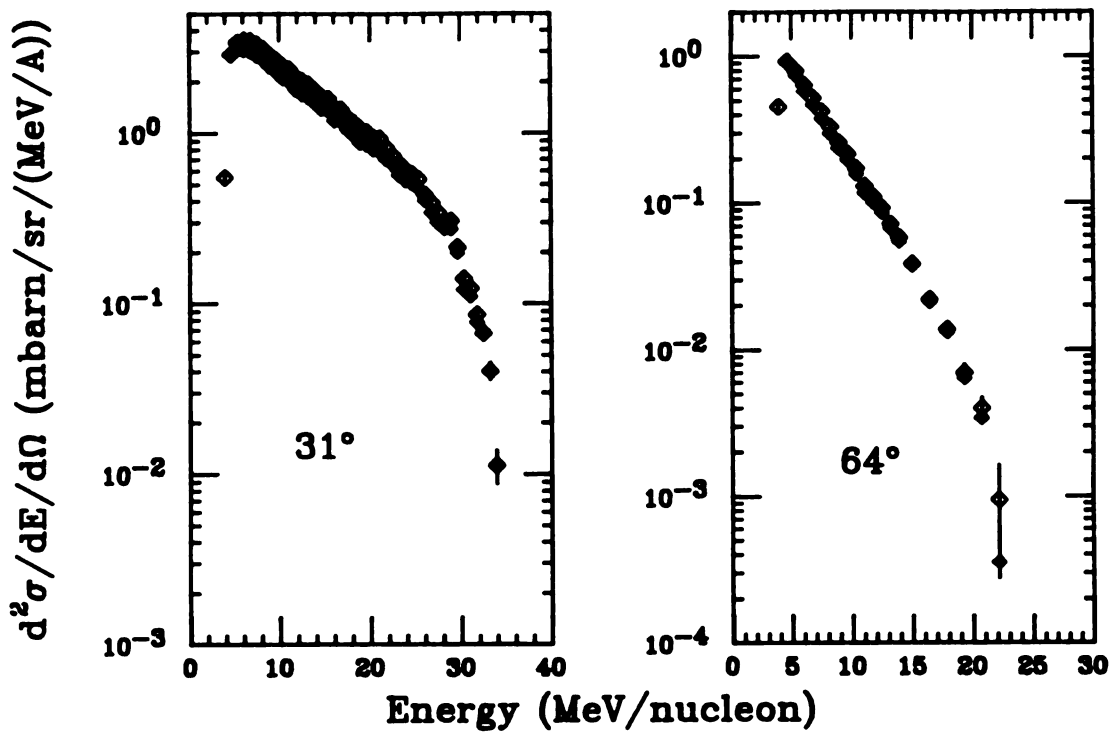

Figure C.1 - ^{7}Li singles spectra at 31° and 64°. The open symbols indicate the spectra before correcting for ^{8}Be contamination, and the closed symbols show the spectra after the correction.

Since the ^{8}Be spectrum measured by Bloc86 is in a region where deep-inelastic processes dominate, the procedure used to correct the spectra at 31° and 64° was not used to correct the ^{7}Li spectrum at 15°, where there is a strong contribution from quasielastic processes. Quasielastic ^{8}Be has not been measured for this system, so the ^{8}Be spectrum at 15° was estimated from an interpolation of the ^{7}Be, ^{9}Be, and ^{10}Be spectra at 15° at specific values of E/A. Figure C.2 shows the interpolated ^{8}Be spectrum at 15°, along with the spectra for ^{7}Be, ^{9}Be, and ^{10}Be. The interpolated spectrum was then used to correct the ^{7}Li + ^{8}Be spectrum at 15°.

In addition to the ^{8}Be spectrum, the collection efficiency for the detection system is also needed in order to correct the measured ^{7}Li + ^{8}Be spectra at 15°, 31°, and 64°. The collection efficiency was calculated using a Monte Carlo simulation of the decay of the parent ^{8}Be and the subsequent kinematical focussing of the two alpha particles towards the detector. The code assumes an isotropic emission of the alphas, with the constraint that the alphas are emitted 180° with respect to each other in the center-of-mass frame. Once the decay has occurred, the paths of both alphas are followed to see if both are collected in the detector. The code then keeps track of the percentage of decays from a ^{8}Be of a specific energy that result in both alphas being detected. Figure C.3 shows the collection efficiency as a function of ^{8}Be kinetic energy for the detectors at 15° (solid line) and at 31° and 64° (dashed line). The solid angle subtended by the 15° detector was 3.54 msr, and the solid angle subtended by both the 31° and 64° detectors was 8.10 msr.

Once the ^{8}Be spectra and collection efficiencies at 15°, 31° and 64° were in hand, the measured ^{7}Li + ^{8}Be spectra were corrected on a point-by-point basis, as follows. For a particular energy, the value of the ^{8}Be spectrum at that energy was multiplied by its corresponding collection efficiency, and that result was then subtracted from the value of the ^{7}Li + ^{8}Be spectrum. The final result was the value of the "true" ^{7}Li spectrum for

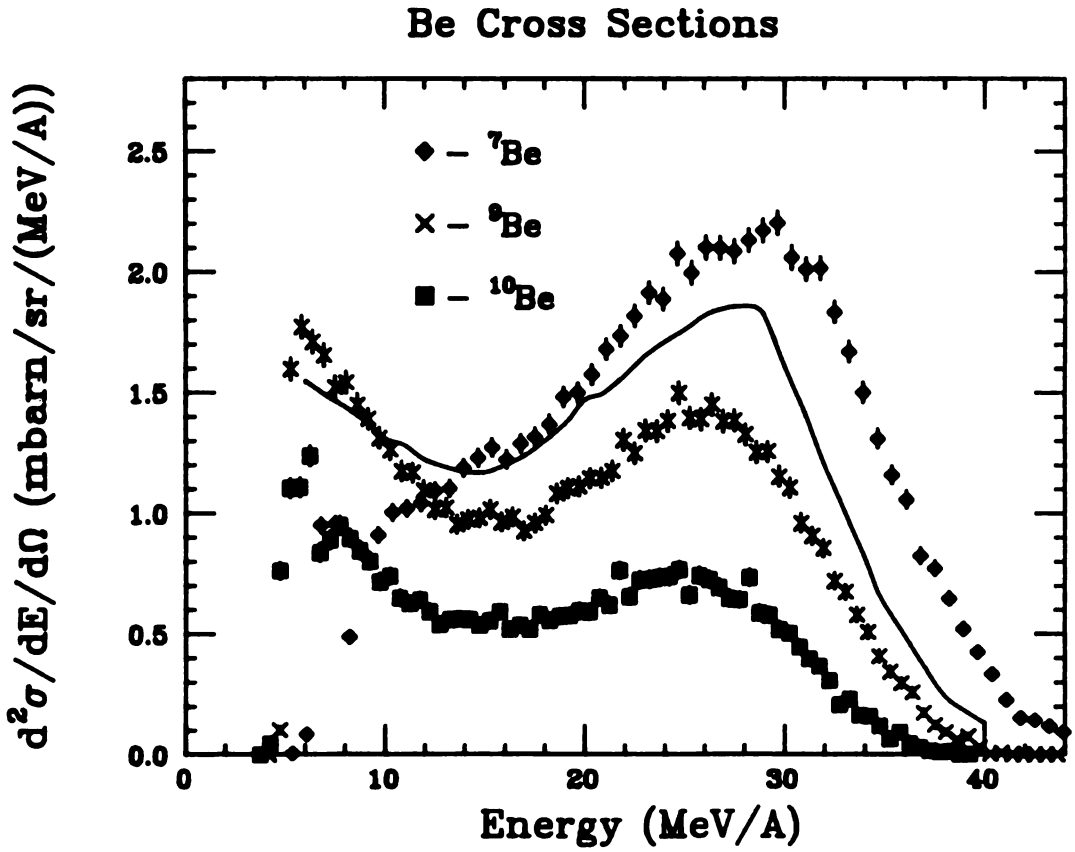

Figure C.2 - Singles spectra for ^{7}Be, ^{9}Be, ^{9}Be, and ^{10}Be at 15°. The symbols used for the ^{7}Be, ^{9}Be, and ^{10}Be spectra are indicated in the figure. The line indicates the ^{9}Be spectrum, which was interpolated from its neighboring ^{7}Be, ^{9}Be, and ^{10}Be singles spectra.

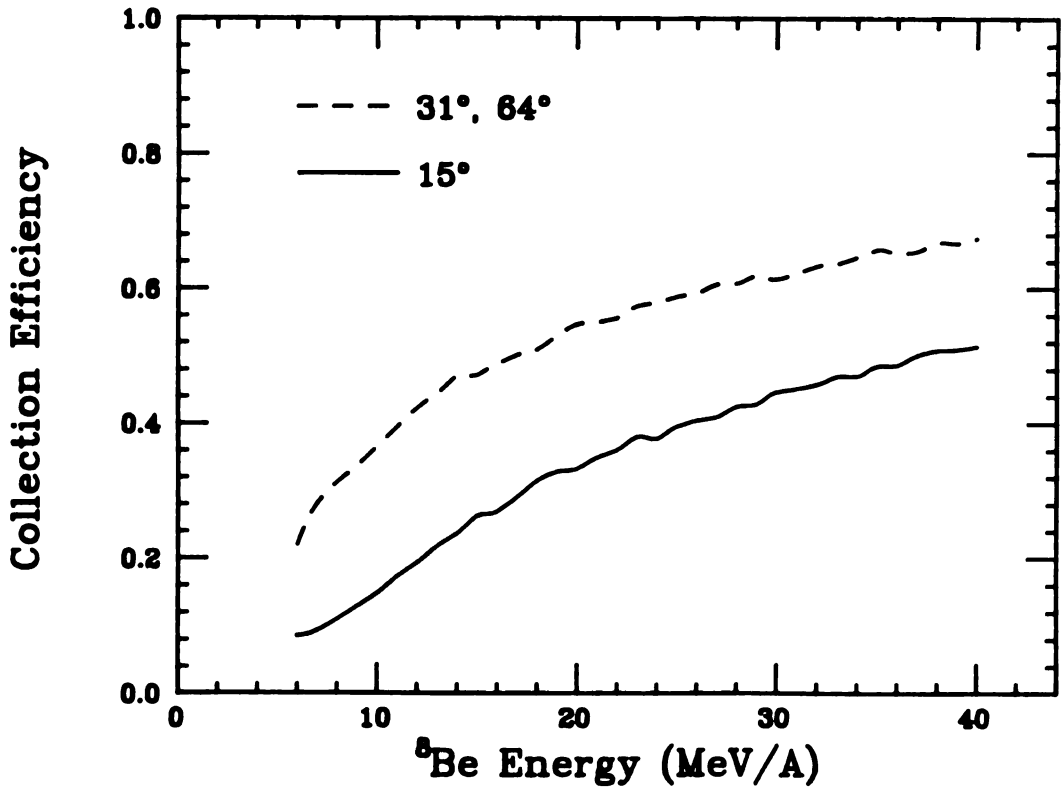

Figure C.3 - The collection efficiency for detecting both alpha particles from the breakup of ^{8}Be in the silicon telescopes at 15°, 31° and 64°. Note that the same efficiency curve is used for 31° and 64° since the detector solid angles were the same at these two angles. The efficiencies were calculated using a Monte Carlo simulation.

that energy. Figure C.4 shows the measured $^{7}Li + {}^{9}Be$ spectrum and the corrected spectrum (shown with the solid symbols) at 15°.

The effect of the correction on the integrated cross sections at 15°, 31°, and 64° shows how large the contamination is at each of these angles. At 15°, the integrated cross section was reduced by 9% after the correction, and at 31° and 64° the integrated cross sections were reduced by 15% and 9%, respectively. In all three cases, the overall correction is not very large in terms of its effect on the integrated cross sections, but it is large enough to justify the effort to apply the correction to the data.

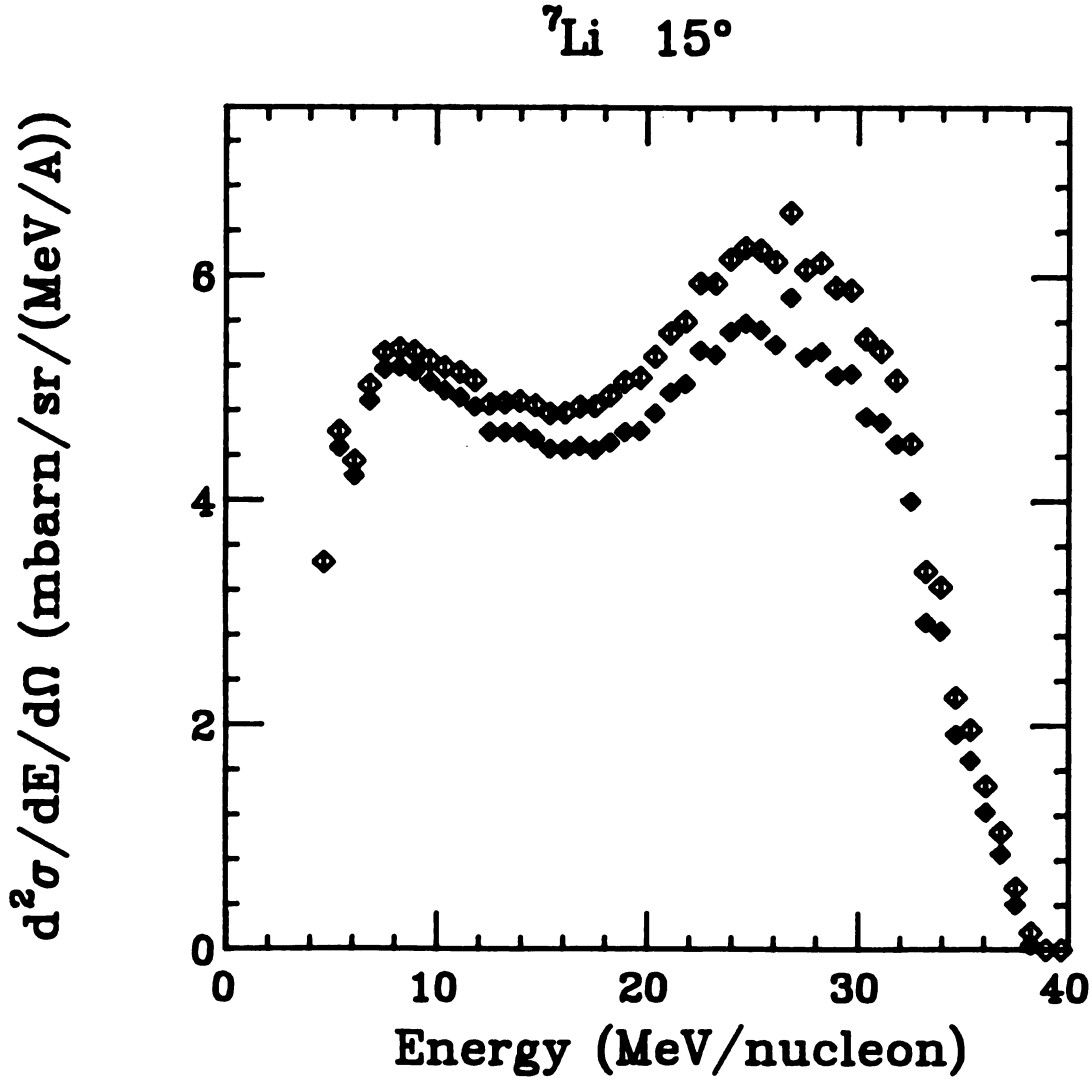

Figure C.4 - ^{7}Li singles spectrum at 15°. The open symbols show the spectrum before correcting for ^{8}Be contamination, and the closed symbols show the spectrum after the correction.

Appendix D

Width Calculation using Penetrabilities

The probability that a particular nuclear state decays through a specific channel (designated by β) with a channel energy E is given by (Blat52):

$$P(E) \propto (1/4\pi)(2\ell+1)\lambda_\beta^2 \frac{\Gamma_\beta \Gamma_{tot}}{(E-E_{res})^2 + (0.5\Gamma_{tot})^2}, \qquad (D.1)$$

where Γ_β is the width of the decay channel β, Γ_{tot} is the sum of all of the possible decay channel widths, E_{res} is the resonance energy for the particular decay channel β, λ_β is the de Broglie wavelength of the channel β ($\lambda_\beta/2\pi = k_\beta^{-1}$, where $k_\beta = (2\pi/h)\sqrt{2ME}$), and ℓ is the angular momentum of the channel. The expression in Equation D.1 was used in the Monte Carlo code Montres (see Chapter III of this thesis) to determine the energy available to the neutron and daughter fragment that came from the neutron decay of a particular parent state. This energy was then used to calculate the relative velocity between the neutron and daughter fragment. Montres calculated one million events for each particular decay, and for each event the relative energy between the neutron and daughter was determined using Equation D.1. Thus, one can see that because of the widths Γ_β and Γ_{tot}, a distribution of relative velocities is obtained from the one million events, even if all other effects which affect the relative-velocity resolution are neglected.

In general, Γ_β can be written as the following (Blat52):

$$\Gamma_\beta = (2k_\beta R v_\ell)\gamma_\beta^2, \qquad (D.2)$$

where R is the channel radius (equal to the sum of both particles' radii for a two-body decay), v_ℓ is the penetration factor for the channel β that has an angular momentum ℓ, and γ_β^2 is the reduced width for channel β. The first factor in Equation D.2 ($2k_\beta Rv_\ell$) is a function of the channel energy and depends on conditions outside the nucleus. The reduced width γ_β^2 incorporates all of the properties of the interior of the nucleus.

In every case except one, Γ_n and Γ_{tot} were taken to be constant as a function of channel energy when they were used in the code Montres. The one exception was for the decay of the 7.456-MeV ($J^\pi = 5/2^-$, Γ = 89 keV) state in ^{7}Li to the ground state of ^{6}Li ($J^\pi = 1^+$) plus a neutron. Since the reported width (89 keV) is relatively large when compared to the resonance decay energy (209 keV), there is a non-zero probability for a decay with a very low decay energy. This point is illustrated with the solid line in Figure D.1, which shows the value of P(E) (Equation D.1) as a function of E, using constant values of Γ_n and Γ_{tot} (for this calculation, Γ_n= 68 keV, Γ_α= 21 keV, and Γ_{tot}= 89 keV).

In order to conserve angular momentum and parity in the neutron decay of the 7.456-MeV state in ^{7}Li, the decay channel must carry an angular momentum of either ℓ=1 or ℓ=3. Since the channel has a non-zero angular momentum, there is a centrifugal barrier the neutron must penetrate in order to decay, and the probability that the neutron penetrates the barrier depends on the energy of the neutron. As the decay energy available to the neutron becomes less and less, the probability for barrier penetration gets smaller. Thus when the effects of the centrifugal barrier are taken into account, the probability for a decay with a near-zero decay energy is reduced.

The effect of the centrifugal barrier is taken into account with the penetration fractor v_ℓ of Equation D.2. When this is done, the neutron width Γ_n is no longer constant as a function of energy. The values of v_ℓ for ℓ = 1 were obtained from Mona58 for

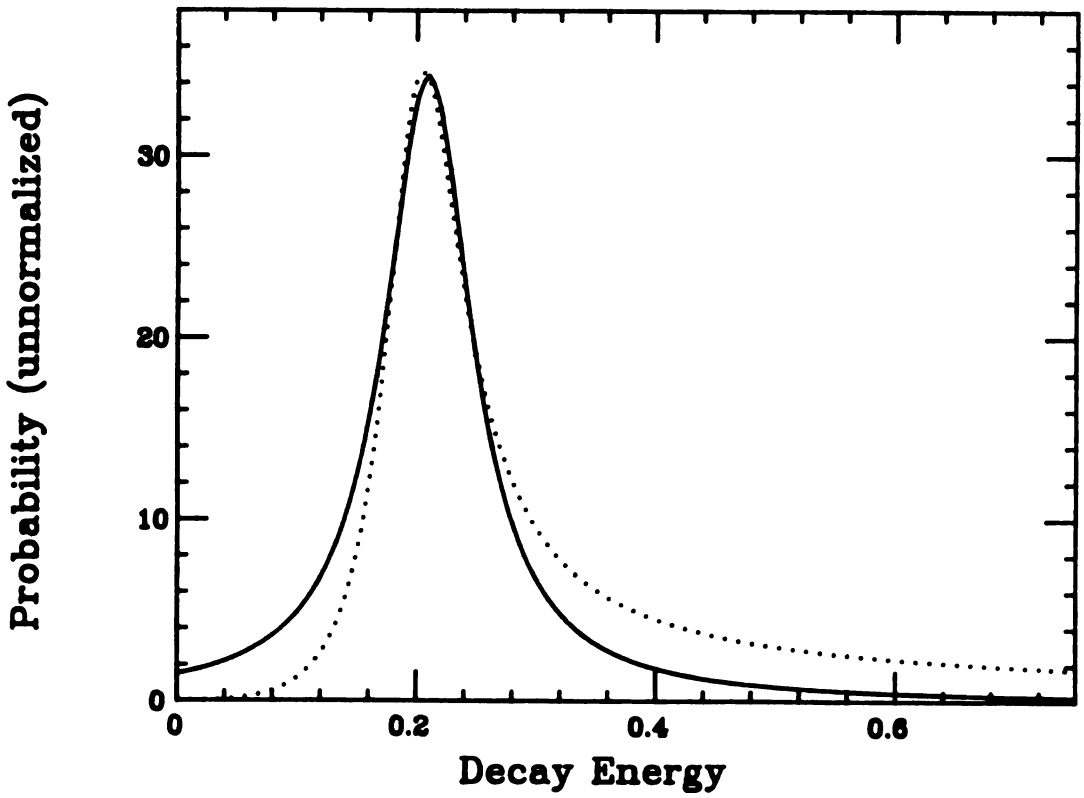

Figure D.1 - Decay probability as a function of energy, as calculated with Equation D.1. The solid line is for the calculation using constant widths, and the dotted line shows the calculation using an energy dependent width.

neutron energies ranging from 0 keV to 750 keV, and these values were used to calculate the energy dependent neutron width $\Gamma_n(E)$. Using the calculated values of $\Gamma_n(E)$, P(E) from Equation D.1 was calculated. The calculated values of P(E) (Equation D.1) using the energy dependent values of $\Gamma_n(E)$ are shown with the dotted line in Figure D.1. Note in Figure D.1 that the probability for a low-energy decay calculated with an energy dependent width (dotted line) is lower than the probability for a low-energy decay calculated with a constant width (solid line).

Figure D.2 shows the fits to the ^{6}Li + n relative velocity spectrum at 15° with a Monte Carlo simulation of the neutron decay of the 7.456-MeV state in ^{7}Li (added on top of a background) using a constant width (top plot) and an energy-dependent with (lower plot). The X^2/d.o.f. for the fit in the upper plot is 2.1, and the X^2/d.o.f. for the fit in the lower plot is 1.2. Clearly, the ^{6}Li + n relative velocity spectrum is fitted much better when an energy-dependent width is used in the Monte Carlo simulation.

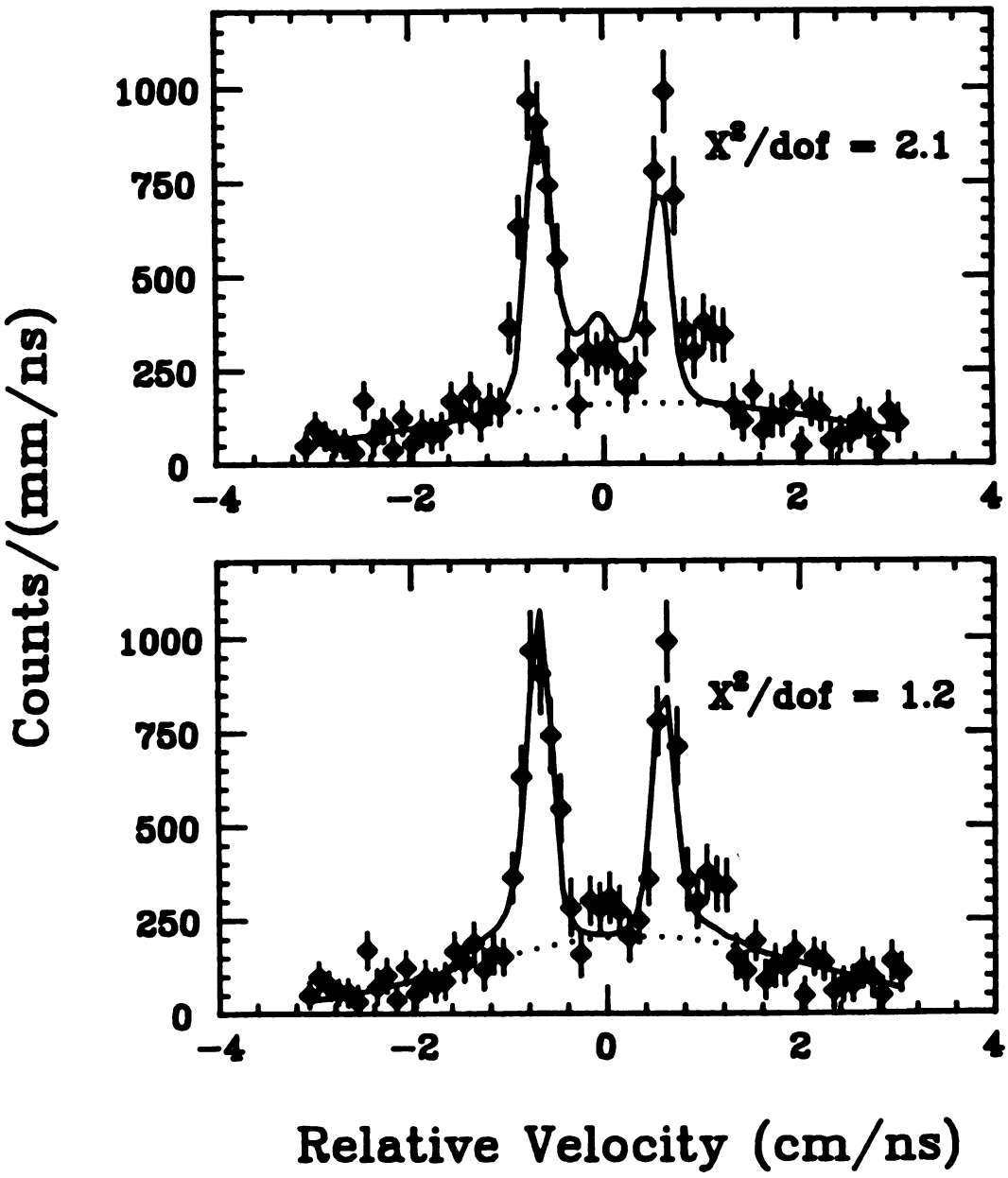

Figure D.2 - Both plots show fits to the ^{6}Li + n relative velocity spectrum for ^{6}Li kinetic energies between 25 MeV/A and 30 MeV/A and for $\Theta = 15°$. The fitting in both cases was done using a Monte Carlo simulation of the decay of the 7.456-MeV state in ^{7}Li to the ground state of ^{6}Li added on top of a background (the dotted line shows the background used). The fit in the top plot used a constant width in the Monte Carlo simulation, and the fit in the bottom plot used an energy-dependent width in the simulation.

LIST OF REFERENCES

LIST OF REFERENCES

Ajze76 F. Ajzenberg-Selove, C. F. Maguire, D. L. Hendrie, D. K. Scott, and J. Maloney, Phys. Rev. C **13**, 46 (1976)

Ajze78 F. Ajzenberg-Selove, E. R. Flynn, and O. Hansen, Phys. Rev. C **17**, 1283 (1978)

Ajze84 F. Ajzenberg-Selove, Nucl. Phys. **A413**, 1 (1984)

Ajze86 F. Ajzenberg-Selove, Nucl. Phys. **A449**, 1 (1986)

Ajze90 F. Ajzenberg-Selove, Nucl. Phys. **A506**, 1 (1990)

Blat52 J. M. Blatt and V. F. Weisskopf, "Theoretical Nuclear Physics", John Wiley and Sons, New York (1952)

Bloc86 C. Bloch, W. Benenson, E. Kashy, D. J. Morrissey, R. A. Blue, R. M. Ronningen, and H. Utsunomiya, Phys. Rev. C **34**, 850 (1986)

Bloc87 C. Bloch, W. Benenson, A.I. Galonsky, E. Kashy, J. Heltsley, L. Heilbronn, M. Lowe, B. Remington, D.J. Morrissey and J. Kasagi, Phys. Rev. C **36**, 203 (1987)

Bloc88 C. Bloch, W. Benenson, A.I. Galonsky, E. Kashy, J. Heltsley, L. Heilbronn, M. Lowe, R.J. Radtke, B. Remington, J. Kasagi, and D.J. Morrissey, Phys. Rev. C **37**, 2469 (1988)

Blum86 Y. Blumenfeld, Ph. Chomaz, N. Frascaria, J.P. Garron, J.C. Jacmart, J.C. Roynette, D. Ardouin, and W. Mittig, Nucl. Phys. **A455**, 357 (1986)

Boal84 D. Boal, Phys. Rev. C **30**, 749 (1984)

Cask88 G. Caskey, L. Heilbronn, B. Remington, A. Galonsky, F. Deak, A. Kiss, and Z. Seres, Phys. Rev. C **37**, 969 (1988)

Cebr89 D.A. Cebra, W. Benenson, Y. Chen, E. Kashy, A. Pradhan, A. Vander Molen, G.D. Westfall, W.K. Wilson, D.J. Morrissey, R.S. Tickle, R. Korteling and R.L. Helmer, Phys. Lett. **227B**, 336 (1989)

Ceci79 R.A. Cecil, B.D. Anderson and R. Madey, Nucl. Instr. and Meth. **161**, 439 (1979)

Chen87a Z. Chen, C.K. Gelbke, W.G. Gong, Y.D. Kim, W.G. Lynch, M.R. Maier, J. Pochodzalla, M.B. Tsang, F. Saint-Laurent, D. Ardouin, H. Delagrange, H. Doubre, J. Kasagi, A. Kyanowski, A. Péghaire, J. Péter, E. Rosato, G. Bizard, F. Lefèbvres, B. Tamain, J. Québert and Y.P. Viyogi, Phys. Rev. C. **36**, 2297 (1987)

Chen87b Z. Chen, C.K. Gelbke, J. Pochodzalla, C.B. Chitwood, D.J. Fields, W.G. Gong, W.G. Lynch and M.B. Tsang, Nucl. Phys. **A473** 564 (1987)

Chen87c Z. Chen, C.K. Gelbke, W.G. Gong, Y.D. Kim, W.G. Lynch, M.R. Maier, J. Pochodzalla, M.B. Tsang, F. Saint-Laurent, D. Ardouin, H. Delagrange, H. Doubre, J. Kasagi, A. Kyanowski, A. Péghaire, J. Péter, E. Rosato, G. Bizard, F. Lefèbvres, B. Tamain, J. Québert and Y.P. Viyogi, Phys. Lett. B **199** 171 (1987)

Chit86 C.B. Chitwood, C.K. Gelbke, J. Pochodzalla, Z. Chen, D.J. Fields, W.G. Lynch, R. Morse, M.B. Tsang, D.H. Boal and J.C. Shillcock, Phys. Lett. **172B**, 27 (1986)

Deak87 F. Deak, A. Kiss, Z. Seres, G. Caskey, A. Galonsky and B. Remington, Nucl. Instr. Meth. **A258**, 67 (1987)

Deak89 F. Deak, A. Kiss, Z. Seres, A. Galonsky, C.K. Gelbke, L. Heilbronn, W. Lynch, T. Murakami, H. Schelin, M.B. Tsang, B.A. Remington and J. Kasagi, Phys. Rev. C **39**, 733 (1989)

Deak90 F. Deak, A. Kiss, Z. Seres, A. Galonsky, L. Heilbronn, and H. R. Schelin, Phys. Rev. C **42**, 1029 (1990)

Fox88 D. Fox, D.A. Cebra, J. Karn, C. Parks, A. Pradhan, A. Vander Molen, J. van der Plicht, G.D. Westfall, W.K. Wilson and R.S. Tickle, Phys. Rev. C **38**, 146 (1988)

Frie83 W.A. Friedman, Phys. Rev. C **27**, 569 (1983)

Galo87 A. Galonsky, G. Caskey, L. Heilbronn, B. Remington, H. Schelin, F. Deak, A. Kiss, Z. Seres and J. Kasagi, Phys. Lett. **197B**, 511 (1987)

Gold74 A.S. Goldhaber, Phys. Lett. **53b**, 306 (1974)

Gome88 J. Gomez del Campo, J. L. Charvet, A. D'Onofrio, R. L. Auble, J. R. Beene, M. L. Halbert, and H. J. Kim, Phys. Rev. Lett. **61**, 290 (1988)

Guer83 D. Guerreau, V. Borrel, D. Jacquet, J. Galin, B. Gatty, and X. Tarrago, Phys. Lett. **131B**, 293 (1983)

Hahn87 D. Hahn and H. Stocker, Phys. Rev. C **35**, 1311 (1987)

Haus52 W. Hauser and H. Feshbach, Phys. Rev. **87**, 366 (1952)

Helt88 J. Heltsley, L. Brandon, A. Galonsky, L. Heilbronn, B.A. Remington, S. Langer, A. Vander Molen, J. Yurkon, and J. Kasagi, Nucl. Instr. and Meth. **A263**, 441 (1988)

Kiss87 A. Kiss, F. Deak, Z. Seres, G. Caskey, A. Galonsky, L. Heilbronn, B.A. Remington and J. Kasagi, Phys. Lett. **184B**, 149 (1987)

Kiss89 A. Kiss, F. Deak, Z. Seres, G. Caskey, A. Galonsky, B. Remington and L. Heilbronn, Nucl. Phys. **A499**, 131 (1989)

Kull67 L. A. Kull, Phys. Rev. **163**, 1066 (1967)

Kurz64 R.J. Kurz, University of California Radiation Lab Internal Report URCL-11339 (1964)

Lee90a Jeong Ho Lee, W. Benenson, and D.J. Morrissey, Phys. Rev. C **41**, 1562 (1990)

Lee90b J.H. Lee, W. Benenson, C. Bloch, Y. Chen, R.J. Radtke, E. Kashy, M.F. Mohar, D.J. Morrissey, R. Blue, and R.M. Ronningen, Phys. Rev. C **41**, 2406 (1990)

McLa88 V. McLane, C.L. Dunford and P.F. Rose, "Neutron Cross Sections" vol. 2, Academic Press (1988)

Menc83 A. Menchaca-Rocha, M.E. Brandan, M. Buenerd, J. Chauvin, D. Lebrun, P. Martin, P. de Santignon, J.C. Gondrand, I. Dorion, and A. Lounis, Phys. Lett. **131B**, 31 (1983)

Morr84 D.J. Morrissey, W. Benenson, E. Kashy, B. Sherrill, A.D. Panagiotou, R.A. Blue, R.M. Ronningen, J. van der Plicht and H. Utsunomiya, Phys. Lett. **148B**, 423 (1984)

Morr85 D.J. Morrissey, W. Benenson, E. Kashy, C. Bloch, M. Lowe, R.A. Blue, R.M. Ronningen, B. Sherrill, H. Utsunomiya and I. Kelson, Phys. Rev. C **32**, 877 (1985)

Mona58 J.E. Monahan, L.C. Biedenharn and J.P. Schiffer, Argonne National Laboratory, ANL-5846 (1958)

Moug81 J. Mougey, R. Ost, M. Buenerd, A.J. Cole, C. Guet, D. Lebrun, J.M. Loiseaux, P. Martin, M. Maurel, E. Monnand, H. Nifenecker, P. Perrin, J. Pinston, C. Ristori, P. de Saintignon, F. Schussler, L. Carlen, B. Jakobsson, A. Oskarsson, I. Otterlund, B. Schroder, H.A. Gustafsson, T. Johansson, H. Ryde, J.P. Bondorf, O.B. Nielsen, and G. Tibell, Phys. Lett. **105B**, 25 (1981)

Murp83 M.J. Murphy and R.G. Stodstad, Phys. Rev. C **28**, 428 (1983)

Namb83 M.N. Namboodiri, R.K. Choudhury, J.B. Natowitz, K. Hagel, L. Adler, P.L. Gonthier, H. Simon, S. Kniffen, R. Patton, E. Tomasi, C. Ngo, C. Mazur and M. Ribrag, Phys. Rev. C **28**, 460 (1983)

Naya89 T.K. Nayak, T. Murakami, W.G. Lynch, K. Swartz, D.J. Fields, C.K. Gelbke, Y.D. Kim, J. Pochodzalla, M.B. Tsang, H.M. Xu, F. Zhu and K. Kwiatkowski, Phys. Rev. Lett. **62**, 1021 (1989)

Naya90 T. Nayak, Ph.D. thesis, Mich. State Univ. (1990)

Ohnu86 H. Ohnuma, N. Hoshino, O. Mikoshiba, K. Raywood, A. Sakaguchi, G.G. Shute, B.M. Spicer, M.H. Tanaka, M. Tanifuji, T. Terasawa and M. Yasue, Nucl. Phys. **A448**, 205 (1986)

Ooth77 M. A. Oothoudt and G. T. Garvey, Nucl. Phys. **A284**, 41 (1977)

Poch85a J. Pochodzalla, W.A. Friedman, C. K. Gelbke, W.G. Lynch, M. Maier, D. Ardouin, H. Delagrange, H. Doubre, C. Gregoire, A. Kyanowski, W. Mittig, A. Péghaire, J. Péter, F. Saint-Laurent, Y.P. Viyogi, B. Zwieglinski, G. Bizard, F. Lefébvres, B. Tamain and J. Québert, Phys. Rev. Lett. **55**, 177 (1985)

Poch85b J. Pochodzalla, W.A. Friedman, C. K. Gelbke, W.G. Lynch, M. Maier, D. Ardouin, H. Delagrange, H. Doubre, C. Gregoire, A. Kyanowski, W. Mittig, A. Péghaire, J. Péter, F. Saint-Laurent, Y.P. Viyogi, B. Zwieglinski, G. Bizard, F. Lefébvres, B. Tamain and J. Québert, Phys. Lett. **161B**, 275 (1985)

Poch87 J. Pochodzalla, C. K. Gelbke, W.G. Lynch, M. Maier, D. Ardouin, H. Delagrange, H. Doubre, C. Gregoire, A. Kyanowski, W. Mittig, A. Péghaire, J. Péter, F. Saint-Laurent, B. Zwieglinski, G. Bizard, F. Lefébvres, B. Tamain, J. Québert, Y.P. Viyogi, W.A. Friedman and D.H. Boal, Phys. Rev. C **35**, 1695 (1987)

Sain88 F. Saint-Laurent, A. Kyanowski, D. Ardouin, H. Delagrange, H. Doubre, C. Gregoire, W. Mittig, A. Peghaire, J. Peter, G. Bizard, F. Lefebvres, B. Tamain, J. Quebert, Y. P. Viyogi, J. Pochodzalla, C. K. Gelbke, W. Lynch, and M. Maier, Phys. Lett. **202B**, 190 (1988)

Remi86 B.A. Remington, Ph.D. Thesis, Michigan State University (1986)

Siem71 P.J. Siemens, J.P. Bondorf, D.H.E. Gross and F. Dickman, Phys. Lett. **36B**, 24 (1971)

Siwe85 K. Siwek-Wilczynska, R.A. Blue, L.H. Harwood, R.M. Ronningen, H. Utsunomiya, J. Wilczynski and D.J. Morrissey, Phys. Rev. C **32**, 1450 (1985)

Vand85 A. Vander Molen, R. Au, R. Fox, and T. Glynn, Nucl. Instr. and Meth. **A236**, 359 (1985)

West76 G.D. Westfall, J. Gosset, P.J. Johansen, A.M. Poskanzer and W.G. Meyer, Phys. Rev. Lett **37**, 1202 (1976)

Wilc89 J. Wilczynski and H.W. Wilschut, Phys. Rev. C **39**, 2475 (1989)

Wilc90 J. Wilczynski and K. Siwek-Wilczynska, Phys. Rev. C **41**, R1917 (1990)

Wozn72 G.J. Wozniak, H.L. Harney, K.H. Wilcox and J. Cerny, Phys. Rev. Lett. **28**, 1278 (1972)

Xu86 H.M. Xu, D.J. Fields, W.G. Lynch, M.B. Tsang, C.K. Gelbke, M.R. Maier, D.J. Morrissey, J. Pochodzalla, D.G. Sarantites, L.G. Sobotka, M.L. Halbert, D.C. Hensley, D. Hahn and H. Stocker, Phys. Lett. **182B**, 155 (1986)

Xu89 H.M. Xu, W.G. Lynch, C.K. Gelbke, M.B. Tsang, D.J. Fields, M.R. Maier, D.J. Morrissey, T.K. Nayak, J. Pochadzalla, D.G. Sarantites, L.G. Sobotka, M.L. Halbert and D.C. Hensley, Phys. Rev. C **40**, 186 (1989)

Youn71 P.G. Young and R.H. Stokes, Phys. Rev. C **4**, 1597 (1971)